



UNIVERSIDADE TÉCNICA DE LISBOA  
INSTITUTO SUPERIOR TÉCNICO

# Estimation of Exclusion Zones for Base Station Antennas in Wireless Communication Systems

Carla Sofia Carita Castelo Grilo de Oliveira  
(*Licenciada*)

Dissertação para a obtenção do grau de Mestre  
em Engenharia Electrotécnica e de Computadores

**Orientador:** Doutor Luís Manuel de Jesus Sousa Correia

**Co-Orientador:** Doutor Carlos António Cardoso Fernandes

**Júri**

**Presidente:** Doutor Carlos António Cardoso Fernandes

**Membros:** Doutor José Fernando da Rocha Pereira

Doutor Luís Manuel de Jesus Sousa Correia

Doutor Custódio José de Oliveira Peixeiro

Novembro 2006



*To my parents*



# Acknowledgements

First of all, I would like to thank Prof. Luís Correia and Prof. Carlos Fernandes for having supervised this work and for providing me all the means for its development. To Prof. Luís Correia, I would like to thank for his discipline, for the constant work guidelines and for his true human character. To Prof. Carlos Fernandes, I would like to thank all his availability during my first WIPL-D incursions, and also all his exceptional ideas for routing the path underlying this work.

To Prof. Yngve Hamnerius from Chalmers University of Technology, I would like to thank the valuable information sent to me, which has been the starting point of this work. In what concerns antenna simulation, a special recognition to Lars Goldstein and Thomas Haunberger, from Kathrein, to Ana Claro, Helene Doussineau and Pompeu Costa, from Optimus, and also to Prof. Custódio Peixeiro. Concerning Matlab programming aspects, a really special thanks to my colleague José Nascimento and also to Martjin Kuipers. Regarding antenna measurements, I would like to thank Jerzy Guterman, and also Mr. Carlos Brito and António Miguel Almeida, from IST radiofrequency laboratories.

To my colleagues Gonçalo Carpinteiro and Daniel Sebastião, I would like to thank all their understanding and availability, which were decisive for the conclusion of this work. Thank you for your friendship.

To the other colleagues from IST and GROW, with whom I have worked throughout these last years, I would like to thank for providing a cheerful working environment.

I would like to express my gratitude to my dear friend Sofia, for her absolute support. I would also like to thank the words of motivation from my dear friends Vânia and Carla.

A special thank to Jaime, who helped me to believe I could face this challenge.

A last thank to my wonderful family, in particular to my parents, for their unconditional and constant support throughout one more journey of my life.



# Abstract

This work aims at developing a model for the estimation of exclusion zones around base station antennas in wireless communication systems, taking into account the actual surrounding environment. Wave propagation theory and numerical methods were applied to model a GSM900 base station antenna, using the WIPL-D software. Antenna's performance was analysed in free space conditions and on five possible scenarios of installation, composed of dielectric and metallic parts. A measurement campaign was performed to assess the accuracy of simulations, which are based on simple and limited models of a real situation. A good agreement is found between simulations and measurements. Results clearly show that the exclusion zone calculated in free space conditions must be redefined, due to the presence of surrounding objects. It is concluded that, for typical scenarios, the exclusion radius might be estimated as twice the one obtained under free space conditions. Exception is made for corner configurations with a metallic part on the back of the antenna, where the exclusion radius may increase by a factor of 5. Although all the work has been developed for a GSM900 antenna, the main conclusions are valid for the other wireless technologies (GSM1800, UMTS, WiFi and WIMAX).

## Keywords

Electromagnetic Fields. Wireless systems. Antenna. Exclusion Zone. Numerical Simulation.





# Resumo

Neste trabalho desenvolve-se um método para estimar zonas de exclusão em redor de antenas de estação base de sistemas de comunicação sem fios, considerando o ambiente envolvente. Aplica-se a teoria da propagação electromagnética e métodos numéricos na simulação de uma antena de estação base de GSM900, através do *software* WIPL-D. Analisa-se o seu desempenho em condições de espaço livre e em cinco cenários prováveis de instalação, compostos por elementos metálicos e dieléctricos. Fizeram-se medidas para aferir os resultados das simulações, dado que os cenários simulados são baseados em modelos geométricos simples e com dimensões limitadas de casos reais. As medidas efectuadas confirmam os resultados das simulações. Conclui-se que, claramente, a zona de exclusão estimada em espaço livre deve ser redefinida quando as antenas são colocadas no seu ambiente operacional, devido à presença dos vários objectos envolventes. Os resultados mostram que, tipicamente, o raio da zona de exclusão corresponde ao dobro daquele que é obtido em condições de espaço livre. Exceptuam-se configurações de canto e em que a antena é encostada a um elemento metálico, situação em que o raio de exclusão se estende até um factor de 5. Os resultados aplicam-se também aos sistemas GSM1800, UMTS, WiFi e WIMAX.

## Palavras-chave

Campos Electromagnéticos. Sistemas sem fios. Antena. Zona de Exclusão. Simulação Numérica.



# Table of Contents

<b><i>Acknowledgements</i></b> .....	<b>v</b>
<b><i>Abstract</i></b> .....	<b>vii</b>
<b><i>Resumo</i></b> .....	<b>ix</b>
<b><i>Table of Contents</i></b> .....	<b>xi</b>
<b><i>List of Figures</i></b> .....	<b>xiii</b>
<b><i>List of Tables</i></b> .....	<b>xvii</b>
<b><i>List of Abbreviations</i></b> .....	<b>xix</b>
<b><i>List of Symbols</i></b> .....	<b>xxi</b>
<b>1 Introduction</b> .....	<b>1</b>
<b>2 Theoretical Aspects</b> .....	<b>5</b>
2.1 Antennas and propagation .....	6
2.1.1 Basic aspects of propagation of EMFs .....	6
2.1.2 Fundamental parameters of antennas .....	9
2.2 Wireless Communication Systems .....	11
2.2.1 Radio interface .....	12
2.2.2 Characterisation of installations .....	16
2.3 Exposure to electromagnetic radiation .....	21
2.3.1 Exposure guidelines .....	21
2.3.2 Measurement guidelines .....	23

2.4	Methods for exposure estimation.....	25
2.4.1	Estimation of exclusion zones .....	25
2.4.2	Estimation of EMFs in the near-field region.....	28
2.4.3	Influence of the surrounding environment.....	32
<b>3</b>	<b>Numerical Methods.....</b>	<b>37</b>
3.1	Integral Equation – Method of Moments.....	38
3.2	WIPL-D software application.....	43
3.3	Antenna simulation using WIPL-D .....	48
<b>4</b>	<b>Estimation of Exclusion Zones .....</b>	<b>53</b>
4.1	Description of scenarios .....	54
4.2	Comparison between measurements and simulations .....	59
4.3	Comparison of scenarios .....	64
4.4	Exclusion zones calculation .....	68
<b>5</b>	<b>Conclusions.....</b>	<b>77</b>
<b>Annex A – Antennas used in Wireless Communication Systems .....</b>		<b>83</b>
<b>Annex B – Simulation of the 736 624 Kathrein Antenna .....</b>		<b>97</b>
<b>Annex C – Study on the accuracy of numerical simulations.....</b>		<b>105</b>
C.1	Accuracy of the parameters of the analysis.....	106
C.2	Accuracy of the geometrical model.....	112
C.3	Use of symmetry .....	116
<b>Annex D – Radiation patterns .....</b>		<b>121</b>
<b>References .....</b>		<b>125</b>

# List of Figures

Figure 2.1 - Boundary regions of the different radiation fields existing around an antenna.....	7
Figure 2.2 – Coordinate system for antenna analysis (adapted from [Bala97]).....	9
Figure 2.3 – Linear plot of a radiation pattern (extracted from [Bala97]).....	10
Figure 2.4 – Omnidirectional antenna radiation patterns (extracted from [KATH05a]). .....	11
Figure 2.5 – Sector antenna radiation patterns (extracted from [KATH05a]). .....	11
Figure 2.6 – Wireless communication systems spectrum allocation.....	16
Figure 2.7 – Omnidirectional BS (adapted from [KATH05a]).....	19
Figure 2.8 – Sector BS antenna (adapted from [KATH05a]). .....	19
Figure 2.9 – WiFi patch antenna (extracted from [CISC06b]). .....	20
Figure 2.10 – Initial plans for WiMAX topology of installation (extracted from [Vaug04]). .....	20
Figure 2.11 – Exclusion zone surrounding a BS antenna (extracted from [OrFr04]).....	25
Figure 2.12 – Cylindrical exclusion zone. ....	27
Figure 2.13 – Example of a parallelepiped exclusion zone (adapted from [CENE02]). .....	27
Figure 2.14 – Example of a complex exclusion zone (extracted from [Dane04]). .....	28
Figure 2.15 – Scheme of a typical 4-element GSM antenna. ....	34
Figure 3.1 – Inside configuration of a GSM antenna (extracted from [KATH06a]). .....	38
Figure 3.2 – Inside configuration of a UMTS antenna (extracted from [KTHS06]). .....	38
Figure 3.3 – Inside configuration of a WiFi antenna (extracted from [CISC06a]). .....	39
Figure 3.4 – Thin-wire model of cylindrical antenna. ....	40
Figure 3.5 – Geometrical definition of a wire (right-truncated cone) in WIPL-D (extracted from [WIPL05]). .....	44
Figure 3.6 – Geometrical definition of a plate (bilinear surface) in WIPL-D (extracted from [WIPL05]). .....	44
Figure 3.7 – The 736 624 Kathrein antenna (extracted from [KATH05b]). .....	49
Figure 3.8 – 736 624 Kathrein antenna radiation patterns (extracted from [KATH05b]). .....	49
Figure 3.9 - Internal parts of the 736 624 Kathrein antenna (side and front views) [KATH05c]. .....	49
Figure 3.10 – Model for simulation of the 736 624 Kathrein antenna.....	50
Figure 3.11 – 3D radiation pattern of the simulated antenna.....	50

Figure 3.12 – Return Loss curve for the simulated model of the antenna. ....	51
Figure 4.1 – “Dielectric Corner” (DiCo) scenario.....	54
Figure 4.2 – “Metallic Corner” (MeCo) scenario.....	54
Figure 4.3 – “Metallic Pole” (MePo) scenario.....	55
Figure 4.4 – “Metallic Roof” (MeRo) scenario. ....	55
Figure 4.5 – “Metallic Roof with Dielectric Corner” (MeRC) scenario. ....	55
Figure 4.6 – Sketch of the measurement set-up (isolated antenna). ....	59
Figure 4.7 – Measurements of the isolated antenna at the anechoic chamber.....	60
Figure 4.8 – Horizontal radiation pattern. ....	61
Figure 4.9 – Vertical radiation pattern. ....	61
Figure 4.10 – Sketch of the measurement set-up (MeRo scenario). ....	62
Figure 4.11 – Sketch of the measurement set-up (MeRC scenario). ....	62
Figure 4.12 – Comparison of results for the MeRo scenario.....	63
Figure 4.13 – Comparison of results for the MeRC scenario. ....	63
Figure 4.14 – RL curves for the various scenarios. ....	66
Figure 4.15 – 3D radiation pattern obtained for the DiCo scenario. ....	67
Figure 4.16 – 3D radiation pattern obtained for the MeCo scenario. ....	67
Figure 4.17 – 3D radiation pattern obtained for the MePo scenario. ....	67
Figure 4.18 – Example of near field calculation using WIPL-D (MePo scenario).....	68
Figure 4.19 – Definition of horizontal and vertical planes. ....	69
Figure 4.20 – Estimation of compliance boundary in the near-field ( $P_{in} = 200$ mW).....	69
Figure 4.21 – Estimation of exclusion zone for the isolated antenna ( $P_{in} = 50$ W).....	70
Figure 4.22 – Estimation of exclusion zone for the DiCo scenario ( $P_{in} = 50$ W).....	70
Figure 4.23 – Estimation of exclusion zone for the MeCo scenario ( $P_{in} = 50$ W). ....	70
Figure 4.24 – Estimation of exclusion zone for the MePo scenario ( $P_{in} = 50$ W).....	71
Figure 4.25 – Estimation of exclusion zone for the MeRo scenario ( $P_{in} = 50$ W). ....	71
Figure 4.26 – Estimation of exclusion zone for the MeRC scenario ( $P_{in} = 50$ W).....	71
Figure 4.27 – Exclusion radius for original and extended models of the MeRo scenario (horizontal plane).....	72
Figure 4.28 – Exclusion radius for original and extended models of the MeRo scenario (vertical plane).....	72
Figure 4.29 – Representation of $r_{sno}/r_{ant}$ (vertical plane) for the various scenarios. ....	73
Figure 4.30 – Representation of $r_{sno}/r_{ant}$ (horizontal plane) for the various scenarios.....	73
Figure A.1 – Sector GSM900 antenna (extracted from [KATH05a]). ....	85
Figure A. 2 - Sector GSM1800 antenna (extracted from [KATH05a]).....	86

Figure A.3 - Sector UMTS antenna (extracted from [KATH05a]).....	87
Figure A.4 - Sector antenna used for WiFi systems (extracted from [CISC06b]).....	88
Figure A.5 – Omnidirectional GSM900 antenna (extracted from [KATH05a]). .....	89
Figure A.6 – Omnidirectional GSM1800/UMTS antenna (extracted from [KATH05a]). .....	90
Figure A.7 - Omnidirectional antenna used for WiFi systems (extracted from [CISC06b]).....	91
Figure A.8 – Omnidirectional GSM indoor antenna(extracted from [KATH05a]). .....	93
Figure A.9 – WiFi indoor omnidirectional antenna (extracted from [CISC06b]).....	94
Figure A.10 – Indoor bi-directional multi band antenna(extracted from [KATH05a]). .....	95
Figure A.11 – Indoor omnidirectional multi band antenna(extracted from [KATH05a]). .....	96
Figure B.1 – The 736 624 Kathrein antenna (extracted from [KATH05b]). .....	99
Figure B.2 – Internal components of the 736 624 Kathrein antenna (side and front views) [KATH05c]. .....	99
Figure B.3 – Radiation patterns.....	100
Figure B.4 – Simulation of the 736 624 Kathrein antenna (Model 1). .....	100
Figure B.5 – Simulation of the 736 624 Kathrein antenna (Model 2). .....	101
Figure B.6 – Simulation of the 736 624 Kathrein antenna (Model 3). .....	101
Figure B.7 - 3D radiation pattern (Model 1). .....	102
Figure B.8 – Radiation patterns (Model 1). .....	102
Figure B.9 – 3D radiation pattern (Model 2). .....	102
Figure B.10 – Radiation patterns (Model 2). .....	103
Figure B.11 – 3D radiation pattern (Model 3). .....	103
Figure B.12 – Horizontal and vertical patterns (Model 3). .....	103
Figure B.13 – Return loss curve for Model 3.....	104
Figure C.1 – Radiation patterns for the DiCo scenario.....	108
Figure C.2 – Radiation patterns for the MeCo scenario.....	108
Figure C.3 – Radiation patterns for the MePo scenario. ....	109
Figure C.4 – Radiation patterns for the MeRo scenario.....	109
Figure C.5 – Radiation patterns for the MeRC scenario. ....	109
Figure C.6 – Geometrical models for the MePo scenario.....	112
Figure C.7 – Radiation patterns for the different geometrical models (MePo scenario).....	113
Figure C.8 – Geometrical models for the DiCo scenario. ....	114
Figure C.9 – Radiation patterns for the different geometrical models (DiCo scenario).....	115
Figure C.10 – Radiation patterns obtained for the MePo scenario. ....	117
Figure C.11 – Horizontal radiation pattern obtained for the MeRo scenario.....	118
Figure C.12 – Vertical radiation pattern obtained for the MeRo scenario. ....	119

Figure D.1 – 3D radiation pattern obtained for the DiCo scenario. ....	122
Figure D.2 – 3D radiation pattern obtained for the MeCo scenario. ....	122
Figure D.3 – 3D radiation pattern obtained for the MePo scenario. ....	123
Figure D.4 – 3D radiation pattern obtained for the MeRo scenario. ....	123
Figure D.5 – 3D radiation pattern obtained for the MeRC scenario. ....	124



# List of Tables

Table 2.1 – Typical antenna gain values.....	10
Table 2.2 - GSM BS maximum output power levels [ETSI92].....	12
Table 2.3 - UMTS BSs EIRP [Bena99].....	13
Table 2.4 – European specifications of WiFi standards [Bing02].....	14
Table 2.5 – Classification of cells in wireless communications. ....	17
Table 2.6 – Classification of BS installations (extracted from [OFRC04]).....	18
Table 2.7 – ICNIRP reference levels for general public exposure (unperturbed rms values). ....	22
Table 2.8 – Reference and alternative methodologies established by the EN 50383 standard, [CENE02].....	24
Table 3.1 – Technical characteristics of the 736 624 Kathrein antenna (extracted from [KATH05b]).....	48
Table 3.2 – Comparison between the simulated antenna and the real one. ....	51
Table 4.1 – Material Properties (extracted from [DaCo99]). ....	56
Table 4.2 - Simulations performed with different accuracies of parameters.....	57
Table 4.3 – Input impedance for the various scenarios ( $f = 902.5$ MHz).....	65
Table A.1 – Technical characteristics for a WiMAX antenna (based on [WiMA06]).....	84
Table A.2 – Summary of typical BS outdoor antennas.....	84
Table A.3 – Technical characteristics of a typical sector GSM900 antenna (extracted from [KATH05a]).....	85
Table A.4 – Technical characteristics of a sector GSM1800 antenna (extracted from [KATH05a]).....	86
Table A.5 – Technical characteristics of a sector UMTS antenna (extracted from [KATH05a]).....	87
Table A.6 – Technical characteristics of a sector WiFi antenna (extracted from [CISC06b]).....	88
Table A.7 – Technical characteristics of an omnidirectional GSM900 antenna (extracted from [KATH05a]).....	89
Table A.8 – Technical characteristics of an omnidirectional GSM1800/UMTS antenna (extracted from [KATH05a]).....	90
Table A.9 – Technical characteristics of an omnidirectional WiFi antenna (extracted from [CISC06b]).....	91
Table A.10 – Summary of typical indoor antennas. ....	92

Table A.11 – Technical characteristics of an omnidirectional GSM indoor antenna (extracted from [KATH05a]).....	93
Table A.12 – Characteristics of a WiFi indoor omnidirectional antenna.....	94
Table A.13 – Technical characteristics of an indoor bi-directional multi band antenna (extracted from [KATH05a]).....	95
Table A.14 – Technical characteristics of an indoor omnidirectional multi band antenna (extracted from [KATH05a]).....	96
Table B.1 – Technical characteristics of the 736 624 Kathrein antenna (extracted from [KATH05b]).....	98
Table B.2 – Description of the geometrical models. ....	100
Table B.3 – Input impedance for the three models ( $f = 902.5$ MHz). ....	101
Table B.4 – Radiation characteristics for the three models. ....	104
Table C.1 – Simulations performed with different accuracies of parameters. ....	108
Table C.2 – Simulation results for the DiCo scenario. ....	110
Table C.3 – Simulation results for the MeCo scenario. ....	110
Table C.4 – Simulation results for the MePo scenario. ....	110
Table C.5 – Simulation results for the MeRo scenario. ....	111
Table C.6 – Simulation results for the MeRC scenario. ....	111
Table C.7 – Geometrical models for the MePo scenario. ....	113
Table C.8 – Simulation results for the MePo scenario. ....	114
Table C.9 – Comparison of CPU resources (MePo scenario). ....	114
Table C.10 – Geometrical models for the DiCo scenario.....	115
Table C.11 – Simulation results for the DiCo scenario.....	116
Table C.12 – Comparison of CPU resources (DiCO scenario). ....	116
Table C.13 – Differences in radiation pattern using symmetry (MePo scenario).....	119
Table C.14 – Comparison of CPU resources (MePo scenario).....	120
Table C.15 – Differences in radiation pattern using symmetry (MeRo scenario).....	120
Table C.16 – Comparison of CPU resources (MeRo scenario).....	120

# List of Abbreviations

2G	Second Generation
3D	Three Dimensional
3G	Third Generation
AP	Access Point
BS	Base Station
BSS	Base Station Subsystem
CDMA	Code Division Multiple Access
CENELEC	European Committee for Electrotechnical Standardisation
CEPT	European Conference of Postal and Telecommunications Administrations
CSMA/CA	Carrier Sense Multiple Access Collision Avoidance
DiCo	“Dielectric Corner” scenario
DL	Downlink
DSSS	Direct Sequence Spread Spectrum
ECC	Electronic Communications Committee
EFIE	Electrical Field Integral Equation
EIRP	Effective Isotropic Radiated Power
EM	Electromagnetic
EMF	Electromagnetic Field
ETSI	European Telecommunications Standards Institute
FDD	Frequency Division Duplex
FDMA	Frequency Division Multiple Access
FDTD	Finite Difference Time Domain
FEM	Finite Element Method
FNBW	First-Null-Beam-Width
GO	Geometrical Optics
GSM	Global System for Mobile Communications
GTD	Geometrical Theory of Diffraction
HPBW	Half-Power-Beam-Width

ICNIRP	International Commission on Non-Ionising Radiation Protection
LoS	Line of Sight
MeCo	“Metallic Corner” scenario
MePo	“Metallic Pole” scenario
MeRC	“Metallic Roof with Dielectric Corner” scenario
MeRo	“Metallic Roof” scenario
MoM	Method of Moments
N/A	Non Applicable
NLoS	Non Line of Sight
OFDM	Orthogonal Frequency Division Multiplexing
PMCHW	Poggio, Miller, Chang, Harrington, and Wu
RF	Radio Frequency
RL	Return Loss
rms	Root-Mean-Square
RX	Reception
SAR	Specific Absorption Rate
SFIE	Surface Field Integral Equation
SIE	Surface Integral Equation
TDD	Time Division Duplex
TDMA	Time Division Multiple Access
TRX	Transmitted Radio Carrier
Tx	Transmission
UL	Uplink
UMTS	Universal Mobile Telecommunications System
UTD	Uniform Theory of Diffraction
VSWR	Voltage Stand Wave Ratio
WiFi	Wireless-Fidelity
WiMAX	Worldwide Interoperability for Microwave Access
WLAN	Wireless Local Area Network

# List of Symbols

$\alpha_{3dB}$	Angle defining the HPBW of an antenna
$\varepsilon_s$	Difference between radiation pattern of mode 3 and mode $s$
$\varepsilon_n$	$\varepsilon_s$ for each radiation angle
$\overline{\varepsilon}$	Averaged $\varepsilon_s$
$\sqrt{\overline{\varepsilon^2}}$	RMS $\varepsilon_s$
$\overline{\varepsilon_w}$	Weighted average $\varepsilon_s$
$\varepsilon$	Complex relative permittivity of the medium
$\varepsilon_i$	Imaginary part of complex relative permittivity
$\varepsilon_r$	Real part of complex relative permittivity
$\lambda$	Wavelength
$\mu$	Complex relative permeability
$\mu_0$	Free space permeability
$\mu_i$	Imaginary part of complex relative permeability
$\mu_r$	Real part of complex relative permeability
$\sigma$	Conductivity
$\omega$	Angular frequency
$\theta$	Elevation angle
$\theta_{dt}$	Downtilt angle
$\Phi$	Azimuth angle
$\varphi_i$	Phase difference between the element feeding coefficients
$a$	Radius of a wire antenna
$a_1$	Radius of cone end beginning
$a_2$	Radius of cone end ending
$a_n$	Unknown current coefficient
$A_o$	Magnitude
$B$	Magnetic flux density
$d$	Distance from the antenna to observation point

$D$	Largest geometrical dimension of the antenna
$D_{back}$	Back border of an exclusion zone
$D_{bottom}$	Border for the bottom of an exclusion zone
$D'_{bottom}$	Border for the bottom of an exclusion zone (downtilt corrected value)
$D_{down}$	Border for the bottom of an exclusion zone
$D_{front}$	Front border of an exclusion zone
$d_i$	Distance from the centre of the antenna to the centre of the $i$ -th element of the array
$D_i$	Largest dimension of the $i$ -th element of the array
$D_{max}$	Maximum distance of an exclusion zone
$D_{side}$	Border for the sides of an exclusion zone
$D_{top}$	Border for the top of an exclusion zone
$D'_{top}$	Border for the top of an exclusion zone (downtilt corrected value)
$D_{up}$	Border for the top of an exclusion zone
$E$	Electric field strength
$E^{(1)}$	Resulting electric field in domain 1
$E^{(2)}$	Resulting electric field in domain 2
$E_{diffracted-ray}$	Electric field strength caused by the refracted ray
$E_{direct-ray}$	Electric field strength caused by the direct ray
$E_i$	Electric field strength at frequency $i$
$E_{in}$	Incident electric field
$E_i^{(1)}$	Impressed electric field in domain 1
$E_i^{(2)}$	Impressed electric field in domain 2
$E_{ij}$	Electric field strength including the effect of free space propagation, reflections, transmissions and diffractions, weighted by the antenna radiation pattern
$E_{ref i}$	Electric field reference level
$E_{reflected-ray}$	Electric field strength caused by the reflected ray
$E_{tot}$	Total electric field strength at the investigation point
$E_{transmitted-ray}$	Electric field strength caused by the transmitted ray
$f$	Frequency
$F$	Linear operator
$F_i$	Radiation pattern of the $i$ -th element of an array
$G$	Antenna gain
$g$	Response function

$g(\mathbf{R})$	Free-space Green's function
$G(\theta, \Phi)$	Generalised antenna gain
$G(\theta, \Phi)^s$	Antenna gain for simulation mode $s$
$G_H$	Radiation pattern in the horizontal plane
$G_{He}$	Radiation pattern in the horizontal plane for the $e$ -th array element
$G_M$	Maximum gain of an antenna
$G_{n_{ref}}$	Gain of a reference antenna for a particular radiation direction
$g_n$	Basis function
$G_V$	Radiation pattern in the vertical plane
$G_{Ve}$	Radiation pattern in the vertical plane for the $e$ -th array element
$H$	Magnetic field strength
$h$	Excitation function
$H^{(1)}$	Resulting magnetic field in domain 1
$H^{(2)}$	Resulting magnetic field in domain 2
$H_i^{(1)}$	Impressed magnetic field in domain 1
$H_i^{(2)}$	Impressed magnetic field in domain 2
$H_j$	Magnetic field strength at frequency $j$
$H_{refj}$	Magnetic field reference level
$I(s)$	Total current flowing along the cone
$I(\tilde{z})$	Current distribution along a wire antenna
$I_n$	Antenna's current
$i_p(\hat{p})$	Radial unit vector in the local coordinate system perpendicular to the cone axis
$J(s)$	Surface current density
$k$	Propagation constant
$k_0$	Free space propagation constant
$l$	Antenna length
$M$	Number of divisions of a wire
$n$	Radiation angle
$N$	Number of elements of a linear array antenna
$N_A$	Number of radiation angles
$N_R$	Number of propagation rays associated to each antenna element
$p$	Local coordinate about the cone axis measured from the $x$ -axis
$p_1$	Starting coordinate of the quadrilateral sides in the local coordinate system adopted

$p_2$	Starting coordinate of the quadrilateral sides in the local coordinate system adopted
$P_{in}$	Total power delivered to the antenna terminals
$R$	Distance between point of investigation and source point
$r'$	Position vector of the point of investigation
$r(p,s)$	Position vector of the source point
$r_1$	Position vector
$r_{11}$	Position vector of vertices
$r_{12}$	Position vector of vertices
$r_2$	Position vector
$r_{21}$	Position vector of vertices
$r_{22}$	Position vector of vertices
$R_e$	Medium distance between source point and points of investigation belonging to the cone circumference that corresponds to the $s$ -coordinate
$r_i$	Distance from the centre of the antenna to the centre of the $i$ -th element
$r_{ant}$	Exclusion zone radius for the isolated antenna
$r_{sno}$	Exclusion zone radius
$S$	Power density
$s$	Local coordinate along reference-cone generatrix
$s_1$	Starting coordinate of the quadrilateral sides in the local coordinate system adopted
$s_2$	Starting coordinate of the quadrilateral sides in the local coordinate system adopted
$S_{eq}$	Equivalent plane wave power density
$V_i$	Voltage at the feed terminals of a wire antenna
$V_m$	Potential at antenna's terminals
$w$	Weighting / testing functions
$Z_0$	Free space characteristic impedance
$Z_{mn}$	Antenna's input impedance



# **Chapter 1**

## **Introduction**

This chapter gives a brief overview of the work. Before establishing work goals, the scope and motivations are brought up. The current state-of-the-art in the scope of the work is also presented. At the end of the chapter, the innovative aspect of the work is stressed and its structure is provided.

The replacement of the analogue mobile network by the digital one, with the introduction of second generation (2G) mobile systems, in the early 90's, started the wireless communication's revolution, which is continuing today with the deployment of the third generation (3G). Moreover, driven by the success of the Internet in the last years, with increasing data rates made available to the (wired) subscribers and the inherent deployment of new services, certain expectations emerged. Not only businessmen, but also the public in general demand for a wired-service like connection while on the move. This challenge is being coped by emerging technologies, with high speed data rates.

The increasing number of customers of wireless communication technologies has been leading to an increasing deployment of base station (BS) antennas. This is particularly true in urban areas, where those antennas are being deployed on rooftops, façades and more recently in indoor environments. At the same time, a general public concern about possible health hazards caused by radiation from these systems has emerged in the last years.

Mobile operators are being forced to adopt a precautionary approach when dimensioning new BSs, which involves, for instance, the physical delimitation of exclusion zones around antennas, *i.e.*, areas inside which electromagnetic field (EMF) levels are above the reference levels. Usually, exclusion zones are estimated considering free space conditions; however, the environment of installation, in particular the presence of walls, reflecting objects, barriers and others, do affect the overall performance of BS antennas, and consequently the exclusion area.

There are various approaches to solve the problem of estimating EMFs around BSs. The simplest one is the far-field model, defining in most of the cases unfeasible exclusion zones, with distances as large as the far-field distance (around 20-40 m for typical BS antennas). Refined models are required to evaluate EMFs at closer distances, although posing the problem of estimating EMFs in the near-field region. As the field behaviour in this region is complex, numerical methods, such as the Method of Moments (MoM), the Finite Element Method (FEM) or the Finite Difference Time Domain (FDTD) method, may be applied. Their main problem when modelling the external environment is that the dimensions of the region to be studied can be huge compared with the wavelength, thus, requiring unacceptable processing times and available memory. An additional problem is the lack of data on antennas' inside configuration.

The far-field approximation models are a usual approach, [CENE02], [MNMV02]. In general, these models are more accurate predictors of exposure very close to an antenna, where the

far-field model may significantly overestimate EMF values. As many BS antennas are built as an array of dipoles with a reflector behind them, there are also interesting models to estimate exposure taking into account the mutual interference between these dipoles, like the refined far-field model proposed in [OlMa00] and the far-field-gain-based model, [BiGi99]. A different approach is to use the spherical/cylindrical near-field transformations, a standard antenna measurement technique in the near-field, allowing for examination at very short distances to the antenna [BIRC02] and also closely behind the antenna [Frid03]. In [Frid03], it is stated that a combination of spherical and cylindrical near-field transformations techniques is well suited for exposure assessment of panel antennas.

Furthermore, it is necessary to take into account the reflected, transmitted and refracted fields caused by the presence of the various surrounding scattered or reflector objects. A combination of different exposure assessment methods may be used to analyse these situations. In the literature, one can find studies that evaluate human exposure in the case where the BS antenna is near obstacles, [BCPP00], [NMMV01], [BCCP03]. These studies propose hybrid techniques, which start to evaluate the EMFs incident on the exposed subject by using ray tracing techniques, then employ the FDTD method to analyse fields inside the body. Other studies, like [BCFF99] and [Wojc02] consider the use of ray tracing techniques, based on the Geometrical Optics (GO) hypothesis. Under the GO approach, the propagation is considered to take place by “rays” originated in the antenna site, experiencing straight line propagation in free space. Each ray is associated to a local plane wave, which can experience reflection, transmission and diffraction due to the presence of obstacles. Obstacles are modelled as a set of basic homogeneous scattered elements, described by their electromagnetic (EM) properties: dielectric constant, magnetic permeability, and conductivity. The GO approach allows determining the EMFs of reflected and transmitted rays, through the well-known Fresnel coefficients. The Geometrical Theory of Diffraction (GTD) and the Uniform Theory of Diffraction (UTD) extend the GO applicability domains to rays diffracted by edges and corners. Ray tracing techniques determine the different paths taken by the rays, with a precision dependent on a limiting number of successive scattering actions a ray can experience.

A practical approach to the problem of estimate exclusion zones taking the environment of installation into account was found in [Dane04], where the author studies possible changes of the compliance boundary of a BS antenna due to the presence of other radio sources and of a metallic plate in its vicinity. The study is based on broadband and frequency selective

measurements and also on simulations performed with commercial numerical software. No studies were found on the literature considering real BS installation scenarios.

The current thesis presents a possible approach to the evaluation of compliance boundaries for BS antennas, taking common indoor and outdoor installation scenarios into account. Moreover, it considers the influence of both metallic and dielectric three dimensional (3D) structures surrounding BS antennas. Although being focused on the evaluation of exclusion zones, the work also analyses expectable changes on antenna's impedance mismatch and on the radiation pattern. For that, WIPL-D [WIPL05], a commercial numerical EM code, is employed to estimate EMFs close to a particular GSM900 BS antenna installed on different scenarios. Major conclusions are valid for other wireless technologies. The work provides qualitative results of great value to radio engineers, when dimensioning and installing new antennas. As it is shown, wireless networks planning tools can not continue uncritically applying free space conditions to estimate exclusion zones.

Preliminary results of this work were already presented in "EHE'06 - International Conference on EMFs, Health and Environment", [OIFC06]. A positive feedback and new ideas from international EMF experts were gathered, allowing to improve the remainder of work.

This document is composed of 4 chapters, besides the current one, and of 4 annexes. The following chapter presents theoretical aspects related to antennas and propagation, wireless communication systems, exposure thresholds and guidelines for assessment of radiation levels and different approaches for the estimation of EMFs levels. Chapter 3 refers to the numerical method employed in this thesis and on the way this method is applied in WIPL-D. Practical results achieved on the simulation of a GSM900 BS antenna are presented at the end of the chapter. In Chapter 4, the five simulated scenarios of installation of BS antennas are described and verified through measurements, then compared between them, resulting on a useful outcome for the estimation of exclusion zones. Chapter 5 finalises this thesis, drawing conclusions and further suggestions of work. Annex A includes a technical overview on the antennas used in wireless communication systems, while Annex B presents details on the simulation of the GSM900 BS antenna studied in this work. Annex C contains a detailed study on the accuracy of numerical simulations performed with WIPL-D and Annex D presents the complete set of radiation patterns obtained from simulations.

# Chapter 2

## Theoretical Aspects

This chapter presents theoretical aspects on the estimation of exclusion zones around BS antennas from wireless communication systems, considering the surrounding environment. Section 2.1 refers to basic aspects of EMFs propagation, and describes some of the antennas characterisation parameters. Section 2.2 gives an insight into the radio interface of the cellular communication systems predominantly used, as well as on wireless emerging technologies. Section 2.3 gives a brief overview on exposure thresholds and on the main guidelines established by international entities for the assessment of radiation levels. Finally, Section 2.4 presents a literature survey on different approaches to the assessment of EMFs.

## **2.1 Antennas and propagation**

The evaluation of EMFs in the vicinity of a BS antenna and the study of the impact of the environment surrounding the antenna require the knowledge of basic propagation aspects, as well as information on antennas performance. This section gives a brief overview of some basic aspects of EMFs propagation, and describes some of the antennas characterisation parameters. The analysis presented here focuses on mobile and wireless communication systems.

### **2.1.1 Basic aspects of propagation of EMFs**

When assessing EMFs in the area around an antenna, one must take into account that these fields vary considerably, depending on the investigated zone. According to EMFs structure, the space surrounding an antenna is commonly divided into three regions [Bala97], Figure 2.1:

- Reactive near-field region.
- Radiating near-field (Fresnel) region.
- Far-field (Fraunhofer) region.

The theory describing EMFs is given by solving Maxwell's equations. In the far-field region of an antenna, the field calculation does not take the antenna size into account, which is assumed to be a point source. This region corresponds to:

$$d > \frac{2D^2}{\lambda}. \quad (2.1)$$

where:

- $D$  – Largest geometrical dimension of the antenna [m].
- $d$  – Distance from the antenna to the observation point [m].
- $\lambda$  – Wavelength [m].

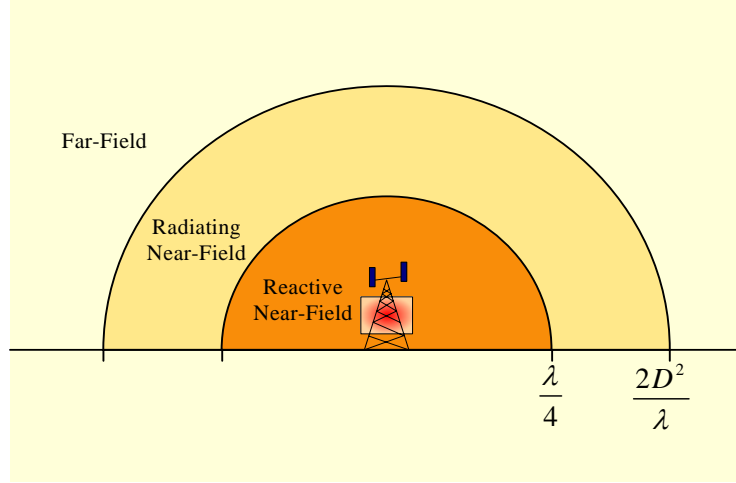


Figure 2.1 - Boundary regions of the different radiation fields existing around an antenna.

In the far-field region, the amplitude of the electric field,  $E$ , may be expressed by:

$$E(d) = A_0 \frac{e^{-jkd}}{d}. \quad (2.2)$$

where:

- $E$  – Electric field strength [V/m].
- $A_0$  – Magnitude [V].
- $k = \frac{2\pi}{\lambda} \sqrt{\epsilon}$  – Propagation constant [ $\text{m}^{-1}$ ].
- $\epsilon$  – Relative permittivity of the medium.

One also has:

$$\frac{E}{H} = Z_0 = 120\pi \, \Omega. \quad (2.3)$$

where:

- $H$  – Magnetic field strength [A/m].
- $Z_0$  – Free space characteristic impedance [ $\Omega$ ].

and:

$$S = EH. \quad (2.4)$$

where:

- $S$  – Power density [W/m<sup>2</sup>].

[CENE02] recommends  $\lambda/4$  as the boundary between the radiating near-field and the reactive near-field regions for RF exposure compliance. The criterion for defining the outer boundary is based on a maximum phase error of  $\pi/8$ .

In the radiating near-field region, the angular field distribution depends on the distance to the antenna. If the antenna has a maximum dimension that is not large compared to the wavelength, this region may not exist. The radiating near-field region is defined by:

$$\frac{\lambda}{4} < d \leq \frac{2D^2}{\lambda}. \quad (2.5)$$

The reactive near-field region is the portion of the near-field region where reactive oscillating and non-radiating energy predominates. It corresponds to the closest region around the transmitting antenna, delimited by:

$$d \leq \frac{\lambda}{4}. \quad (2.6)$$

The environment surrounding a BS antenna influences the behaviour of EMFs, as the transmission path between the transmitter and the receiver can vary from simple line-of-sight (LoS) to one that is obstructed by any objects. Due to multiple reflections and diffractions from various objects, EM waves travel along different paths of varying lengths, these lengths decreasing as the distance between the transmitter and the receiver increases. The interaction of these waves at a specific location is known as the *multipath* phenomenon [Pars92]. Incoming waves arrive from different directions with different time delays, being vectorial combined at the receiver antenna to produce a signal that can be large or small depending on the distribution of phases among multipath waves. The received signal may vary several tens of dB, depending on the location of the receiver, even for small distances between different locations at the order of the wavelength. Short-term variations in the signal amplitude caused by the local multipath are known as *fast fading*.

In case of non-line-of-sight (NLoS) configurations, the Rayleigh distribution is commonly used to model fast fading. In the situation of a LoS path, or at least, when there is a dominant component, the Rician distribution is used to model fast fading. In this case, spatial variations are



less important.

### 2.1.2 Fundamental parameters of antennas

The level of exposure to EM radiation transmitted by a BS depends on some characteristics of the antennas. The behaviour of an antenna is described by various parameters, whose definition is given in this section.

It is usual to define a convenient set of space coordinates for antenna analysis, Figure 2.2. This coordinate system will be the reference used throughout this thesis. The coordinate system axis represented in Figure 2.2 is centred on the antenna. Figure 2.3 represents a plot of a *radiation pattern*, which is one of antenna's main characteristics, showing lobes and beam-widths; in this figure, the concept of *half-power-beam-width* (HPBW) is represented. In most cases, the radiation pattern is determined in the far-field, being represented as a function of the directional coordinates. Usually, it is represented by the plots of the  $E$  field on the horizontal plane ( $\theta=90^\circ$ ) and on a vertical plane that contain the direction of maximum field ( $\Phi=\text{constant}$ ).

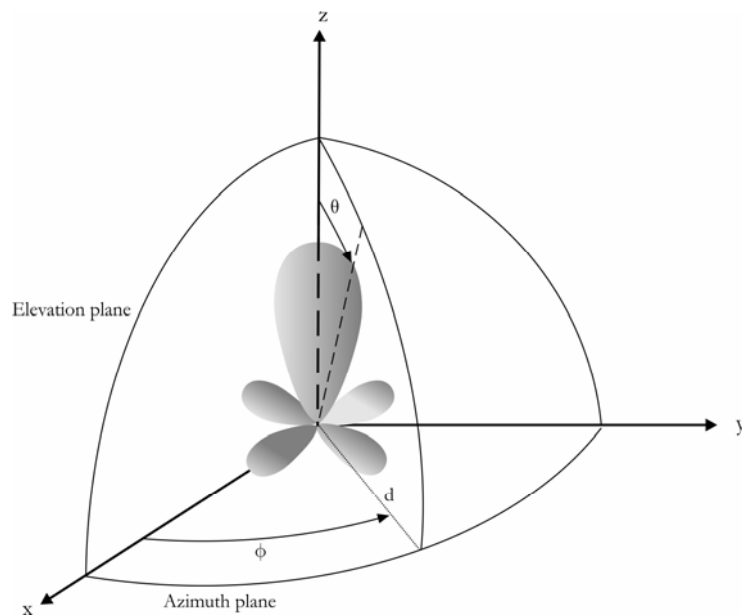


Figure 2.2 – Coordinate system for antenna analysis (adapted from [Bala97]).

A useful measure of an antenna's performance is the *directivity*, giving an indication of the directional properties of the antenna compared to those of an isotropic source.

Another important characteristic of an antenna is its *gain*, which takes the efficiency of the antenna into account as well as its directional capabilities, being a measure of how effective an antenna is on radiating power in the direction of its main beam. According to a survey undertaken on major manufacturers, [CISC06a], [KATH06] and mobile operators, [MONI04], the typical gain values used in mobile and wireless communication systems are presented in Table 2.1.

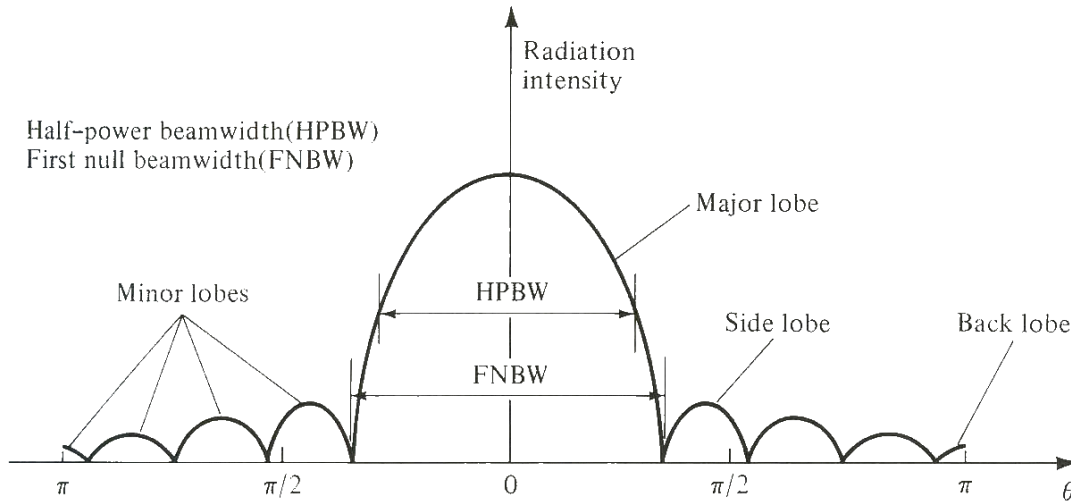


Figure 2.3 – Linear plot of a radiation pattern (extracted from [Bala97]).

Table 2.1 – Typical antenna gain values.

$G$ [dBi]		System			
		GSM	UMTS	WiFi	WiMAX
Environment	Outdoor	[7, 22]	18	[12, 24]	[8, 27]
	Indoor	[2, 7]	[2, 7]	[3, 8]	N/A <sup>1</sup>

<sup>1</sup> Non Applicable.

Examples of omnidirectional and sector antenna radiation patterns are represented in Figure 2.4 and Figure 2.5. The power transmitted by sector antennas may be many times stronger in the intended directions compared to an omni one, while it will be weaker in other directions. For example, the exposure behind a sector antenna can be 300 times weaker than in the main lobe [BFHM00].

The *polarisation* of an antenna is another important characteristic; it describes the spatial orientation of the  $E$ -field when a wave is transmitted or received by an antenna, and may be classified as linear, circular or elliptical. The antennas used in cellular communications are generally vertically or double ( $\pm 45^\circ$ ) polarised. Most of the antennas employed in WiFi systems are also vertically polarised, in order to minimise reflections. For WiMAX, double polarisation will be a probable solution.

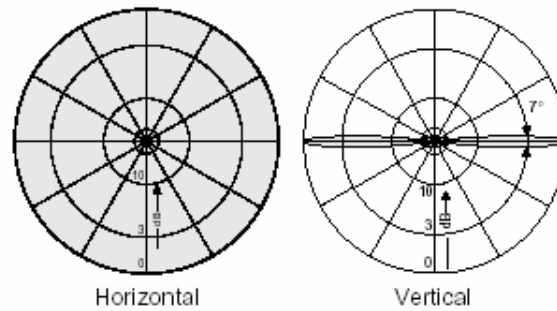


Figure 2.4 – Omnidirectional antenna radiation patterns (extracted from [KATH05a]).

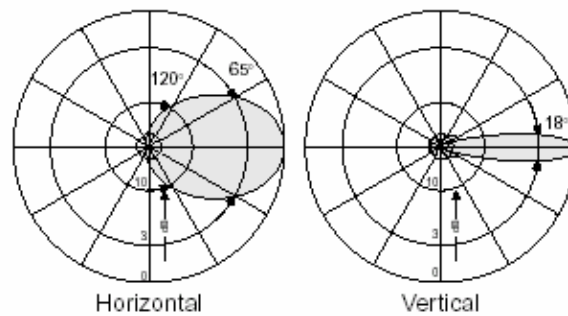


Figure 2.5 – Sector antenna radiation patterns (extracted from [KATH05a]).

## 2.2 Wireless Communication Systems

This section gives an insight into the main characteristics of the radio interface of the cellular communication systems predominantly used, *Global System for Mobile Communications* (GSM) [MoPa92] and *Universal Mobile Telecommunications System* (UMTS) [HoTo00], as well as on the wireless emerging technologies *Wireless-Fidelity* (WiFi) [Bing02] and *Worldwide Interoperability for Microwave Access* (WiMAX) [WiMA05].

### 2.2.1 Radio interface

In the GSM standards, [ETSI92], both the Time Division Multiple Access (TDMA) and the Frequency Division Multiple Access (FDMA) technologies have been adopted. Transmission over this system makes use of different frequency bands, divided into 200 kHz bandwidth channels and with each carrier frequency split into 8 time-slots. The frequency bands defined for the operation of GSM are:

- [890, 915] MHz (uplink (UL)) and [935, 960] MHz (downlink (DL)) for GSM900;
- [1710, 1785] MHz (UL) and [1805, 1880] MHz (DL) for GSM1800.

In Portugal, each one of the three mobile operators owns 40 carriers (except one of them, which has only 39 carriers) in the 900 MHz band and other 40 in the 1800 MHz one. In areas with high population density and three operators present, this results typically in a maximum of 20 carriers per cell.

The standard GSM BS transmitter maximum output levels, measured at the input of the Base Station Subsystem (BSS) Transmission (Tx) combiner, are presented in Table 2.2.

Table 2.2 - GSM BS maximum output power levels [ETSI92].

<b>GSM BS maximum output power levels [dBm]</b>			
<b>900 MHz</b>		<b>1800 MHz</b>	
<b>Macro-cell</b>	<b>Micro<sup>1</sup>-cell</b>	<b>Macro-cell</b>	<b>Micro<sup>1</sup>-cell</b>
[34,58]	]9,24]	[34,46]	]17,32]

<sup>1</sup> Micro-BS maximum output per carrier.

For a worst-case analysis when assessing EMFs around a GSM BS, one should measure the power transmitted by the BCCH carrier (always transmitted at full power), using frequency selective equipment. The maximum possible power is extrapolated by multiplying the measured value by the number of transmitted radio carriers (TRX).

UMTS is based on the Code Division Multiple Access (CDMA) technology, working in Frequency Division Duplex (FDD) and Time Division Duplex (TDD) modes. For the FDD mode, two separate carriers are used for full-duplex, one for UL and another for DL. The TDD mode uses a single carrier for both for UL and DL, unequally allocating the 15 time-slots

between the two links.

Transmission over UMTS makes use of different frequency bands, with a 5 MHz separation between channels:

- [1920, 1980] MHz (UL) and [2110, 2170] MHz (DL) for the UMTS-FDD mode;
- [1900, 1920] MHz and [2010, 2025] MHz (UL/DL) for the UMTS-TDD mode.

In Portugal, each one of the three mobile operators owns 4 FDD carriers and 1 TDD carrier, which can be reused in every cell, subject to controlling the interference between each other.

Standard UMTS BS transmitter maximum output levels, measured as Equivalent Isotropic Radiated Power (EIRP), are presented in Table 2.3.

Table 2.3 - UMTS BSs EIRP [Bena99].

<b>UMTS BSs EIRP [dBm]</b>	
<b>Macro-cell</b>	<b>Micro-cell</b>
[40,43]	[30,33]

When assessing EMFs around a UMTS BS, one must take into account the functioning mode, FDD or TDD. Note that the co-sitting of FDD and TDD BSs is feasible in micro- and pico-cell environments, with antennas shared between both TDD and FDD systems, but in macro-cell environments this is not a commercial and technically viable solution, [HoTo00]. For TDD BSs, the worst-case scenario corresponds to the Tx with maximum power on 14 DL time-slots (1 time-slot is left for UL). For the FDD BSs, the correspondent of the GSM BCCH carrier is the physical pilot channel (CPICH). Typically, the power carried by the CPICH is a fixed percentage of the maximum power transmitted by the BS (usually 10% - 25%), hence, it is enough to measure the power in this channel to estimate the maximum power transmitted by the BS. If user traffic is present, a standard spectrum analyser is not enough and this measurement requires additional features to decode the CPICH channel.

The main differences between GSM and UMTS when evaluating exposure to EMFs have to do with the fact that UMTS introduces new timing features in the power control and in the chip rate. There are spectral peaks at 1500 Hz (FDD) and 100 Hz (TDD) and a more continuous spectrum at low frequencies for the latter; due to the non-constant envelope, there is also a

spectral peak at the chip rate of 3.84 MHz [AnMP01].

For both GSM and UMTS, BS settings allow the output power to be reduced from its maximum level in static radio frequency (RF) power steps, in order to enable the adjustment of the coverage by the operator. In addition to this, downlink RF power control through additional power levels is almost always implemented, meaning that the maximum values presented in Table 2.2 and Table 2.3 are not often attained. In fact, when BSs are installed close to each other, the transmitted power needs to be reduced in order to avoid interference. On the other hand, typical BSs in rural areas, located apart from neighbouring ones, are usually operating at higher power levels. Nevertheless, for the purpose of this thesis, the maximum values, corresponding to the worst-case situation, are considered.

WiFi is based both on the Orthogonal Frequency Division Multiplexing (OFDM) and on the Direct Sequence Spread Spectrum (DSSS), using Carrier Sense Multiple Access-Collision Avoidance (CSMA/CA) access. Currently, there are three main Wireless LAN (WLAN) standards [Bing02]: the IEEE 802.11a, the IEEE 802.11b and the IEEE 802.11g. There are also further standards under development, like IEEE 802.11i or IEEE 802.11e, not detailed here. Table 2.4 presents the specifications of each WiFi standard.

Table 2.4 – European specifications of WiFi standards [Bing02].

	802.11a	802.11b	802.11g
Frequency Band [GHz]	5.150 – 5.350	2.4 – 2.4835	2.4 – 2.4835
Available Bandwidth [MHz]	300	83.5	83.5
Channel Bandwidth [MHz]	20	22	22
Number of Non-Overlapping Radio Channels	12	3	3
Modulation Type / Access	OFDM	DSSS	OFDM

The most common WiFi standard used in Portugal is the 802.11b, with one channel allocated per Access Point (AP). When the coverage area requires more than one AP, it is important to use all the 3 non-overlapping channels in such a way that they do not interfere with each other. Note

that WiFi frequency bands are non-licensed.

The European Telecommunications Standards Institute (ETSI) limits the EIRP of WiFi systems to 20 dBm (100 mW), which is the value established in Portugal. In the United States, the Federal Communications Commission (FCC) sets a maximum EIRP value of 36 dBm, thus, allowing the use of point-to-point and point-to-multipoint wireless links up to some kilometres.

WiMAX refers to a new wireless access technology, resulting from the interoperability of the IEEE 802.16 [IEEE04] and the ETSI HiperMAN [ETSI05] standards. WiMAX promises to deliver up to 70 Mbit/s for each user at up to 50 km in low density, LoS outdoor conditions and at shorter ranges for NLoS situations in cluttered urban environments. The WiMAX Forum [WiMA05], an industry non-profit consortium with about 100 members, is supporting WiMAX technology and promoting its commercial use.

WiMAX technology is based on OFDM techniques (all profiles currently defined by the WiMAX Forum specify a 256-carrier OFDM), working on FDD and TDD modes, and having different channel bandwidths (from 1.25 up to 20 MHz). At present, a major challenge of the WiMAX Forum is the spectrum alignment. The consortium is particularly interested in harmonising the following frequency bands:

- Licensed 2.5 GHz;
- Licensed 3.5 GHz;
- Licensed 5 GHz – Includes the frequency range between 5.25 and 5.85 GHz. This band is strategic for covering underserved, low population density rural and remote markets. In the upper 5 GHz band, many countries allow a maximum of 4 W EIRP for BSs, which makes this band very attractive to WiMAX applications;
- New bands in Lower Frequencies – These frequencies are very interesting, since they allow a lower number of BSs required to cover a given service area, decreasing the deployment costs.

According to [WiMA06], WiMAX BSs will have 2 or 4 antennas for reception (RX) and the same number for TX, with a maximum EIRP of 43 dBm.

Figure 2.6 represents an overview of the spectrum allocation for the wireless communication systems considered in this thesis.

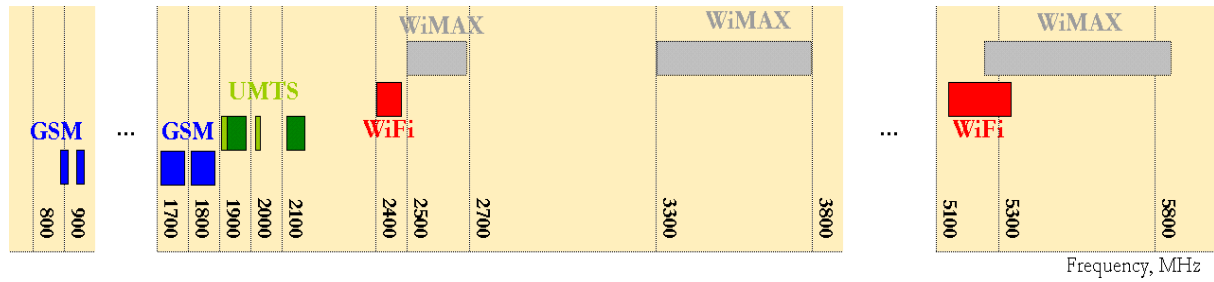


Figure 2.6 – Wireless communication systems spectrum allocation.

## 2.2.2 Characterisation of installations

The deployment of cellular networks is strongly related to the environment of installation. BS antennas must be strategically located in available places where coverage, capacity and interference conditions are balanced in the best way. For example, larger cells cover low traffic density areas (rural environments) and small ones cover high traffic density (urban environments). It is common to classify cells according to the coverage range and the position of BS antennas relative to the neighbouring buildings (if they exist). In [OFRC04], a classification of wireless communication cells is suggested, Table 2.5.

According to the type of infrastructure supporting the antenna and the involving environment, the installations of BS antennas may also be categorised, Table 2.6. This classification is important for the purpose of estimation of exclusion zones around BS antennas, as it allows a relatively precise description of each configuration. The classification proposed here may be extended to WiFi and WiMAX installations (disregarding the column “Cell type”).

As one may observe in Table 2.6, antennas are usually installed high above the ground, being inaccessible to areas where people can stay. However, in “Ufaçade” and “Upole” scenarios, antennas may be accessed through balconies or windows. “Iceil” and “Iwall” are the scenarios where antennas are installed closer to people. It is important to clearly define exclusion zones to avoid human exposure in high-level radiation areas.

In regions with a relatively low number of subscribers, it is common to find an omni BS, requiring one Tx/Rx antenna or even two in case of diversity in RX, Figure 2.7. In high-density zones, for capacity reasons, the typical configuration of BSs consists of three sectors of 120°, Figure 2.8. Each sector constitutes a cell, requiring one Tx/Rx antenna or even two in RX (in



case of diversity in the RX) per system (GSM900, GSM1800 or UMTS). This means that up to three Tx/Rx co-located antennas may be transmitting into a certain direction. If, in addition, more than one operator is sharing the site, even more antennas may be found in the same infrastructure. Antennas might be installed with a mechanical tilt, still being possible to adjust additionally its tilt electrically (electrical tilt), in order to better satisfy coverage and interference requirements.

Table 2.5 – Classification of cells in wireless communications.

Cell		Coverage range	Description
Macro	Large	0.5 – 30 km	Serve either <i>rural</i> or <i>suburban</i> environments, where the density of BSs is small due to low traffic density; antennas are typically installed on high masts, top of high buildings or other structures, using high-radiated power levels to allow a wide coverage area. Propagation is typically over rooftops.
	Small	3 – 30 km	
Micro		50 – 500 m	Provide coverage in <i>urban</i> areas, where requirements in terms of capacity are stringent due to high traffic demand; antennas are strategically installed (small towers, top of lower buildings or façades) radiating medium power levels in order to satisfy the capacity demand in a restricted coverage area, and to avoid interference with neighbouring cells. Propagation is typically below rooftops.
Pico		Few tens of metres	Usually used to increase <i>in-building</i> coverage, where demand is very high; antennas are typically placed on walls and ceilings inside buildings for the coverage of small areas, thus, requiring lower power levels.

Table 2.6 – Classification of BS installations (extracted from [OFRC04]).

Denomination	Cell type	Environment	Installation type	Antenna height [m]
Rtower	Macro	Rural, Suburban	Tower, Mast, Water sump, “Tree”	20 – 40
Uroof	Micro/Macro *	Urban	Roof-top	2 – 5 **
Utower			Tower	3 – 10
Ufaçade	Micro		Building façade	3 – 10
Upole			Light pole or other	3 – 5
Iceil	Pico	In-building	Ceiling	2 – 3
Iwall			Walls	

\*: The cell type will depend on the coverage area

\*\*: Height from the roof top

In indoor environments, there are wideband omnidirectional antennas available, which can be mounted on the ceiling (see Annex A). If used in conjunction with wideband splitters, then an indoor network can be achieved associated to several wireless communications systems. Extremely flat directional antennas can be mounted on walls (see Annex A). The small depth of the antenna is achieved by using patch technology.

There are slightly different WiFi topologies; the simplest arrangement is an ad hoc group of independent wireless nodes communicating on a peer-to-peer basis, in a short-range area. More complex topologies are possible, referred to as infrastructure topologies, including at least one AP. A single AP can manage and bridge wireless communications for all the devices within the range and operating on the same channel. To cover larger areas, multiple APs are deployed, each one being assigned a different channel whenever possible to minimise interference.

WiFi systems employ various types of antennas, offering different coverage capabilities. Usually, omnidirectional, yagis, patch and parabolic dish antennas are used. The omnidirectional antennas,

Annex A, are used in situations requiring a large coverage area, like a warehouse, manufacturing enterprise and large retail environments, also being used indoors in point-to-point links, or outdoors in point-to-multipoint links. High gain directional antennas, like parabolic dishes, Annex A, are used in remote point-to-point LoS links; in indoor situations at back corner offices, against walls, or in long and narrow areas (e.g., long rows of racking), patch or yagis are employed, Figure 2.9 and Annex A. Spatial diversity is commonly used in WiFi systems to overcome fast fading (e.g., in indoor point-to-point links).

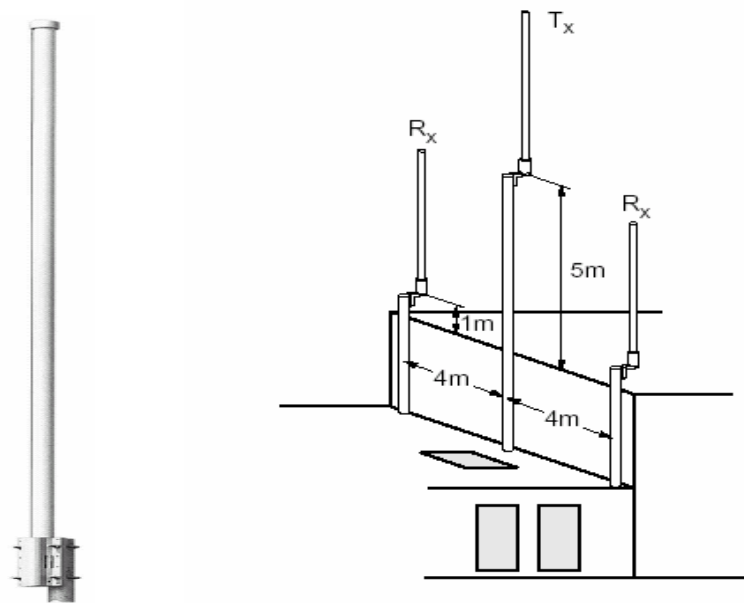


Figure 2.7 – Omnidirectional BS (adapted from [KATH05a]).

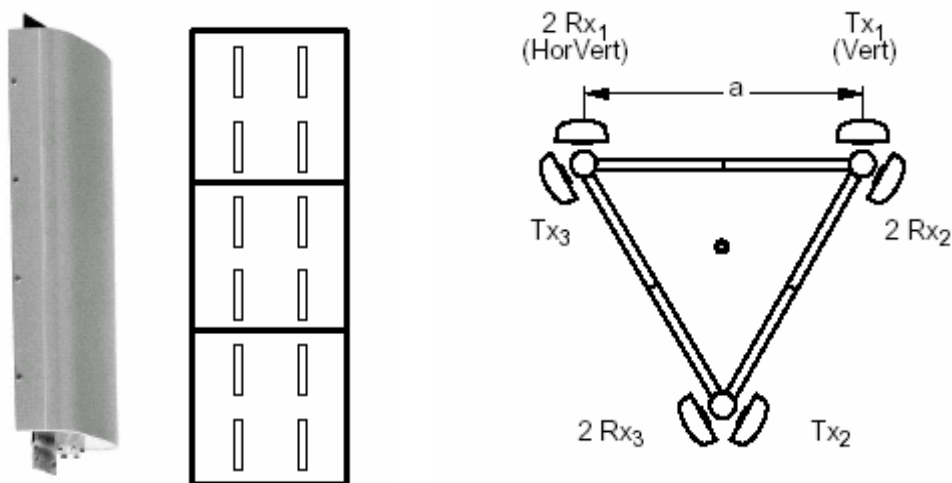


Figure 2.8 – Sector BS antenna (adapted from [KATH05a]).



Figure 2.9 – WiFi patch antenna (extracted from [CISC06b]).

Concerning WiMAX installation topologies, in a first stage it will be implemented outdoors, with the configuration identified in Figure 2.10. A point-to-multipoint topology will be used, where carriers will set up rooftop transceivers as BSs connected to the Internet. Each BS will use WiMAX to communicate with fixed subscriber antennas mounted externally in rooftops or walls. The technology is being upgraded so that customers can use indoor antennas.

WiMAX BSs will use preferentially directional antennas with configurations varying from one RX antenna and three sector cells to two RX antenna and six-sector cells. Diversity schemes are used to minimise multipath and reflection effects that occur in NLoS conditions. Optionally, the WiMAX standard provides the use of adaptive antenna systems, which have beam forming properties that can steer to a particular direction or directions.

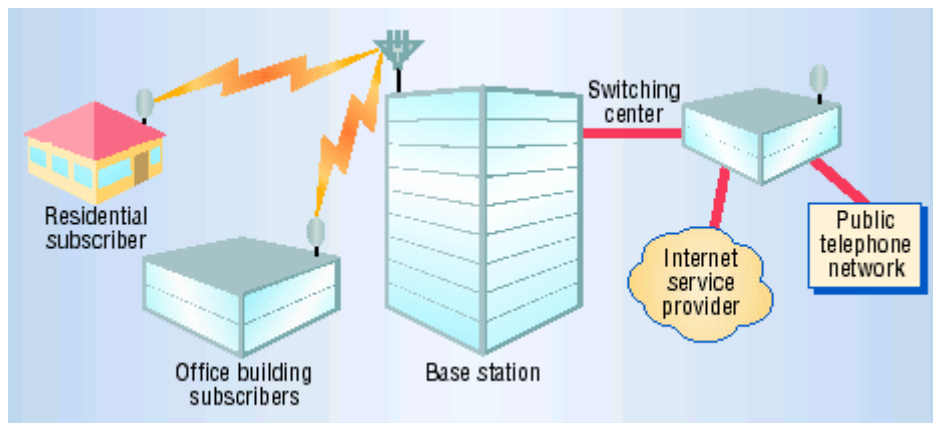


Figure 2.10 – Initial plans for WiMAX topology of installation (extracted from [Vaug04]).

## **2.3 Exposure to electromagnetic radiation**

It is worldwide accepted that the evaluation of human exposure to EM radiation comprises a process of comparison of the exposure levels measured, calculated or simulated against reference levels. A brief overview on the reference levels is presented in this section, going from the basics for the establishment of safety guidelines to the presentation of the reference levels adopted in Portugal. An insight into the main guidelines established by international entities for assessment of EMFs is also given.

### **2.3.1 Exposure guidelines**

The key perspective adopted by the international community for risk management related with EMFs was the adoption of reference levels, which constitute an answer to the question: when are biological effects caused by radiation absorption harmful to health? This way, it can be said that reference levels establish maximum permissible values for radiation absorbed by the human body.

Several national and international entities have established guidelines for limiting EMF exposure, providing protection against known adverse health effects<sup>1</sup>. Portugal, along with most of the European countries, adopted the exposure thresholds established by the European Union Recommendation [CoEU99] for general public. For occupational exposure (occupational population consists of adults exposed under known conditions, being trained to be aware of potential risks), a European directive was recently set up [CoEU04] and must be adopted by all member states until the end of 2008. These standards rely on the International Commission for Non-Ionising Radiation Protection (ICNIRP) guidelines [ICNI98].

The ICNIRP guidelines have been developed following a thorough review of all published literature; only established effects were used as the basis for setting the exposure restrictions. These are short-term, immediate health effects associated to the exposure to frequency sources

---

<sup>1</sup> An adverse health effect causes detectable impairment of the health of the exposed individual; a biological effect, on the other hand, may or may not result in an adverse health effect.

up to 300 GHz; for RF exposure they arise as elevated tissue temperatures resulting from absorption of energy. Two classes of guidance are presented in ICNIRP guidelines, both frequency dependent and including safety factors:

- Basic restrictions: Based directly on established health effects. For RF frequencies, the physical quantity used to specify these restrictions is the Specific Absorption Rate (SAR), which can not be easily measured, as it implies performing measurements inside the body of the exposed individual. Protection against adverse health effects requires that these basic restrictions are not exceeded.
- Reference levels: Defined for practical exposure purposes; the physical quantities used to specify these levels that derive from the basic restrictions are  $E$ ,  $H$ , magnetic flux density ( $B$ ) and  $S$ . Compliance with the reference levels will ensure compliance with the relevant basic restriction. However, whenever a reference level is exceeded it does not imply that the basic restriction has been exceeded, but a more detailed analysis is necessary to assess compliance with the basic restrictions.

The reference levels (unperturbed root-mean-square (rms) values) set by ICNIRP guidelines to the general public are presented in Table 2.7 (only for the frequencies of interest in this thesis). These levels have been obtained from those for occupational exposure by applying various factors over the entire frequency range, being more restrictive than those ones. In the far field zone, only  $E$  or  $H$  need to be measured, as they are related by (2.3). For a conservative approach, these reference levels can be used for near field assessment (by measuring both  $E$  and  $H$ ), since the coupling of energy from the electric or magnetic field contribution cannot exceed the SAR restrictions. For the frequencies of interest in this work, the measured  $E$  and  $H$  values must be time averaged over any 6-minutes period and spatially averaged over the entire body of the exposed individual.

Table 2.7 – ICNIRP reference levels for general public exposure (unperturbed rms values).

Frequency range, $f$	$E$ [V/m]	$H$ [A/m]	$B$ [ $\mu$ T]	$S_{eq}$ [W/m <sup>2</sup> ]
400 – 2000 MHz	$1.375 f^{\frac{1}{2}}$	$0.0037 f^{\frac{1}{2}}$	$0.0046 f^{\frac{1}{2}}$	$f/200$
2 – 300 GHz	61	0.16	0.20	10

Note that, for preventing unintentionally high exposure during the averaging period, the ICNIRP guidelines also provide peak power limits. For frequencies between 10 MHz and 300 GHz, peak

reference values are obtained by multiplying the corresponding rms values by 32.

In situations of simultaneous exposure to fields of different frequencies, the exposure may be additive in its effects. For the frequencies of interest in this work, the following two requirements should be applied to the field levels:

$$\sum_{i>400MHz}^{300GHz} \left( \frac{E_i}{E_{ref_i}} \right)^2 \leq 1. \quad (2.7)$$

and:

$$\sum_{j>400MHz}^{300GHz} \left( \frac{H_j}{H_{ref_j}} \right)^2 \leq 1. \quad (2.8)$$

where:

- $E_i$  – Electric field strength at frequency  $i$  [V/m].
- $E_{ref_i}$  – Electric field reference level from Table 2.7 [V/m].
- $H_j$  – Magnetic field strength at frequency  $j$  [A/m].
- $H_{ref_j}$  – Magnetic field reference level from Table 2.7 [A/m].

### 2.3.2 Measurement guidelines

Measurement guidelines are important tools to assess EMFs for the purpose of comparison against reference levels. Furthermore, they are decisive for comparability and acceptance between different measurement series, as well as for results replication. The harmonisation of measurement methods is a major challenge that European and international standardisation bodies are facing up today.

The “ECC Recommendation (02)04”, [ECCC03], issued by the Electronic Communications Committee (ECC) within the European Conference of Postal and Telecommunications Administrations (CEPT), is being adopted by the majority of the European telecommunications administrations; the Portuguese national telecommunications administration, ANACOM, [ANAC03] has already done so. This recommendation specifies in-situ measurement procedures

to assess non-ionising EMF levels for the purpose of comparison against reference levels, and establishes a structure for reporting measurements. The recommendation states a measuring approach based on the application of various methods, whose accuracy is increased when radiation levels reach the limits.

The European Committee for Electrotechnical Standardisation (CENELEC) issued the EN 50383 standard, [CENE02], aiming to specify the method for assessment of compliance distances around BSs operating in the 110 MHz to 40 GHz frequency range. This standard describes the measurement and calculation methodologies that may be used to establish compliance boundaries in free space conditions, specifying those methodologies for each antenna region, Table 2.8.

Table 2.8 – Reference and alternative methodologies established by the EN 50383 standard, [CENE02].

	Reactive near-field region	Radiating near-field region	Far-field region
Reference	SAR evaluation	SAR evaluation	<i>E</i> -field or <i>H</i> -field calculation
First alternative	<i>E</i> -field or <i>H</i> -field measurement	<i>E</i> -field or <i>H</i> -field measurement	<i>E</i> -field or <i>H</i> -field measurement
Second Alternative	-	<i>E</i> -field or <i>H</i> -field calculation	-

Complementary to the EN 50383 standard, CENELEC is preparing the EN 50400 standard (currently in the form of a draft document, under review), [CENE04], which specifies, for BSs put into service in its operational environment, the method for assessment of compliance in areas where people may have access. Following the definition of compliance boundaries, this standard will be useful to assess the influence of nearby relevant transmission sources or of structures that may cause reflections or diffractions in the total exposure ratio.



## 2.4 Methods for exposure estimation

EMF exposure levels in the vicinity of a BS antenna might be estimated through different methods, with different levels of complexity. In this section, an approach to the assessment of EMF levels is presented, based on an overview of models found in the literature. The survey presented here starts with the theory to estimate exclusion zones, then goes through the calculation of fields in the near-field region, ending with the estimation of field levels in the presence of scattering objects and others.

### 2.4.1 Estimation of exclusion zones

The concept of exclusion zone may be defined as a region around BS antennas where the general public is not allowed to enter, because the EMFs reference levels may be exceeded inside it. In normal conditions, outside the exclusion zone the RF exposure is below the reference levels. Figure 2.11 presents an example of exclusion zone.

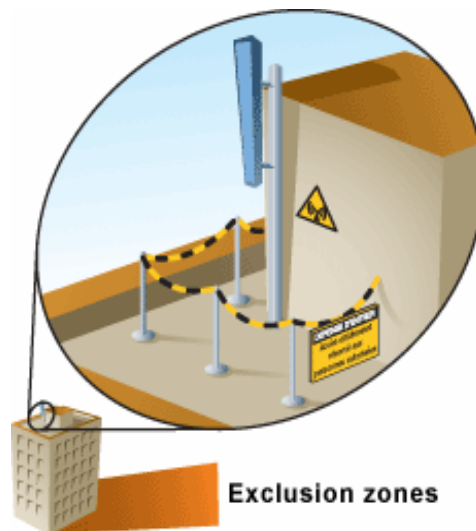


Figure 2.11 – Exclusion zone surrounding a BS antenna (extracted from [OrFr04]).

There are various approaches to solve the problem of estimating exclusion zones around BSs. The simplest method, applicable in situations where the influence of the environment is considered as negligible, is the far-field model:

$$S(d, \theta, \phi) = \frac{P_{in} G(\theta, \phi)}{4\pi d^2}, \quad d \geq \frac{2D^2}{\lambda}. \quad (2.9)$$

where:

- $P_{in}$  – Total power delivered to the antenna terminals.
- $G(\theta, \phi)$  – Generalised antenna gain.

This model is applicable in the far-field region, and overestimates in the near-field one, resulting in including the near-field region inside the exclusion zone even if the field levels inside it are below the reference levels. This means that the exclusion zone is forced to be as large as the far-field distance, which is usually unfeasible, if one considers that for typical BSs the far-field distance is around 20-40 m. So, there is a need to use models that are valid at a closer distance from the antennas.

In [MFRL02], a rigorous but practical BSs assessment procedure is described, whose first stage is to determine the exclusion zone. A model defining a cylindrical exclusion zone for BSs located in free-space areas is presented. The value of  $S$  near the antenna - collinear array of  $N$  half-wave dipoles - is estimated by computing  $S$  on the surface of an imaginary cylinder that extends from the bottom of the lowest element to the top of the highest one, according to:

$$S(d, \theta, \phi) = \frac{P_{in} G(\theta, \phi)}{2D\pi d}, \quad d > \frac{\lambda}{2}. \quad (2.10)$$

The cylindrical exclusion zone is represented in Figure 2.12. Limits for the top and bottom of the cylinder ( $D_{top}$  and  $D_{bottom}$ ) are suggested as being equal to  $0.3 D_{max}$ ,  $D_{max}$  being the maximum distance of the cylindrical exclusion zone (calculated through (2.10)). When a downtilt  $\theta_{dt}$  is used, the following correction of these values is suggested:

$$D'_{top} = D_{top} \cos(\theta_{dt}). \quad (2.11)$$

$$D'_{bottom} = D_{bottom} [1 + \sin(\theta_{dt})]. \quad (2.12)$$

A limit for the back of the cylinder,  $D_{back}$  is also estimated as being equal to  $0.1 D_{max}$ . When the BS has several sector antennas, the total exclusion zone results from the added composition truncated sector cylinders of all the individual exclusion zones.

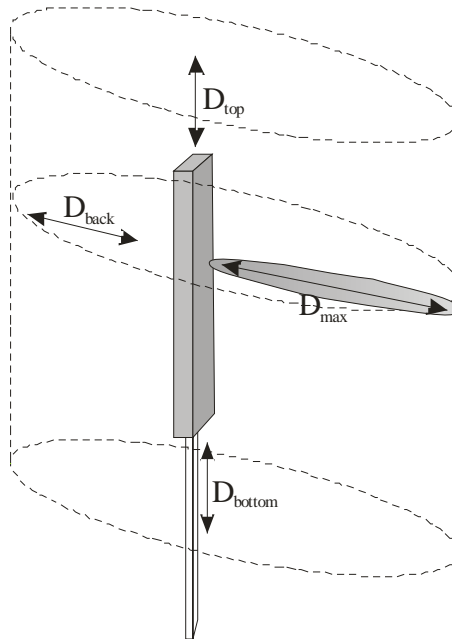


Figure 2.12 – Cylindrical exclusion zone.

Other examples of exclusion zones are the ones considered by [CENE02], which may have simple (parallelepiped, sphere or cylinder) or complex shapes, as the examples of Figure 2.13 and Figure 2.14.

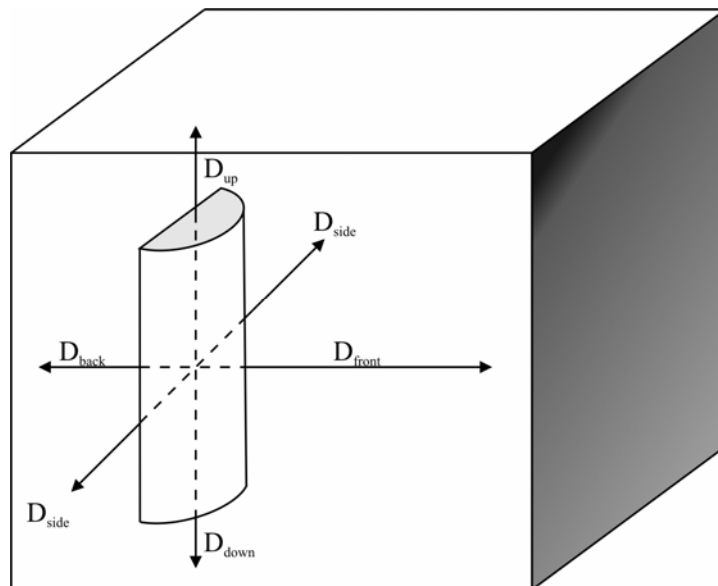


Figure 2.13 – Example of a parallelepiped exclusion zone (adapted from [CENE02]).

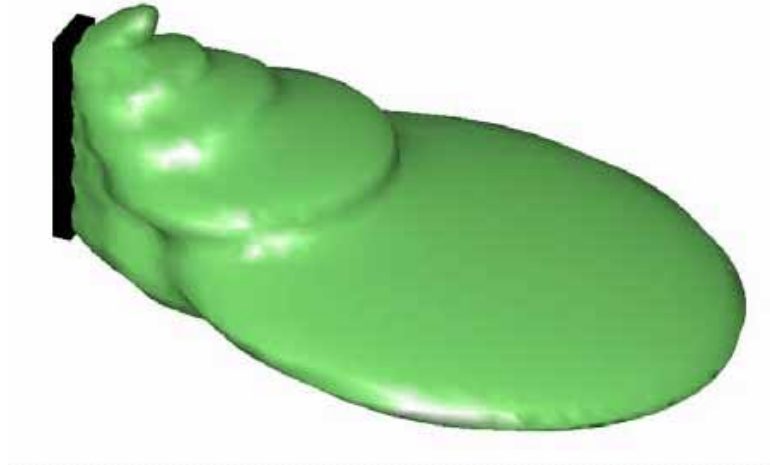


Figure 2.14 – Example of a complex exclusion zone (extracted from [Dane04]).

## **2.4.2 Estimation of EMFs in the near-field region**

The field behaviour in the near-field region is complex and difficult to estimate. Numerical methods [Sadi00] may be applied to solve the problem, such as the MoM, the FEM or the FDTD ones. These methods are based on the solution of Maxwell equations in the time or frequency domains. NEC [NEC05], FEKO [FEKO05] and WIPL-D [WIPL05] are examples of software simulation tools employing the MoM, while Empire [EMPI05] uses the FDTD method.

The MoM determines the field in any point around an antenna for the spatial points of interest, thus, being fast and requiring little computer memory. The most frequent problem related with the application of these methods is the lack of data on the geometry of BS antennas. Additionally, when the external environment is modelled, the dimensions of the region to be studied can be huge compared with the wavelength, thus, requiring unacceptable processing times and available memory. Time-consuming calculations can be avoided by predicting the EMFs using simplified, but accurate methods.

The far-field approximation models are a usual approach, [CENE02], [MNMV02]. For example, [CENE02] considers the use of a cylindrical wave model to evaluate RF fields near vertical collinear dipole antennas. In general, this model is a more accurate predictor of exposure very close to an antenna where the far-field model may significantly overestimate the EMF values. Nevertheless, as one moves away from the antenna, the cylindrical model becomes overly

conservative and the far-field model becomes more accurate. According to this model,  $S$  may be estimated by:

$$S = \frac{P_{in}}{\alpha_{3dB} D d}, \frac{\lambda}{4} \leq d \leq \frac{2D^2}{\lambda}. \quad (2.13)$$

where:

- $\alpha_{3dB}$  – Angle defining the HPBW of a directional antenna (for an omnidirectional antenna  $\alpha_{3dB} = 2\pi$ ) [rad].

In [MNMV02], a comparison between simple formulas based on cylindrical and far-field approximations for calculating exclusion zones and FDTD results is presented. It is concluded that the following expressions can be used to obtain approximate results for the average  $S$  near the array:

$$S(d, \theta, \phi) = \begin{cases} \frac{P_{in}}{\alpha_{3dB} D d}, \frac{D^2}{4\lambda} \leq d < \frac{\alpha_{3dB} G(\theta, \phi) D}{4\pi} \\ \frac{P_{in} G(\theta, \phi)}{4\pi d^2}, d \geq \frac{\alpha_{3dB} G(\theta, \phi) D}{4\pi} \end{cases}. \quad (2.14)$$

As many BS antennas are built as an array of  $N$  dipoles with a reflector behind them, there are also interesting models to estimate exposure taking into account the mutual interference between these dipoles. In [OIMa00], a refined far-field model is proposed, where the antenna is split into different small elements, so that  $E$  in an observation point can be calculated as the superposition of the classical far-field of each element:

$$E = \sum_{i=1}^N \frac{F_i e^{-jkd_i}}{d_i}. \quad (2.15)$$

where:

- $F_i$  – Radiation pattern of the  $i$ -th element.
- $d_i$  – Distance from the centre of the  $i$ -th element to the observation point.

The conditions of validity of this model are:

$$d_i > \frac{2D_i^2}{\lambda}, \forall i. \quad (2.16)$$

and

$$\frac{r_i}{d_i} \ll 1, \forall i. \quad (2.17)$$

where:

- $D_i$  – Largest dimension of the  $i$ -th element.
- $r_i$  – Distance from the centre of the antenna to the centre of the  $i$ -th element.

In order to calculate each  $F_i$ , each  $i$ -th antenna must be excited with a current equal to the current present at these terminals when all elements are excited, but leaving all other ones open. In this way, the radiation pattern of the whole antenna can be constructed from the radiation patterns of the elements.

A similar approach to the preceding method is the far-field-gain-based model described in [BiGi99], which is a fast and efficient method for evaluating EMF levels radiated by BS uniform array antennas in the near-field area. It is assumed that the gain function of the antenna is represented as:

$$G(\theta, \phi) \simeq G_M G_V(\theta) G_H(\phi). \quad (2.18)$$

where:

- $G_M$  – Maximum gain of the antenna.
- $G_V(\theta)$  – Radiation pattern in the vertical plane.
- $G_H(\phi)$  – Radiation pattern in the horizontal plane.

A good estimate of the near-field radiated by the antenna as a combination of the far-field radiated by each element of the array can be obtained by:

$$E(d, \theta, \phi) \simeq \left| \sum_{i=1}^N \frac{\sqrt{30 P_{in} G(\theta_i, \phi_i)}}{d_i} e^{-j\phi_i} \mathbf{u}(\theta_i, \phi_i) \right|, d > 3\lambda. \quad (2.19)$$

and

$$G(\theta_i, \phi_i) \simeq \frac{G_M G_{Ve}(\theta) G_{He}(\phi)}{N}. \quad (2.20)$$

$$\varphi_i = (i-1)\varphi + \frac{2\pi d_i}{\lambda}. \quad (2.21)$$

where:

- $(d_i, \theta_i, \phi_i)$  – Spherical co-ordinates centred at the  $i$ -th element of the array.
- $\mathbf{u}(\theta_i, \phi_i)$  – Unitary vector of the  $i$ -th element.
- $G_{V_i}(\theta)$  – Element radiation pattern in the vertical plane.
- $G_{H_i}(\phi)$  – Element radiation pattern in the horizontal plane.
- $\varphi_i$  – Phase difference between the element feeding coefficients.

This paper presents a two-step method to determine the radiation pattern of each  $i$ -th element of the array. Results were assessed with NEC simulations, presenting good agreement for distances above three wavelengths. Nevertheless, the environment topology is not considered, in particular the surrounding buildings, which may have an effect on the field levels.

In [ABDK02], two simple and accurate models are presented, having similarities with the above ones. One of them is the synthetic model, which calculates the radiated near-field of one unit cell of the antenna array in the volume of interest. The near-field of the full antenna is derived by superposing horizontally shifted contributions of the unit cell. The other model proposed in this paper is the gain-based model, derived from the synthetic model by computing the gain pattern of one unit cell for all angles, and storing it in computer memory. The near-field of the full antenna is then approximated as the sum of the far-field contributions of its shifted unit cell. The gain-based model approximates reasonably well the near-field from a distance of about two wavelengths, requiring small time and memory resources.

A different approach to estimate exposure in the near-field region is by using spherical/cylindrical near-field transformations, allowing for examination at very short distances to the antenna [BIRC02] and also closely behind the antenna [Frid03]. Spherical near to far-field transformation is a standard antenna measurement technique employed to obtain the antenna far-field pattern from a near-field measurement. The near-field measurement can also be employed to obtain a very good estimate of  $S$  in the vicinity of the antenna, thus, allowing the definition of exclusion zones. In [Frid03], it is stated that a combination of spherical and cylindrical near-field transformations techniques is well suited for exposure assessment of panel antennas.

### **2.4.3 Influence of the surrounding environment**

When a BS antenna is put into service on its operational environment, the exclusion zone calculated in free space conditions may be redefined. This may happen because of the presence of surrounding objects (*e.g.*, the physical barrier interdicting access to the area around BS antenna, building walls, etc.), which modify EMFs in the region around the antenna. The analysis of this problem is not a simple matter, as generally it requires calculating EMF levels in the near-field region. Moreover, it is necessary to take into account the reflected, transmitted and refracted fields caused by the presence of the various surrounding scattered or reflector objects. A combination of different exposure assessment methods is used to analyse this situation.

The techniques of ‘rigorous’ numerical modelling may be used to study the problem, But, as stated in the previous section, the main problem of these tools when modelling the external environment is that the dimensions of the region to be studied can be huge compared with the wavelength, thus, requiring unacceptable processing times and available memory.

In the literature, one can find some studies that evaluate human exposure in the case where the BS antenna is near obstacles, [BCPP00], [NMMV01], [BCCP03]. These studies are focused on the estimation of SAR values in the far-field region of the considered BS antenna. They propose hybrid techniques, which start to evaluate the EMFs incident on the exposed subject by using ray tracing techniques, then employ the FDTD method to analyse fields inside the body.

Other studies, dedicated to the specific problem of this thesis are also found in the literature, [BCFF99], [Wojc02], [Dane04]. All of them consider the use of more or less complex ray tracing techniques, which are based on the GO hypothesis. Under the GO approach, the wavelength is assumed to be very small compared to the environment dimensions, so propagation is considered to take place by “rays” originated in the antenna site, experiencing straight line propagation in free space. Each ray is associated to a local plane wave, which can experience reflection, transmission and diffraction due to the presence of obstacles. Obstacles are modelled as a set of basic homogeneous scattered elements, described by their EM properties: dielectric constant, magnetic permeability, and conductivity. The GO approach allows determining the EMFs of reflected and transmitted rays, through the well-known Fresnel coefficients. The GTD and the UTD extend the GO applicability domains to rays diffracted by edges and corners. Ray tracing techniques determine the different paths taken by the rays, with a precision dependent on a limiting number of successive scattering actions a ray can experience. The total EMF level at a



specific point is the sum of all the EMFs caused by the different rays:

$$E_{tot} = E_{direct-ray} + E_{reflected-ray} + E_{transmitted-ray} + E_{diffracted-ray} . \quad (2.22)$$

where:

- $E_{tot}$  – Total electric field strength at the investigation point.
- $E_{direct-ray}$  – Electric field strength caused by the direct ray.
- $E_{reflected-ray}$  – Electric field strength caused by the reflected ray.
- $E_{transmitted-ray}$  – Electric field strength caused by the transmitted ray.
- $E_{diffracted-ray}$  – Electric field strength caused by the refracted ray.

In [Wojc02], a method for evaluation of near field of GSM BS antennas in urban environment is presented. The method is based on the replacement of a panel antenna by a linear discrete array. Moreover, the GO approach is used to evaluate the influence of the environment, thus, neglecting edge diffractions.

The total EMF in a point is obtained as a sum of the fields radiated by each of the  $N$  individual sources calculated using far-field equations:

$$E_{tot} = \left| \sqrt{\frac{30P}{N}} \sum_{i=1}^N \frac{\sqrt{G(\theta_i, \phi_i)}}{d_i} e^{-jkd_i} \hat{u}(\theta_i, \phi_i) \right| . \quad (2.23)$$

The phase shifts arising from different distances between particular sources and the observation point are included. The gain pattern of each unit source may be approximated by:

$$G(\theta, \phi) = \begin{cases} G_M \sin^m(\theta) \cos^n\left(\frac{\phi}{2}\right), & -90^\circ < \phi < 90^\circ \\ 0 & \text{elsewhere} \end{cases} . \quad (2.24)$$

The comparison between the results obtained with the proposed method and with a full wave analysis proved the accuracy of the method. This model is employed in the software tool EMF Visual [ANTE04].

In [BCFF99], a hybrid prediction algorithm is proposed for the evaluation of field strength distributions near BS antennas. It combines three different propagation models used in different areas around the antenna: very near the antenna, in the far field region, and in the region that lies between the two previous ones. This algorithm considers a typical vertical array antenna with  $N$

elements, where each element is composed of a couple of dipoles placed in front of a plate, Figure 2.15. The element is represented by the single dipole.

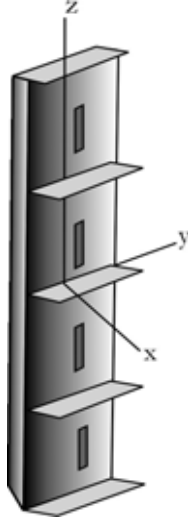


Figure 2.15 – Scheme of a typical 4-element GSM antenna.

For the first region ( $d \ll \lambda$ ), the spherical waves triples model [Sche43] enables to evaluate the exact value of the electrical field radiated by a dipole as the sum of the field radiated from three different sources of spherical non-uniform waves, located in the middle and at the extremes of the dipole. It allows an accurate prediction in both the near and far-field regions of the antenna. The influence of the environment is neglected in this area.

For the second region, corresponding to  $d \ll 2D^2/\lambda$ , the element radiation pattern antenna model [CGLM99] is combined with a ray-tracing propagation tool. At a given point, the total field is evaluated as the sum of all different contributions originated from each single element, which is assumed as an independent non-uniform spherical source. The effect of reflections and diffractions due to obstacles near the antenna is accounted for through the combination of this antenna model with a 3D ray-tracing algorithm. This ray-tracing algorithm is based on GO and UTD. The total field is a vectorial sum of all contributions, *i.e.*, all the rays reaching the receiver after a number of interactions with obstacles:

$$E_{tot} = \sum_{i=1}^N \sum_{j=1}^{N_R} \overline{E_{ij}}. \quad (2.25)$$

where:

- $N_R$  – Number of propagation rays associated to each antenna element.

- $\overline{E_{ij}}$  – Electric field including the effect of free space propagation, reflections, transmissions and diffractions, weighted by the antenna radiation pattern.

For the area corresponding to the far-field region ( $d > 2D^2/\lambda$ ), the same ray-tracing algorithm is employed, but considering the BS antenna as a single source, thus, using the overall radiation pattern. If the antenna is located in an open area, one can simply employ the free space propagation formula. In this third region, propagation phase deviations are neglected, so an overestimation of field amplitude is possible if all the antenna elements are fed in-phase and if the observation point is close to the azimuth plane.

To study the influence of the geometrical environment and of the antenna characteristics, different BS installations were considered both in rural and urban areas. The reliability of this hybrid prediction tool has been assessed with measurements. Based on this tool, an exclusion zone was derived as being a parallelepiped volume around the antenna symmetric to maximum radiation direction. A preliminary evaluation of this precautionary volume is proposed, where distances for the different axis of this volume are specified for different installation types (mast, roof of a rural building, roof of an urban building with and without surrounding buildings). It is stated that the proximity of surrounding buildings might increase the volume.

[Dane04] studies the possible alterations of the compliance boundary of a BS antenna due to the presence of other radio sources and scattering objects in the vicinity. The influence of other radio sources is analysed through broadband and frequency selective measurements. The effect of scattering objects is analysed both numerically, through simulations performed with FEKO and with the EMF Visual softwares, and by performing broadband and frequency selective measurements on a real UMTS site. It is stated that co-located radio sources have insignificant effects on the compliance boundary, as well as the presence of surrounding objects close to the antenna, but outside its main beam. The worst scenario occurs when a reflecting object is present inside a horizontal sector with an angle twice the HPBW (typically 130°), extending the compliance boundary less than 25%.

It is important to refer that, although all the literature overview presented in the last three sections deals with panel antennas for cellular systems, the results can be extended to other types of antennas and for other systems. In a first approach, other antenna types (dish, Yagi, horn) can be modelled by giving their far field radiation patterns. On going research is being carried out to develop more sophisticated models for those other kind of antennas for the near field region.



# Chapter 3

## Numerical Methods

This chapter concerns the numerical method employed in this thesis to solve the problem of evaluating EMFs in any point of interest around an antenna. Section 3.1 briefly describes the theoretical aspects of the Integral Equation and the Method of Moments. Section 3.2 explains how these methods are implemented in the software tool WIPL-D, which is a tool to analyse metallic and dielectric structures. Section 3.3 presents the practical results achieved from the application of WIPL-D to the numerical simulation of a GSM900 BS antenna.

### **3.1 Integral Equation – Method of Moments**

The accurate evaluation of EMFs around an antenna in the presence of neighbouring objects should start by modelling the geometry of the problem. In order to obtain satisfactory near-field results, both the antenna and scatterers should be geometrically described exactly or approximately, by means of interconnected surface elements. For BS antennas, this may be a complicated task, as manufacturers do not use to provide information on the internal configuration / geometry of the antennas. Figure 3.1 and Figure 3.2 depict the inside configuration of common BS antennas employed in GSM and UMTS BSs, and Figure 3.3 represents the internal configuration of a WiFi AP antenna.



Figure 3.1 – Inside configuration of a GSM antenna (extracted from [KATH06]).

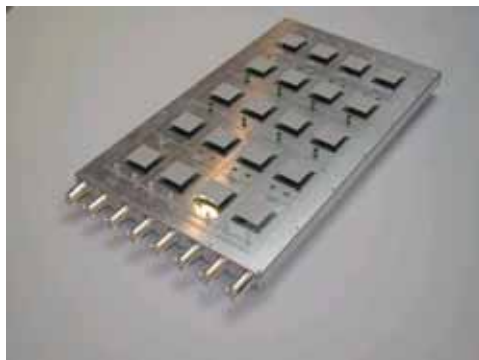


Figure 3.2 – Inside configuration of a UMTS antenna (extracted from [KTHS06]).



Figure 3.3 – Inside configuration of a WiFi antenna (extracted from [CISC06a]).

A second step for EMF evaluation is to determine the distribution of currents over the (exact or approximate) geometrical model. If one knows the voltage at the feeding terminals of an antenna and finds the current distribution, then the input impedance and radiation pattern can be obtained. In the same way, if a wave impinges upon the surface of a scatter, a current density is induced, from which one can find the scattered field. So, the main goal of the analysis is to determine the surface current distribution over the structure.

Estimation of currents may be obtained from numerical solution of an integral equation. The objective of integral equations methods is to cast the solution for the unknown current density in the form of an integral equation where the unknown induced current density is part of the integrand. The integral equation is then solved by using numerical techniques such as the MoM [Harr93]. For time-harmonic EMFs, a popular equation, applicable to both open and closed bodies, is the *Electrical Field Integral Equation* (EFIE) [Bala89], which enforces the boundary condition on the tangential  $E$  field.

For radiation problems, especially for wire antennas, two popular EFIEs are the *Pocklington Integral Equation* [Pock97] and the *Hallén Integral Equation* [Hall38], expressed in (3.1) and (3.2) for a cylindrical antenna of length  $l$  and radius  $a$ , Figure 3.4. Hallén’s equation is usually restricted to the use of a *delta gap* voltage source at the feed of a wire antenna. Delta-gap assumes that the excitation voltage at the feed terminals is of a constant  $V_i$  value and zero elsewhere.

Pocklington's equation is more general, and it is adaptable to many types of feed sources, including the magnetic frill generator (this generator replaces the feed gap by a circumferentially directed magnetic density that exists over an annular aperture). Additionally, Hallén's equation requires the inversion of an  $M + 1$  order matrix (where  $M$  is the number of divisions of the wire) while Pocklington's equation requires the inversion of an  $M$  order matrix.

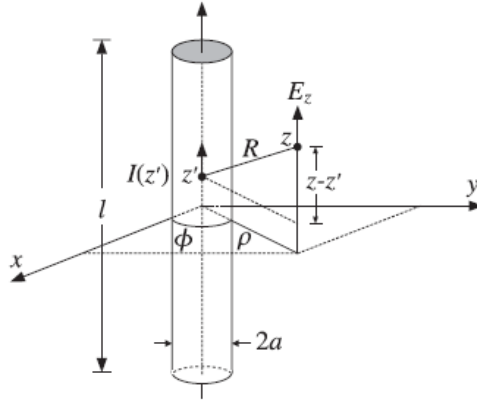


Figure 3.4 – Thin-wire model of cylindrical antenna.

$$\frac{\mu}{4\pi} \int_{-l/2}^{l/2} I(z') G(z - z') dz' = -j\omega\mu\epsilon \left( \partial_z^2 + k^2 \right)^{-1} E_{in}(z). \quad (3.1)$$

where:

- $I(z')$  – Current distribution along the wire antenna.
- $G(z - z') = \frac{e^{-jkR}}{R}$ .
- $R = \sqrt{(z - z')^2 + \rho^2}$ .
- $\omega$  – Angular frequency.
- $\mu$  – Relative permeability.
- $\epsilon$  – Relative permittivity.
- $E_{in}(z)$  – Incident electric field.



$$\frac{\mu}{4\pi} \int_{-l/2}^{l/2} I(z') (\partial_z^2 + k^2) G(z - z') dz' = -j\omega\mu\epsilon E_{in}(z). \quad (3.2)$$

Generally, an EFIE is a deterministic equation of the form:

$$F(g) = h. \quad (3.3)$$

where  $F$  is a known linear operator,  $h$  is a known excitation function, and  $g$  is the response function. The objective is to determine  $g$  once  $F$  and  $h$  are specified. The MoM [Harr93] is a numerical technique to solve this problem, which requires the expansion of the unknown function as a linear combination of  $N$  terms, being written as:

$$g \simeq \sum_{n=1}^N a_n g_n. \quad (3.4)$$

Each  $a_n$  is an unknown constant and each  $g_n$  is a known *basis function*. Substituting (3.4) in (3.3) and using the linearity of the operator  $F$ , one has:

$$\sum_{n=1}^N a_n F(g_n) = h. \quad (3.5)$$

The expansion of (3.5) leads to one equation with  $N$  unknowns, which is not sufficient to determine the  $a_n$  unknown constants. In order to obtain the  $N$  linearly independent equations, to resolve the  $N$  unknown constants, boundary conditions (*e.g.*, vanishing tangential  $E$  field on the surface of an electric conductor) are applied at  $N$  different points, through a point-matching technique. By doing this, (3.5) takes the form of:

$$\sum_{n=1}^N a_n F(g_n) = h_m, \quad m = 1, 2, \dots, N. \quad (3.6)$$

In matrix form, (3.6) can be expressed by:

$$[Z_{mn}][I_n] = [V_m]. \quad (3.7)$$

where:

$$Z_{mn} = F(g_n) - \text{Antenna's input impedance}. \quad (3.8)$$

$$I_n = a_n - \text{Antenna's current.} \quad (3.9)$$

$$V_m = h_m - \text{Potential at antenna's terminals.} \quad (3.10)$$

The unknown  $a_n$  coefficients can be found by solving (3.7), using matrix inversion techniques:

$$[I_n] = [Z_{mm}]^{-1} [V_m]. \quad (3.11)$$

The computational effort required to implement the MoM should be minimised by a correct choice of basis functions. Basis functions should accurately represent and resemble the anticipated unknown function, while minimising calculations effort. Sub-domain functions, such as piecewise constant, piecewise linear or piecewise sinusoid, are the most common type of basis functions, as they may be used with no prior knowledge of the function that they must represent. Entire domain basis functions, as sinusoidal functions, may also be used, especially in problems where the unknown function is assumed *a priori* to follow a known pattern.

In order to improve the point-matching solution, *weighting / testing functions*  $w$  may be used, (3.12). Similar weighting and basis functions should be used to achieve computational simplicity. A well-known technique, known as the *Galerkin's method* [KaAk64], uses the same weighting and basis functions, that is to say  $w_m = g_n$ .

$$\sum_{n=1}^N a_n \langle w_m, F(g_n) \rangle = \langle w_m, h \rangle, m = 1, 2, \dots, N. \quad (3.12)$$

In the literature, one can find several matrix methods for solving field problems. [Harr67] gives a unified treatment of matrix methods for field problems, based on the MoM. The problem of radiation and scattering by wire objects of arbitrary shape is treated in detail, establishing basic concepts that can be generalised to apply to objects of arbitrary geometry and materials. A simple numerical procedure for treating problems of scattering by arbitrarily shaped objects is presented in [RaWG82]. Planar triangular surface patches model the objects, and a corresponding EFIE is derived. In [KoPo93], an entire-domain Galerkin method for analysis of metallic antennas and scatterers is presented. Here, the antenna and scatterers are approximated by generalised quadrangles and the general form of the corresponding EFIE is derived. Two methods are proposed, one intended for the analysis of generalised structures and another aimed at the analysis of spherical scatterers. A more sophisticated method is presented in [Kolu99], where the

author analyses arbitrary composite metallic and dielectric structures, by solving systems of *Surface Field Integral Equations* (SFIEs), using an entire-domain Galerkin method. The method employs efficient basis functions that automatically satisfy continuity equations on surfaces boundaries. The method is validated by examples of scatterers and antennas.

### 3.2 WIPL-D software application

WIPL-D [WIPL05] is a commercial numerical EM code allowing to model general 3D structures, like antennas and scatterers. The structure under analysis is characterised by equivalent surface electric currents over metallic portions and over dielectric material surfaces. The MoM is used to obtain the solution in the frequency domain.

First, the geometry of the composite structure to be analysed is defined through an appropriate combination of wires and plates, which may characterise metallic or lossy/lossless dielectric/magnetic surfaces. Wires can be cylindrical or conical, Figure 3.5, with current existing only over their surface, flowing along the main axis of the object with a distribution that does not depend on its circumferential coordinate. Plates are bilinear surfaces, Figure 3.6, infinitesimally thin and made of a perfect conductor. The program allows wire-to-plate, wire-to-wire and plate-to-plate junctions, applying boundary conditions to these junctions.

The parametric equation of the wire surface is written in the form:

$$r(p, s) = r_a(s) + a(s)i_\rho(p). \quad (3.13)$$

where:

- $s$  – Local coordinate along the reference-cone generatrix.
- $p$  – Local coordinate about the cone axis measured from the  $x$ -axis.
- $i_\rho(p)$  – Radial unit vector in the local coordinate system perpendicular to the cone axis.
- $r_a(s) = r_1 + (s - s_1) \frac{r_2 - r_1}{s_2 - s_1}.$
- $a(s) = a_1 + (s - s_1) \frac{a_2 - a_1}{s_2 - s_1}.$

- $r_1$  and  $r_2$  – Position vectors.
- $a_1$  and  $a_2$  – Radii of cone end beginning and ending, respectively.

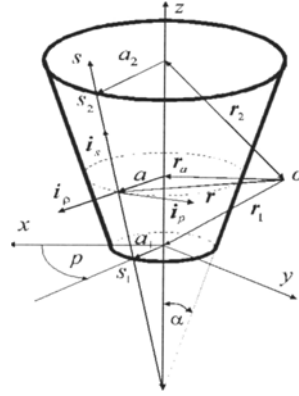


Figure 3.5 – Geometrical definition of a wire (right-truncated cone) in WIPL-D (extracted from [WIPL05]).

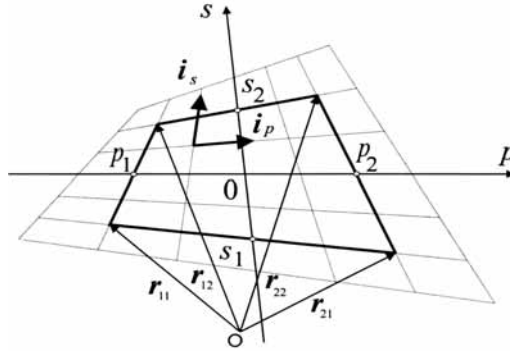


Figure 3.6 – Geometrical definition of a plate (bilinear surface) in WIPL-D (extracted from [WIPL05]).

The parametric equation of a plate (nonplanar quadrilateral) is written in the form:

$$r(p, s) = \frac{1}{\Delta p \Delta s} \left[ r_{11}(p_2 - p)(s_2 - s) + r_{12}(p_2 - p)(s - s_1) + \right. \\ \left. + r_{21}(p - p_1)(s_2 - s) + r_{22}(p - p_1)(s - s_1) \right] \quad (3.14)$$

where:

- $r_{11}, r_{12}, r_{21}$  and  $r_{22}$  – Position vectors of the vertices (Figure 3.6).

- $p_1, p_2, s_1$  and  $s_2$  – Starting coordinates of the quadrilateral sides in the local coordinate system adopted (Figure 3.6).
- $\Delta p = p_2 - p_1$ .
- $\Delta s = s_2 - s_1$ .

WIPL-D analyses both metallic and dielectric structures, allowing the user to define different *domains*, *i.e.*, groups of bodies made of the same material. The electric properties of these domains are characterised by:

- Complex relative permittivity,  $\epsilon = \epsilon_r + j\epsilon_i$ .
- Complex relative permeability,  $\mu = \mu_r + j\mu_i$ .
- Conductivity,  $\sigma$ .

In WIPL-D, antennas are excited by one of two types of voltage generators:

- Delta-function generator (delta-gap excitation);
- Coaxial line generator (magnetic frill excitation).

After the physical definition of the problem, currents are modelled based on the solution of the EFIE. (3.15) and (3.16) express the solution for metallic wires and plates, respectively.

$$E = -j\omega\mu_0 \left\{ \cos(\alpha) i_z \int_{s_1}^{s_2} I(s) g(R_e) ds + \frac{1}{k_0^2} \int_{s_1}^{s_2} \frac{dI(s)}{ds} \text{grad}(\mathbf{R}_e) \frac{dg(\mathbf{R}_e)}{dR_e} ds \right\}. \quad (3.15)$$

where:

- $\mu_0$  – Free space permeability.
- $\alpha$  – Angle between a cone axis and a cone generatrix, for a truncated cone.
- $I(s)$  – Total current flowing along the cone.
- $R_e$  – Medium distance between the source point and the points of investigation belonging to the cone circumference that corresponds to the  $s$ -coordinate.
- $k_0 = \omega\sqrt{\epsilon_0\mu_0}$  – Free space propagation constant.

$$E = -j\omega\mu_0 \left\{ \int_S J_s g(R) dS + \frac{1}{k_0^2} \int_S \text{div}_s J_s i_R \frac{dg(R)}{dR} dS \right\}. \quad (3.16)$$

where:

- $J(s)$  – Surface current density.
- $g(R) = \frac{e^{-jk_0 R}}{4\pi R}$  – Free-space Green's function.
- $R = |\mathbf{R}| = |\mathbf{r}' - \mathbf{r}(p, s)|$  – Distance between the point of investigation and the source point.
- $\mathbf{r}'$  – Position vector of the point of investigation.
- $\mathbf{r}(p, s)$  – Position vector of the source point.
- $\mathbf{i}_R = \frac{\mathbf{R}}{R}$  – Unit vector directed from the source to the field point.

Any composite structure, metallic or dielectric, can be represented as the EM system consisting of a finite number of finite-size linear, homogenous, and isotropic regions, situated in an unbounded linear, homogeneous, and isotropic environment. According to the equivalence theorem [Bala97], the main goal of the analysis of composite structures is to determine electric currents over metallic surfaces and equivalent electric and magnetic currents over dielectric boundary surfaces. Given the impressed fields for two different domains, equivalent electric and magnetic currents placed over the dielectric boundary surface are uniquely determined from the boundary conditions for tangential field components, as expressed in (3.17) and (3.18). Resulting field vectors inside each domain are produced by unknown equivalent currents, expressed through a system of SFIEs. For the case of two domains, a system of two SFIEs, also known as *Poggio, Miller, Chang, Harrington, and Wu* formulation (PMCHW), is obtained. When metallic objects are included, the two PMCHW and an EFIE (resulting from boundary condition for tangential component of  $E$  at metallic-to-dielectric boundary) must be solved. Equivalent electric and magnetic currents placed over dielectric boundary surfaces are approximated in the same way as electric currents placed over metallic surfaces. A detailed explanation of this method is presented in [WIPL05].

$$\left[ E^{(1)} + E_i^{(1)} \right]_{\tan} = \left[ E^{(2)} + E_i^{(2)} \right]_{\tan} . \quad (3.17)$$

$$\left[ H^{(1)} + H_i^{(1)} \right]_{\tan} = \left[ H^{(2)} + H_i^{(2)} \right]_{\tan} . \quad (3.18)$$

where:

- $E_i^{(j)}$  – Impressed electric field in domain 1.

- $E_i^{(2)}$  – Impressed electric field in domain 2.
- $H_i^{(1)}$  – Impressed magnetic field in domain 1.
- $H_i^{(2)}$  – Impressed magnetic field in domain 2.
- $E^{(1)}$  – Resulting electric field in domain 1.
- $E^{(2)}$  – Resulting electric field in domain 2.
- $H^{(1)}$  – Resulting magnetic field in domain 1.
- $H^{(2)}$  – Resulting magnetic field in domain 2.

For both metallic and composite structures, currents are approximated by a finite sum of known functions multiplied by unknown coefficients. These coefficients are obtained by applying the MoM to the EFIE or to the system of SFIEs. Approximation of currents along wires and over plates is performed in two steps. In a first analysis, current expansions for single elements are adopted. Then, these starting current expansions are modified to satisfy the continuity equation at element interconnections and at free ends. WIPL-D uses the Galerkin test procedure. The coefficients for the current expansion are obtained by solving the system of linear equations using L - U decomposition [Ho]085].

WIPL-D uses efficient basis functions that automatically satisfy the continuity equation, assuming that there are no line charges at surface edges. Currents along wires are approximated by polynomials that automatically satisfy continuity at wire ends and junctions. The continuity equation at junction of two or more wires is satisfied by grouping the corresponding node basis functions into doublets (triangle basis functions). The surface current over a bilinear surface is decomposed into its  $p$  and  $s$ -components. As the  $p$ -current components can be treated as the  $s$ -current component defined over the same bilinear surface with interchanged  $p$  and  $s$  coordinates, the program treats the distribution of surface currents as a sum of  $s$ -components defined over bilinear surfaces which overlap or are interconnected. Generally, an entire-domain approximation of currents, along a complex wire-to-plate structure, can be represented as a combination of overlapping doublets and singletons. In the case of lowest-order approximations, the entire-domain expansion degenerates into the classical sub-domain expansion, containing triangle doublets and rooftop basis functions.

Once the unknown coefficients of current expansion are determined, currents along any wire or plate can be evaluated in a particular grid of points of interest. Therefore, near and far field evaluation may be performed, as well as the study of impedance, admittance and s-parameters.

Further details of the theoretical basis of WIPL-D are well described on its user's manual, [WIPL05].

### **3.3 Antenna simulation using WIPL-D**

The 736 624 Kathrein indoor directional antenna [KATH05b] was chosen as an example of a real antenna to be studied, Figure 3.7. The 736 624 Kathrein antenna operates in the GSM900 frequency band, its technical characteristics being presented in Table 3.1, and the horizontal and vertical radiation patterns in Figure 3.8. Figure 3.9 shows the internal components of the antenna under study.

Table 3.1 – Technical characteristics of the 736 624 Kathrein antenna (extracted from [KATH05b]).

Frequency range	870–960 MHz
VSWR	< 1.5
Gain	7 dBi
Impedance	50 $\Omega$
Horizontal HPBW	90°
Vertical HPBW	65°
Polarisation	Vertical
Max. Power	50 W (@ 50°C ambient temperature)
Dimensions (height/width/depth)	205/155/32 mm

Detailed information on the technical characteristics and actual configuration of the antenna,



which were not available, were kindly provided by Kathrein, thus, allowing to adequately model the antenna. Based on the information gathered from Kathrein, three simple geometric models of the antenna were developed using WIPL-D, being analysed and compared in terms of radiation pattern and impedance. One of those models was chosen and used in the various simulation scenarios described in the next chapter. Further information on the models created for simulation of the antenna can be found in Annex B.



Figure 3.7 – The 736 624 Kathrein antenna (extracted from [KATH05b]).

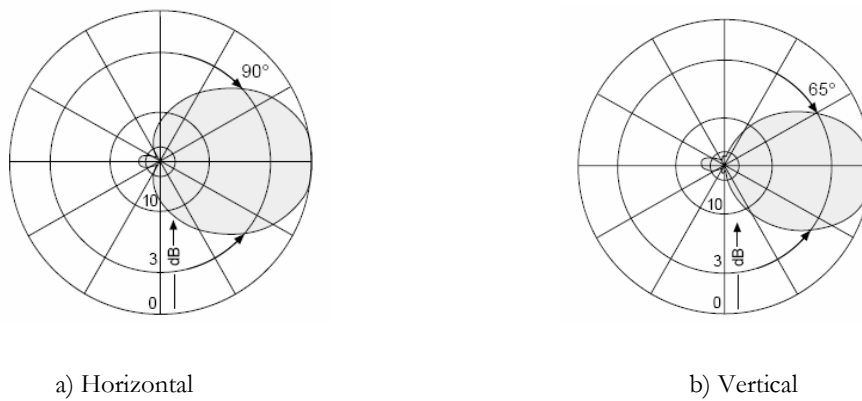


Figure 3.8 – 736 624 Kathrein antenna radiation patterns (extracted from [KATH05b]).

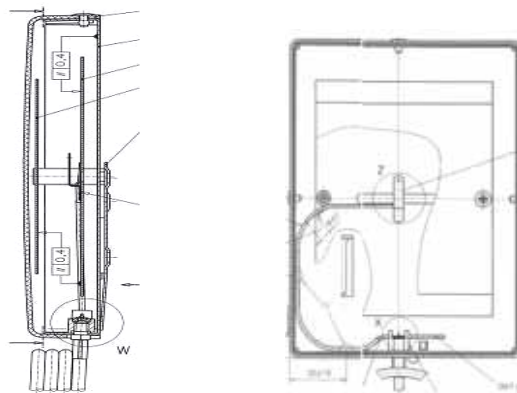


Figure 3.9 - Internal parts of the 736 624 Kathrein antenna (side and front views) [KATH05c].

The geometry of the chosen model of the antenna is based on three metallic plates, fed by a generator on the central one, Figure 3.10. It is a simple model, based both on the available information and on a trade-off between the quality of results and the number of problem unknowns.

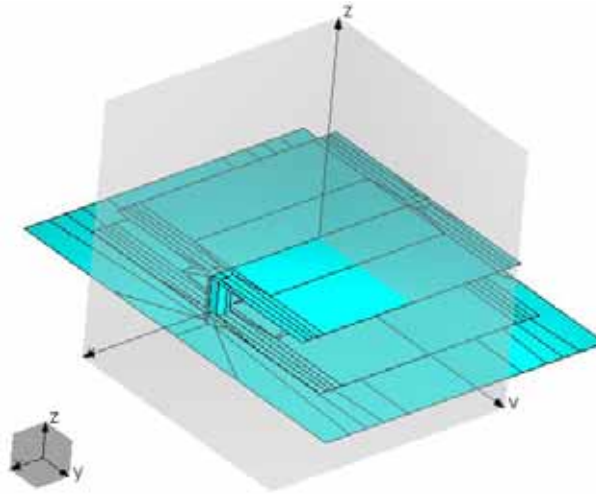


Figure 3.10 – Model for simulation of the 736 624 Kathrein antenna.

In terms of simulated results achieved for this model, one can observe the obtained 3D radiation pattern in Figure 3.11. Moreover, Figure 3.12 presents the return loss (RL) curve of the simulated model, where one can observe matched impedance at 900 MHz, with  $RL < 5.55$  dB ( $VSWR < 3.24$ ) for the overall band of interest. Table 3.2 presents a comparison of parameters obtained through WIPL-D simulation ( $f = 902.5$  MHz) with the parameters provided by the manufacturer.

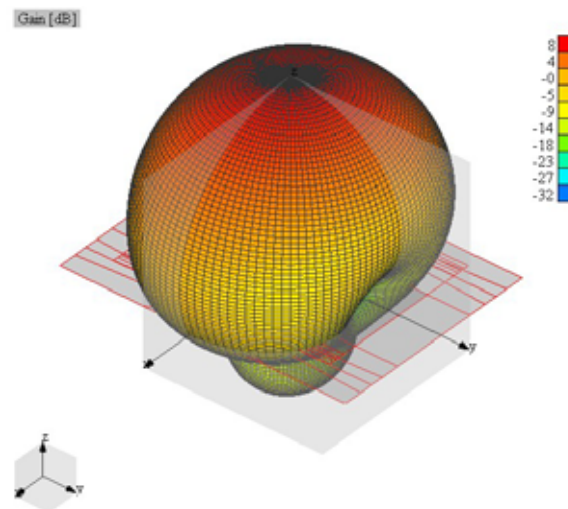


Figure 3.11 – 3D radiation pattern of the simulated antenna.

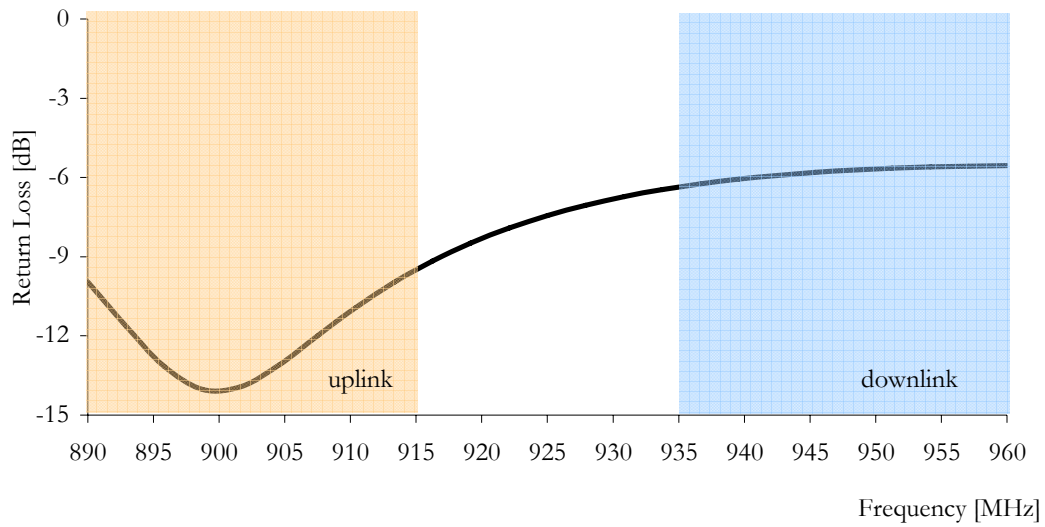


Figure 3.12 – Return Loss curve for the simulated model of the antenna.

Table 3.2 – Comparison between the simulated antenna and the real one.

	Manufacturer parameters	Simulation parameters
Impedance	50 $\Omega$	32.98 – j1.13 $\Omega$
VSWR	< 1.5	< 3.24
Gain	7 dBi	8.38 dBi
Horizontal HPBW	90°	85°
Vertical HPBW	65°	65°

One can state that although this model does not yield perfect results, it achieves an acceptable agreement with the manufacturer parameters. Further information on geometry details of the antenna (*e.g.*, details on the feeding point, details for impedance match) is required to improve the model, especially in terms of impedance results. Despite the slight discrepancies, the obtained antenna model is enough for at least a qualitative evaluation of the impact of scenario objects on the estimation of exclusion zones.



# **Chapter 4**

# **Estimation of Exclusion Zones**

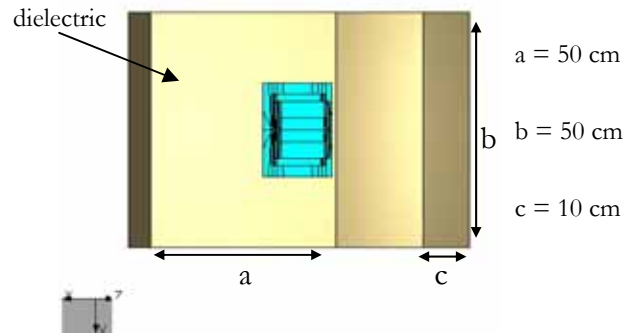
This chapter presents the methodology that was followed to estimate exclusion zones taking the nearby influence of the scenario of installation into account. Section 4.1 presents the five possible scenarios of BS installation considered and modelled in WIPL-D. The practical assessment of the simulation models through measurements is reported in Section 4.2. Section 4.3 analyses the results of simulations for the various scenarios, thus, leading to the practical method to estimate exclusion zones presented in Section 4.4.

## 4.1 Description of scenarios

By using the model of the Kathrein antenna described in Chapter 3, simulations were performed considering the antenna installed in five simulation scenarios. These scenarios represent possible cases of BS antennas installation both in indoor and outdoor environments. The physical dimensions of the used models are restricted by the allowed number of unknowns of WIPL-D, thus, being limited to a few wavelengths. The five created scenarios are represented from Figure 4.1 to Figure 4.5.



a) Real scenario

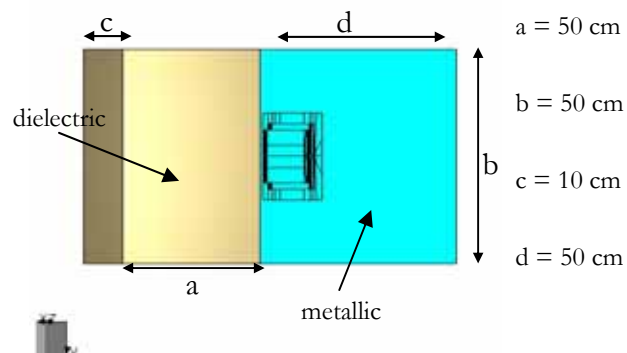


b) Corresponding simulated scenario

Figure 4.1 – “Dielectric Corner” (DiCo) scenario.



a) Real scenario

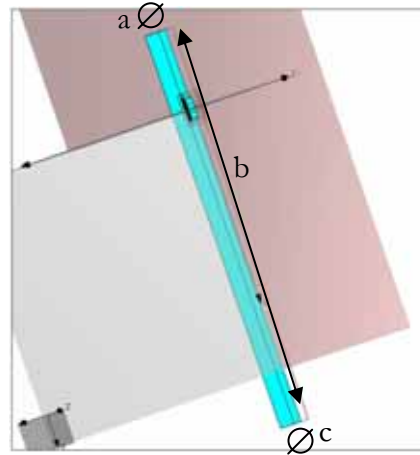


b) Corresponding simulated scenario

Figure 4.2 – “Metallic Corner” (MeCo) scenario.



a) Real scenario



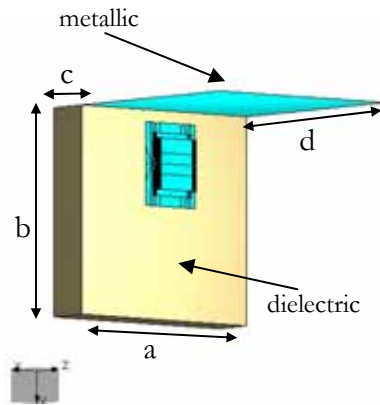
b) Corresponding simulated scenario

$$\begin{aligned} a &= 30 \text{ cm} \\ b &= 500 \text{ cm} \\ c &= 31.5 \text{ cm} \end{aligned}$$

Figure 4.3 – “Metallic Pole” (MePo) scenario.



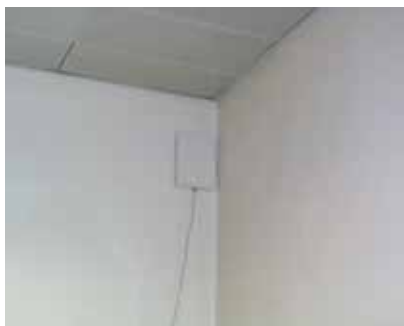
a) Real scenario



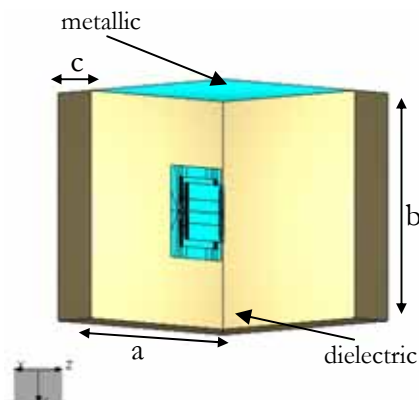
b) Corresponding simulated scenario

$$\begin{aligned} a &= 50 \text{ cm} \\ b &= 50 \text{ cm} \\ c &= 10 \text{ cm} \\ d &= 50 \text{ cm} \end{aligned}$$

Figure 4.4 – “Metallic Roof” (MeRo) scenario.



a) Real scenario



b) Corresponding simulated scenario

$$\begin{aligned} a &= 50 \text{ cm} \\ b &= 50 \text{ cm} \\ c &= 10 \text{ cm} \end{aligned}$$

Figure 4.5 – “Metallic Roof with Dielectric Corner” (MeRC) scenario.

In the previous figures, the blue parts represent metallic plates and the yellow ones represent dielectric materials. The metallic parts are modelled as perfect electric conductors, while the dielectric materials are assumed to be “Light Concrete”, which is a typical material of construction, with dielectric constant  $\epsilon = 2+j0.5$  and having 10 cm thickness, according to Table 4.1.

Table 4.1 – Material Properties (extracted from [DaCo99]).

Material	Uni-Karlsruhe		VTT		Typical thickness [cm]
	$\epsilon_r$	$\epsilon_i$	$\epsilon_r$	$\epsilon_i$	
Concrete	9	0.9	6	0.7	25
Light concrete	-	-	2	0.5	10
Brick	-	-	4	0.1	13
Plasterboard	6	0.6	2.5	0.1	2×1.3
Particle board	-	-	3	0.2	2×1.3
Wood	2.5	0.03	-	-	5
Glass	6	0.05	6	0.05	2×0.3
Bookshelf	2.5	0.3	-	-	30

For each of the five scenarios considered in this work, a study on the best approach to follow was done, so that a trade-off between the quality of the results and the number of problem unknowns (directly related to the simulations time) could be achieved. This study is reported in Annex C, and addresses three issues: accuracy of the parameters of the analysis, accuracy of the geometrical model, and use of symmetry properties of WIPL-D.

In what concerns the first topic, WIPL-D allows the user to change some of the parameters related with the degree of accuracy of the solution: the accuracy of the integrals used, the order of current approximation, and the frequency range of the analysis. Various simulation modes were



run for the five scenarios, by using different combinations of the above mentioned parameters, Table 4.2.

Table 4.2 - Simulations performed with different accuracies of parameters.

Simulation mode, $s$	Integral accuracy	Order of Currents	Frequency range, [MHz]
norm	Normal	Normal	902.5-960
1	Enhanced 1	Enhanced 1	902.5-960
2	Enhanced 2	Enhanced 2	902.5-960
3	Enhanced 3	Enhanced 3	902.5-960
4	Enhanced 1	Enhanced 1	902.5-1050

It is concluded that the simulation mode that is necessary to obtain satisfactory results depends on the type of scenario, the following choices being taken:

- For the DiCo scenario, the simulation mode should be  $s = \text{norm}$ .
- For the MeCo scenario, the simulation mode should be  $s = 2$ .
- For the MePo scenario, the simulation mode should be  $s = 1$ .
- For the MeRo scenario, the simulation mode should be  $s = 2$ .
- For the MeRC scenario, the simulation mode should be  $s = \text{norm}$ .

In what concerns the accuracy of the geometrical model description, one intended to analyse how simple a geometrical model could be and still provide acceptable results. Two scenarios were analysed, the MePo scenario, which is wholly composed of metallic parts, and the MeRo one which contains both metallic and dielectric elements.

For the MePo scenario, different geometrical models were considered, varying the height and the top and bottom radius of the lamp post, and varying also the relative position of the antenna in the pole. It is concluded that the increase of the pole's height originates minor differences on the

horizontal pattern, while producing higher differences in the vertical one. As the number of problem unknowns is not critical in this case, it was decided to take a more realistic approach and choose a light pole with the dimensions referred in Figure 4.3.

For the MeRo scenario, it is observed that increasing the physical dimensions of the model is prohibitive in terms of the number of unknowns and, similarly to the metallic case, it has a minor influence on the horizontal pattern and a higher influence and dispersion of values on the vertical one. Therefore, for the dielectric case, the geometrical model was taken as small as possible, keeping in mind the differences in the vertical pattern.

WIPL-D can speed up the analysis for scenarios having both geometry and excitation symmetrical with respect to principal coordinate planes. As only half of the structure is defined, a reduction is achieved in the number of simulation unknowns and of CPU time used (approximately halved compared with the analysis of the original problem), meaning that the maximum electrical size that WIPL-D can handle is doubled. In MePo and MeRo scenarios, both the geometry and the excitation are symmetrical to the  $yOz$  plane, so again the symmetry options of WIPL-D were used.

As the definition of the reduced symmetrical model is different in practice from the original full model, some differences are found for both scenarios. For the MePo scenario, a maximum average difference of 0.06 dB is found between the radiation pattern of the original problem and the symmetric one, along with a reasonable reduction in the number of unknowns required for simulation of the symmetry model. Thus, it is concluded that the symmetry options could be used in simulations of the MePo scenario, without any loss of accuracy of the results. For the MeRo scenario, a slight reduction on simulation time (average reduction of 16%) and a considerable reduction in the number of unknowns are achieved when using symmetry. However, for  $s = 2$ , the mode that was decided to use for this scenario in the analysis of simulation parameters, reasonable differences are found in the radiation pattern, thus, symmetry properties are not used in the MeRo scenario.

It is important to mention that the time of simulation for each scenario depends on a lot of variables, such as the number of unknowns involved, the type of analysis requested (radiation pattern evaluation, near-field calculation), the number of observation points, the number of frequencies being analysed and so on. One may have simulation times from tens of second to up to tens of minutes per scenario.

## 4.2 Comparison between measurements and simulations

As stated above, due to the restriction in the number of unknowns that are available in the used WIPL-D license, the models used for each scenario are very simple and do not represent a real situation, where several objects are present and sometimes dynamically changing their position through time. In order to assess the reliability of simulation results, measurements were performed considering three of the previously simulated cases: isolated antenna, MeRo and MeRC scenarios.

Regarding the isolated antenna, the objective was to measure horizontal and vertical radiation patterns of the antenna in an anechoic chamber. The used chamber has a fully automatic measurement system [LoCa93] controlled from a central location, and composed of four subsystems: positioning and control, receiving, signal source, and recording and processing.

According to the measurement set-up represented in Figure 4.6, a log-periodic antenna working in the 900 MHz frequency range was installed on one side of the camera, Figure 4.7b, working as probe antenna. On the other side of the camera, the Kathrein antenna was installed on a positioner, Figure 4.7a, in the transmitting mode. According to a pre-defined measurement sequence, the *E*-plane and *H*-plane have been measured. Figure 4.8 and Figure 4.9 present the graphical comparison between measurement results and WIPL-D predictions, where zero degrees correspond to the bore sight direction of the antenna.

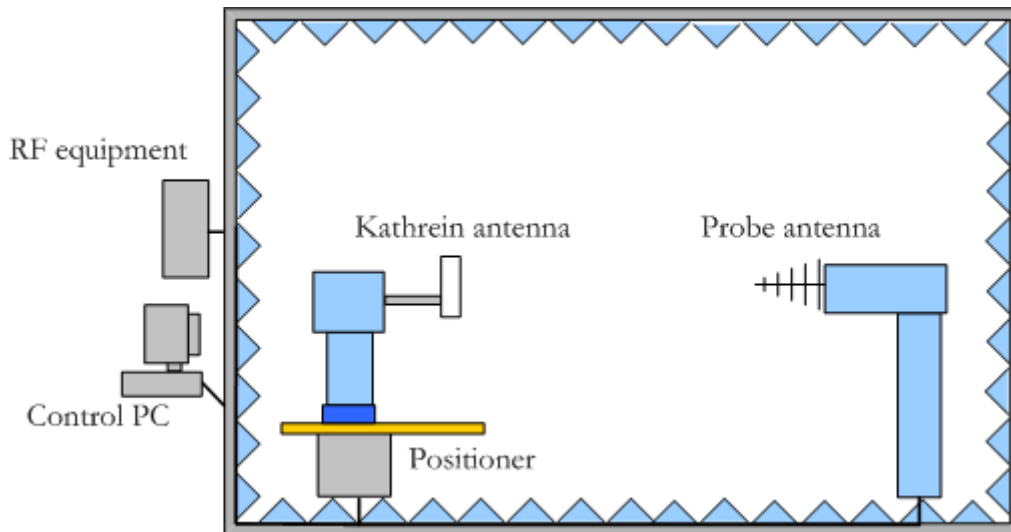
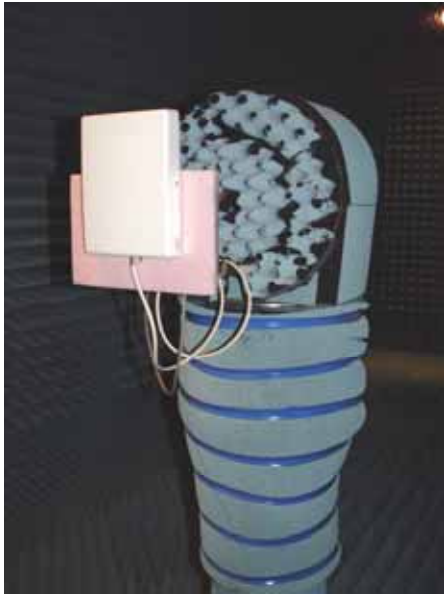
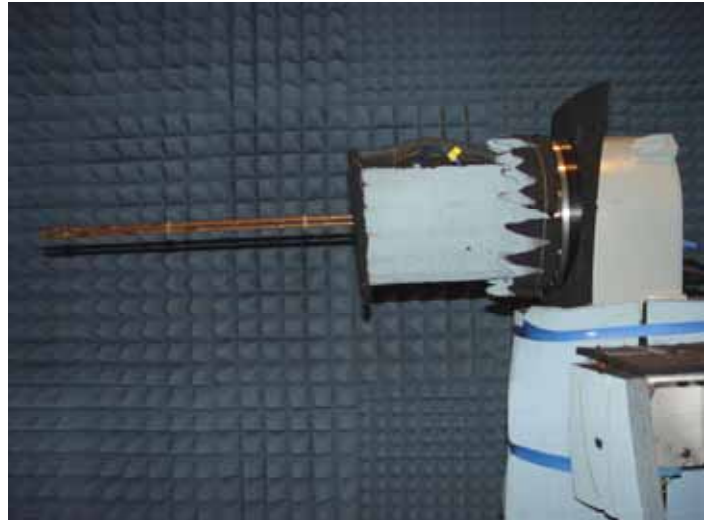


Figure 4.6 – Sketch of the measurement set-up (isolated antenna).

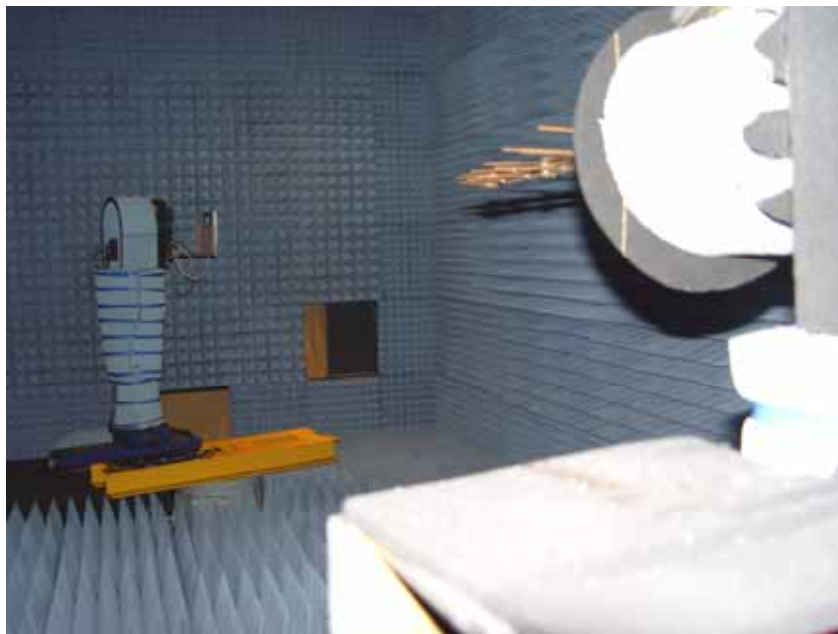
A good agreement between the measured and the simulated results is found, both for the  $E$ - and  $H$ -planes, although some discrepancies are found on the antenna's backside ( $|\text{angles}| > 90^\circ$ ), which are clearly due to interference on measurements caused by the structure that supports the antenna under test. Poor absorbing characteristics of the wall material at 900 MHz may have also affected the measurement results.



a) Kathrein 736 624



b) Log periodic antenna (probe antenna)



c) Measurement set-up

Figure 4.7 – Measurements of the isolated antenna at the anechoic chamber.

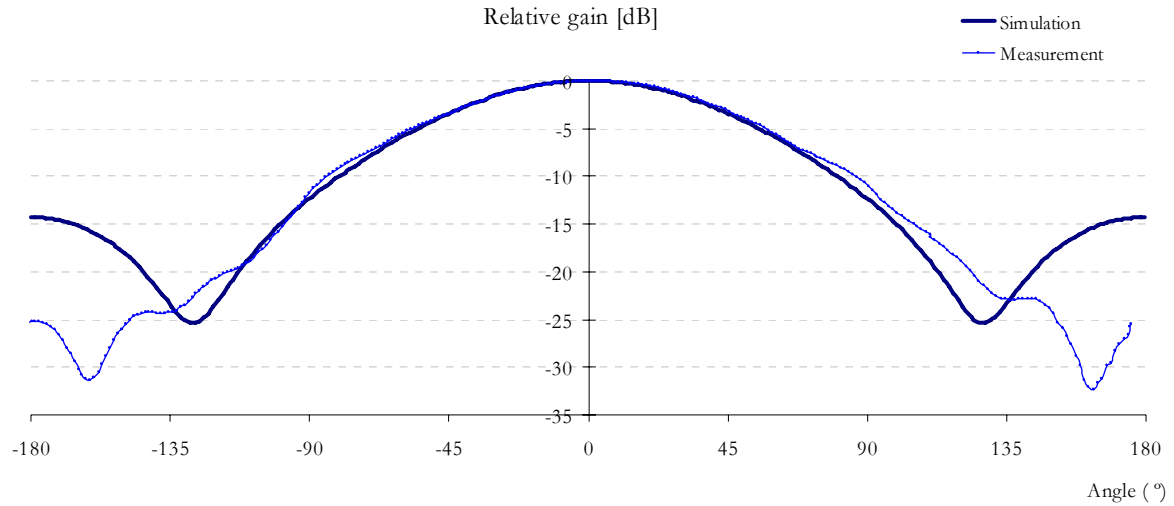


Figure 4.8 – Horizontal radiation pattern.

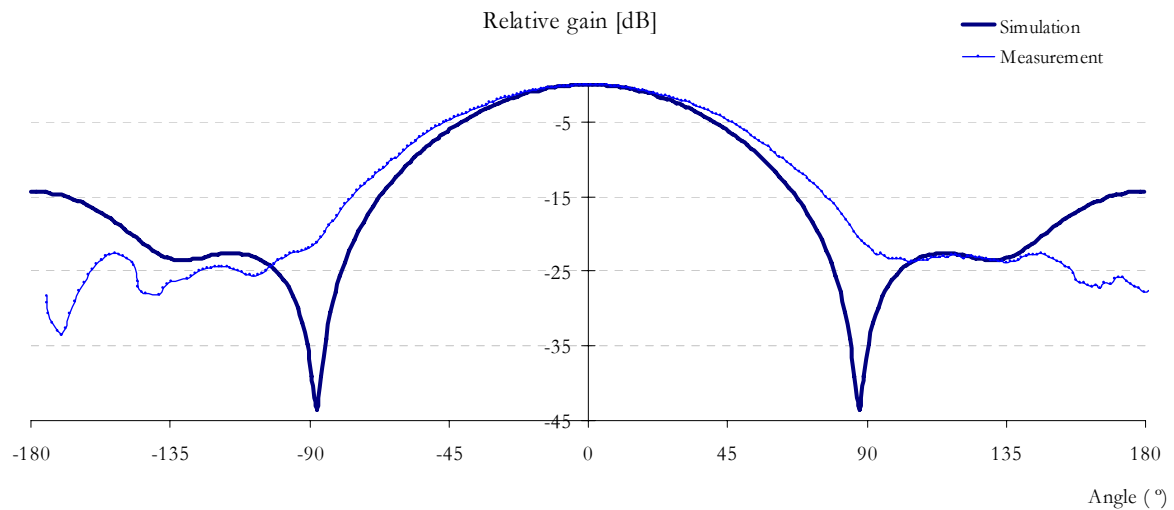


Figure 4.9 – Vertical radiation pattern.

Recreation of MeRo and MeRC scenarios was not performed inside the anechoic chamber, as it would be impractical to sustain samples of walls with large dimensions inside the camera. Thus, measurements were performed in a real classroom, with the configurations represented in Figure 4.10 and Figure 4.11. With these configurations, only a horizontal plane that passes by the centre of the test antenna has been measured. The antenna under test was connected to an RF generator, transmitting at 902.5 MHz. Measurements were performed with Narda SRM-3000 spectrum analyzer [NARD06], connected to a 900 MHz single axis antenna. Figure 4.12 and Figure 4.13 present the graphical comparison between the results of measurements and the

WIPL-D predictions for MeRo and MeRC scenarios, respectively.

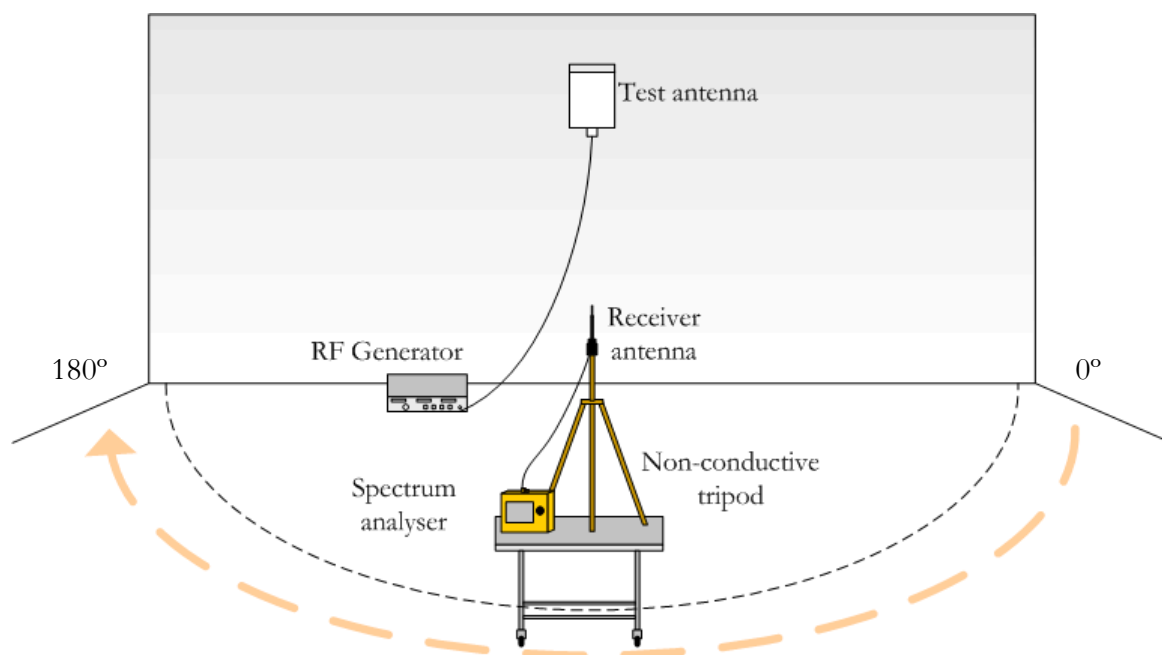


Figure 4.10 – Sketch of the measurement set-up (MeRo scenario).

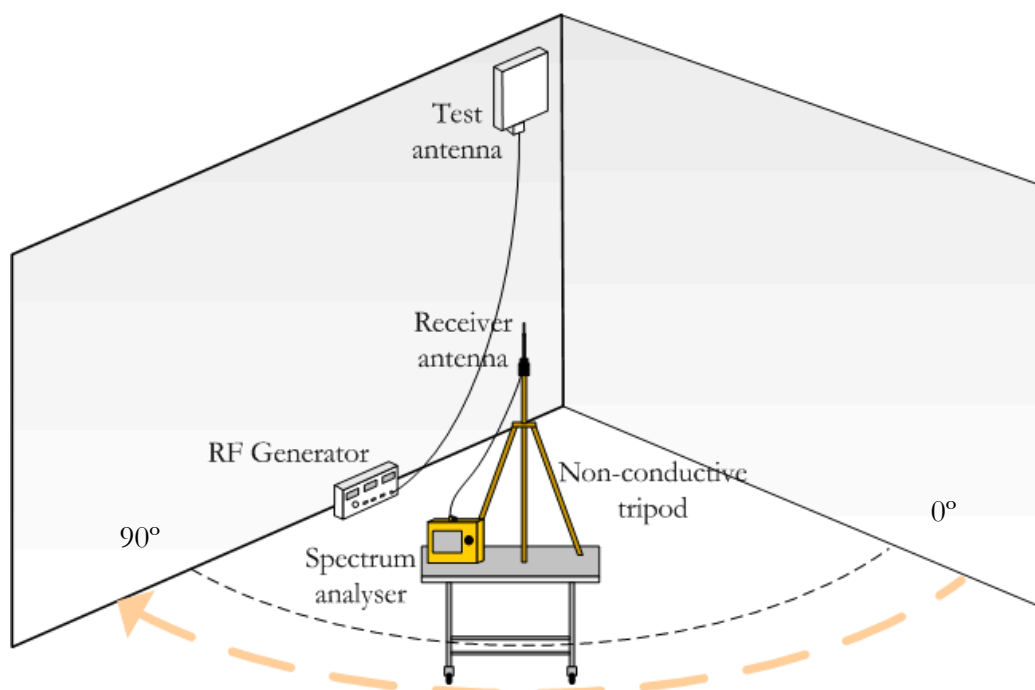


Figure 4.11 – Sketch of the measurement set-up (MeRC scenario).

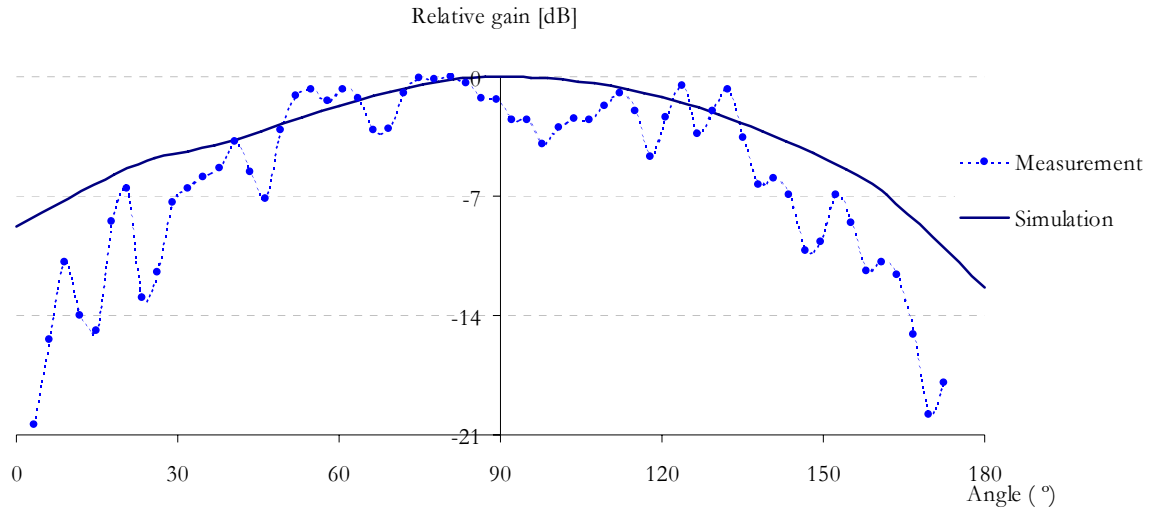


Figure 4.12 – Comparison of results for the MeRo scenario.

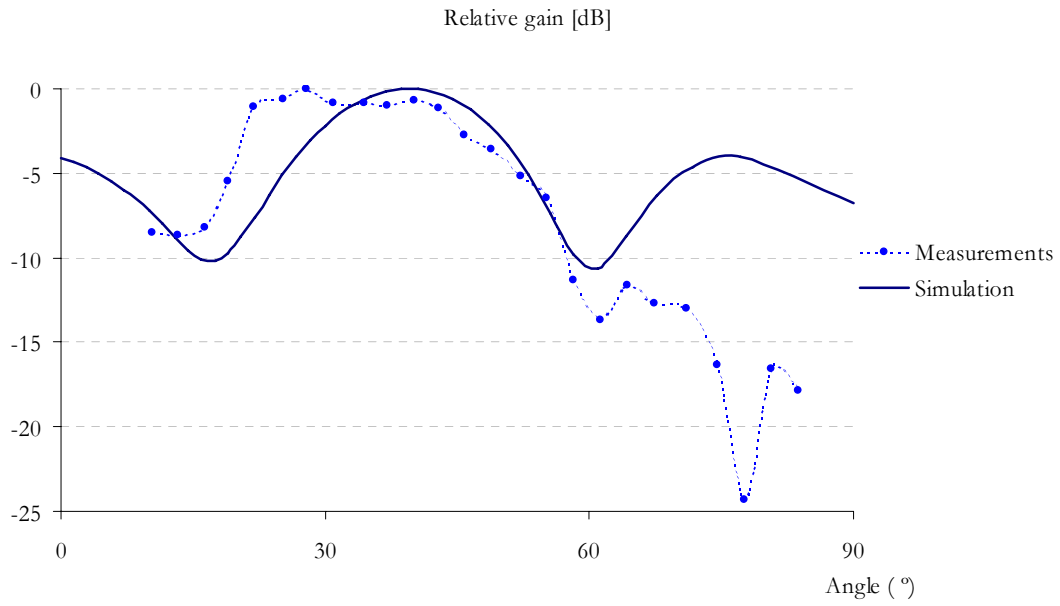


Figure 4.13 – Comparison of results for the MeRC scenario.

For the MeRo scenario, a good agreement is found between measurement results and WIPL-D predictions. Fluctuations in measurement results are due to reflections resulting from more complex details of the real environment, which could not be accounted in simulations, like the structure of the walls. For the MeRC scenario, a similar corner effect caused by the walls is found for both measurement and simulation results. Again there are some differences between simulations and measurements for angles  $> 45^\circ$ , which evidence the limitations of the geometrical model used in WIPL-D.

It is important to state that measurements were influenced by various factors, such as the nearby influence of a metallic board and of a set of tables and chairs that were located inside the measurement room.

Besides the factors stated above, the discrepancies between WIPL-D predictions and measurements are directly related to the limited dimensions of the geometric models adopted, as well as to the dielectric properties of the walls considered in simulations, which are different from those of the real walls.

The main conclusion from the comparison between measurement and simulation results is that the adopted geometrical models are a good approach to reproduce real scenarios. The reduced geometrical dimensions of WIPL-D models still lead to accurate results, do not restricting the overall evaluation.

### **4.3 Comparison of scenarios**

The comparison of results obtained for the different scenarios presented in this section is twofold, comprising the analysis of both impedance and radiation pattern. On the one hand, the analysis of impedance mismatch in the various scenarios is important in order to understand how the effective transmitted power differs from the ideal case of the isolated antenna. On the other, the study of the radiation pattern has a direct impact on the geometrical definition of the exclusion zone.

Table 4.3 presents the input impedances obtained for the various scenarios for  $f = 902.5$  MHz. As it is important to analyse antenna's behaviour for the entire bandwidth, RL curves were studied on the overall bandwidth for the various scenarios. Figure 4.14 presents the graphical representation of these curves for the various scenarios under study.

The general conclusion is that when an antenna is placed in a typical installation scenario, the input impedance mismatch will modify. This leads to increased reflection loss and consequently to implicit increase of input powers. The analysis of RL curves emphasises that impedance-matching conditions are clearly modified, decreasing down to 4 dB. Moreover, by analysing each particular result, one may observe that:



- When an antenna is installed on a dielectric corner (DiCo scenario), impedance slightly differs from its free space value. When comparing the RL curve for this situation with the one from the isolated antenna, one may observe that matched impedance is obtained for lower frequencies and that RL values decrease down to 4 dB, thus decreasing system's performance. Similar conclusions also apply to the situation of installation on a dielectric corner, with a metallic ceiling (MeRC scenario).
- When an antenna is installed on a metallic surface like in the MeCo scenario, its impedance modifies considerably. The analysis of RL curve shows that this situation leads to severe antenna's inefficiency. For this scenario, a  $RL < -1.79$  dB ( $VSWR < 9.75$ ) is obtained, while a RL value below  $-5.55$  dB ( $VSWR < 3.24$ ) is obtained for the isolated antenna.
- The installation of an antenna on a metallic pole (MePo scenario) decreases antenna's impedance, leading to an approximately constant RL curve and thus to poorer efficiency.
- Installing an antenna on a dielectric wall with a metallic ceiling above (MeRo scenario) has a minor effect on its input impedance. The RL curve for this situation shows a similar behaviour within the frequency band as isolated antenna.

Table 4.3 – Input impedance for the various scenarios ( $f = 902.5$  MHz).

Scenario	Input impedance [ $\Omega$ ]
Isolated antenna	$32.98 - j 1.13$
DiCo	$26.69 - j14.27$
MeCo	$9.77 - j0.42$
MePo	$22.03 - j14.37$
MeRo	$27.67 - j2.26$
MeRC	$25.91 - j13.17$

3D radiation patterns were obtained for the antenna located in the five simulation scenarios (see

Annex D for further information on radiation patterns for each scenario). The overall conclusion resulting from the analysis of the radiation patterns is that the installation scenario has a great influence on the way antenna radiates in space, almost always leading to the deformation of antenna's free space radiation pattern. The following specific results are found:

- The situation of installation on a dielectric corner (DiCo scenario) leads to evident distortions on the radiation diagram, Figure 4.15. A “corner” effect probably formed by propagation modes occurring inside dielectric walls is verified, as well as the introduction of secondary radiation lobes. These conclusions also apply when the antenna is located on a dielectric corner with a metallic roof (MeRC scenario).
- The MeCo scenario presents a great dissimilarity when compared to the isolated antenna, Figure 4.16. When a metallic structure is located behind the antenna, a considerable increase of its directivity properties is found.
- For installation on metallic poles (MePo scenario), the most visible effect is the attenuation of backward radiation lobe, Figure 4.17. A reduction of vertical and horizontal HPBW's is also observed, thus, leading to an increased antenna's directivity.
- The situation of an antenna installed on a dielectric wall, with a metallic roof above it (MeRo scenario) approaches the radiation pattern of the isolated antenna, although with slight distortions on the vertical plane.

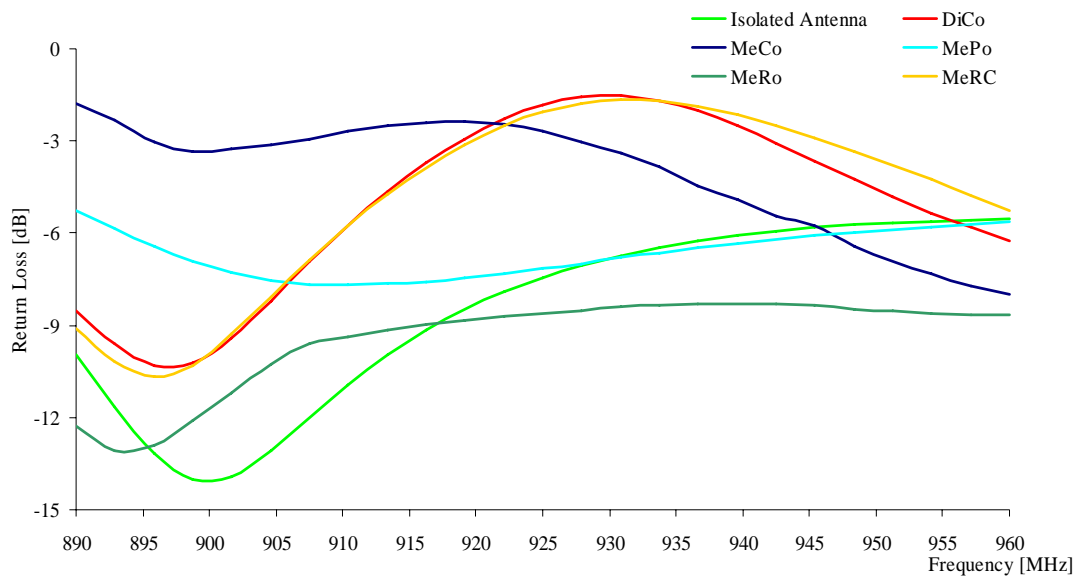


Figure 4.14 – RL curves for the various scenarios.

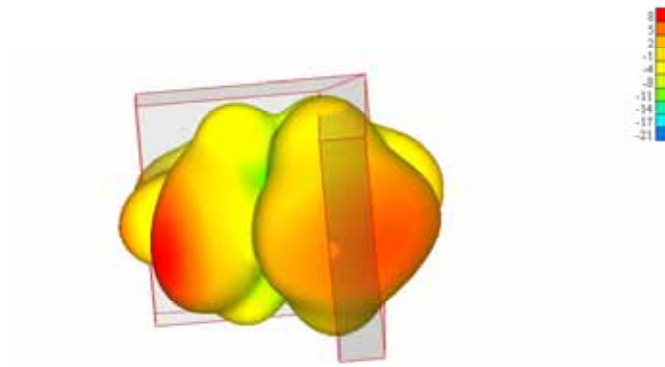


Figure 4.15 – 3D radiation pattern obtained for the DiCo scenario.

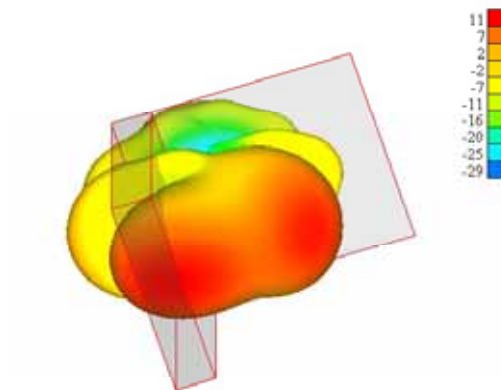


Figure 4.16 – 3D radiation pattern obtained for the MeCo scenario.

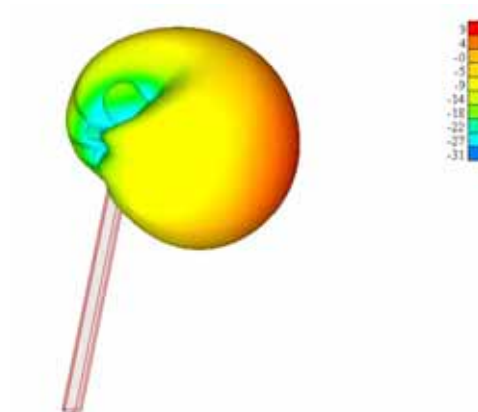


Figure 4.17 – 3D radiation pattern obtained for the MePo scenario.

## 4.4 Exclusion zones calculation

WIPL-D allows the calculation of near-field values for an area of interest defined by the user, Figure 4.18, also enabling to create ASCII files with near-field results. Hence, based on the outputs extracted from WIPL-D simulations, a small application was developed in Matlab [MATL06] in order to allow fast processing and extended graphical manipulation of results. The developed Matlab application receives WIPL-D output files with near-field values, then, through comparison with EMF reference levels for the frequency of operation,  $f = 902.5$  MHz, it traces the 2D compliance boundary. Finally, the exclusion radius,  $r_{comp}$ , for the plane of interest is calculated.

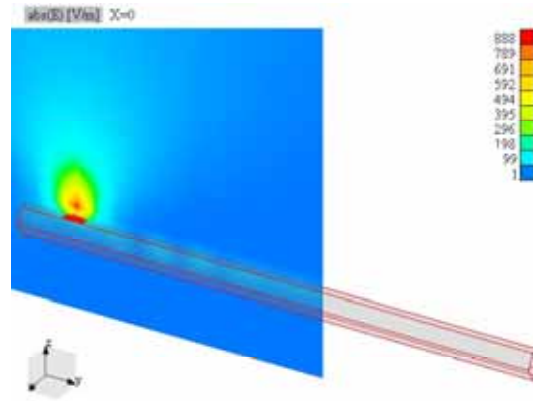


Figure 4.18 – Example of near field calculation using WIPL-D (MePo scenario).

For all scenarios, the near-field values are predicted on both horizontal and vertical planes passing through antenna's origin. The red region in Figure 4.19 indicates the horizontal plane ( $y=0$ ), while the blue region corresponds to the vertical one ( $x=0$ ). For each plane, the exclusion radius,  $r_{comp}$  is estimated.

According to (2.1), the far-field region of the Kathrein antenna under study occurs at distances  $d > 0.24$  m from the antenna. The field values were predicted for different input powers, ranging from 100 mW to 50 W, in order to understand how the exclusion zone will modify according to the power feeding the antenna, thus, one has exclusion zones lying inside the near-field region and others falling in the far-field one. The application developed in Matlab determines two compliance boundaries, one for compliance with  $E$ -field reference levels and another one for compliance with  $H$ -field reference levels. In the far-field, these two boundaries overlap, while in the near-field, the compliance boundary is assumed to be the largest of the  $E$ - or  $H$ -field

boundaries. Figure 4.20 presents an example of the latter situation, where the closed red curve indicates the  $E$ -field compliance boundary and the green one points out the  $H$ -field compliance boundary. In this situation, the chosen compliance boundary is the green one and the exclusion radius,  $r_{sno}$ , is estimated as being the maximum distance from the centre of the antenna to this curve, as indicated in the same figure.

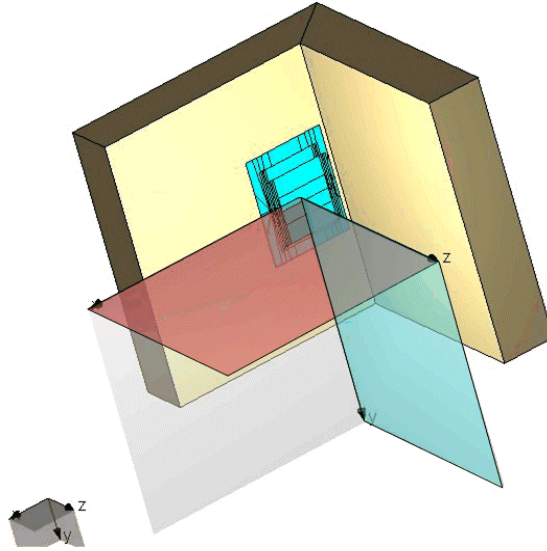


Figure 4.19 – Definition of horizontal and vertical planes.

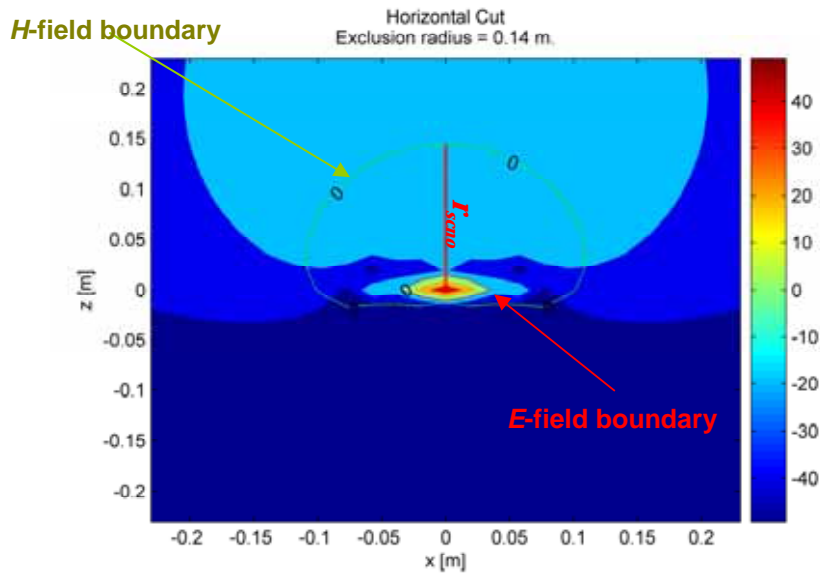


Figure 4.20 – Estimation of compliance boundary in the near-field ( $P_{in} = 200$  mW).

Figure 4.21 presents the exclusion boundary for the isolated antenna on the horizontal and vertical planes, when it is fed with  $P_{in} = 50$  W. In this case,  $r_{sno} = 2.5$  m for both planes, as

expected. From Figure 4.22 to Figure 4.26 one may observe horizontal and vertical compliance boundaries and  $r_{sco}$  for the five scenarios under study, corresponding to  $P_{in} = 50$  W. By analysing the obtained results, one can see that the geometrical shape of the exclusion boundary is distorted and extended for all scenarios.

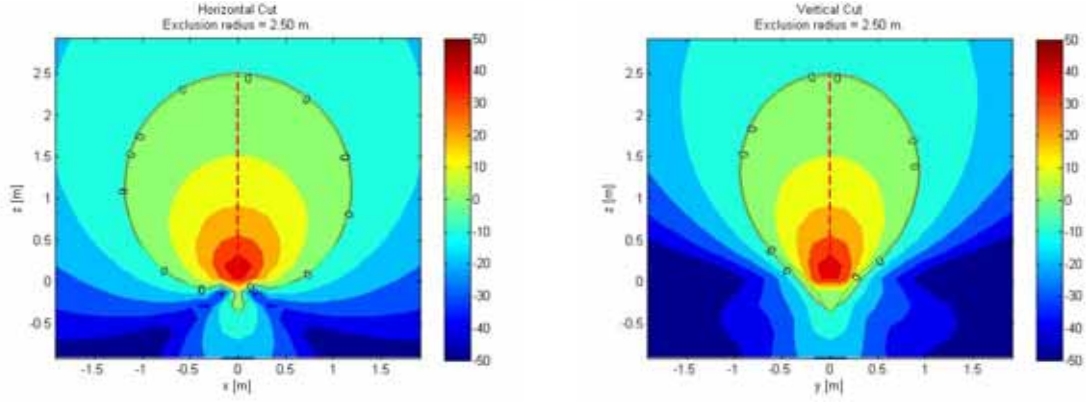


Figure 4.21 – Estimation of exclusion zone for the isolated antenna ( $P_{in} = 50$  W).

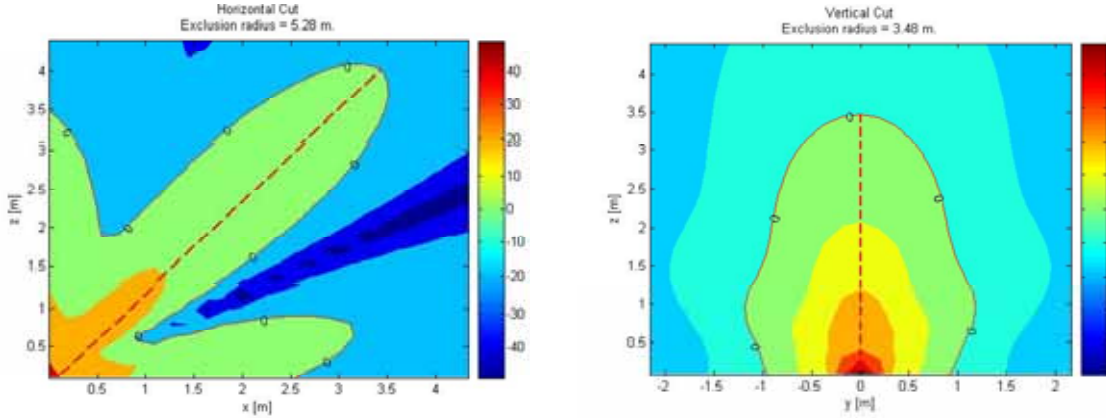


Figure 4.22 – Estimation of exclusion zone for the DiCo scenario ( $P_{in} = 50$  W).

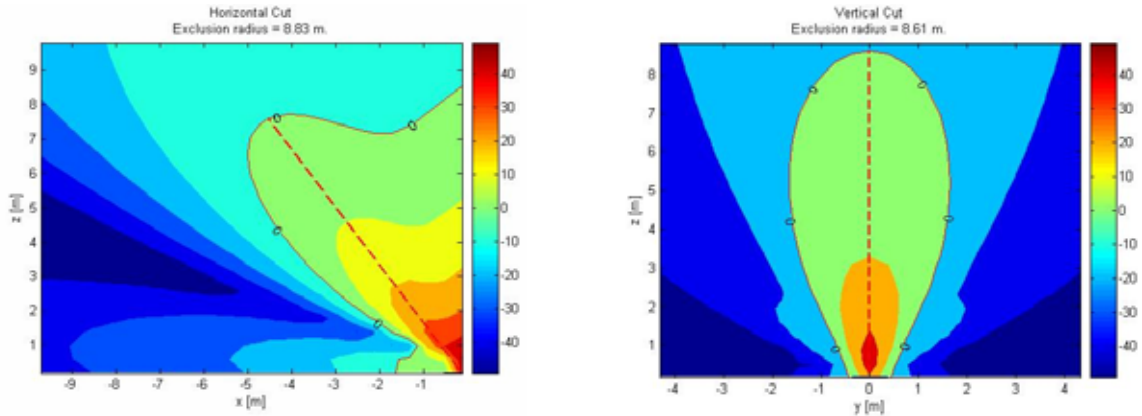
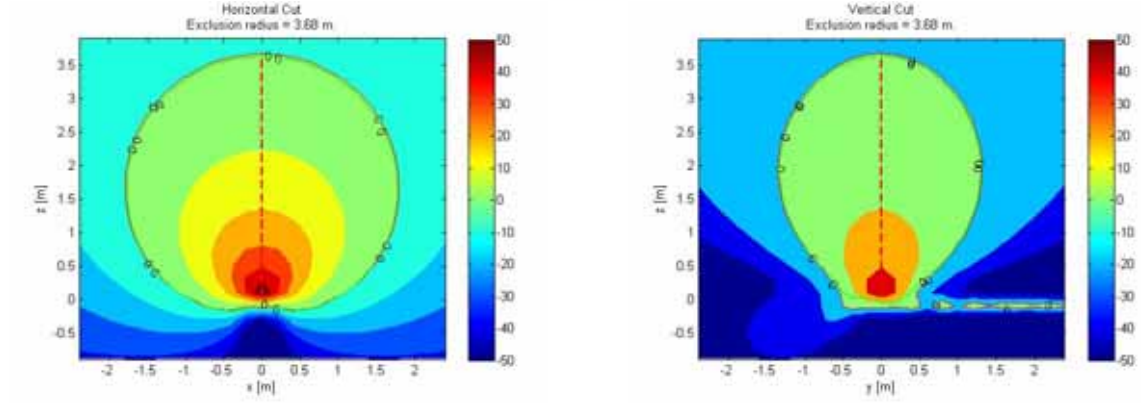
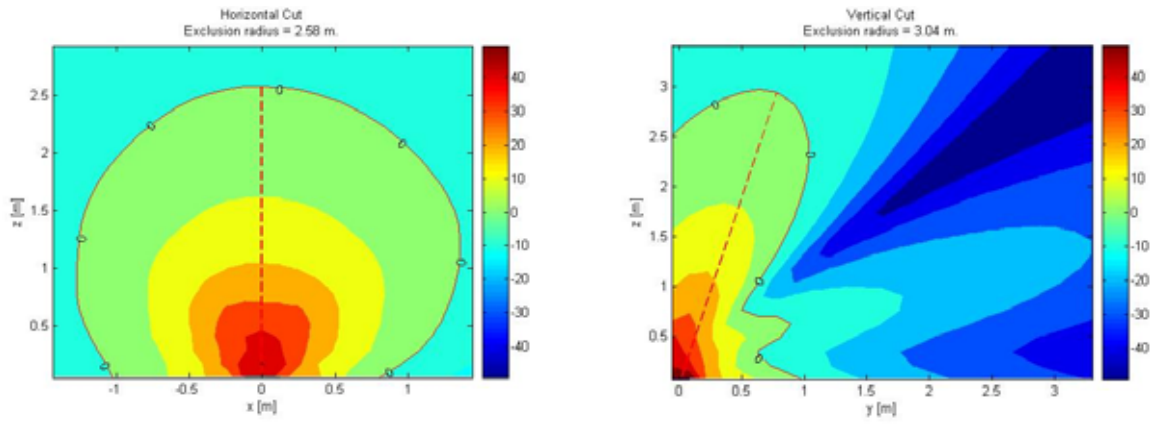
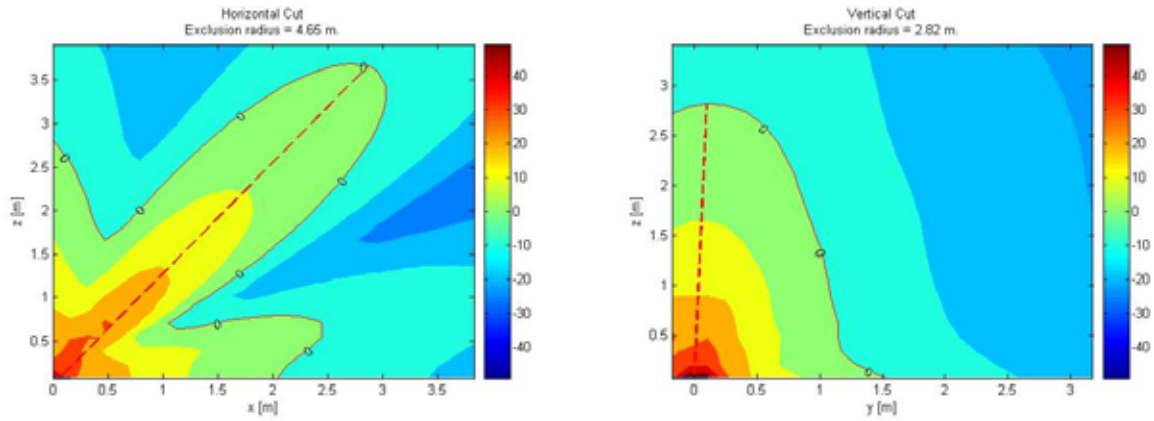


Figure 4.23 – Estimation of exclusion zone for the MeCo scenario ( $P_{in} = 50$  W).


 Figure 4.24 – Estimation of exclusion zone for the MePo scenario ( $P_{in} = 50$  W).

 Figure 4.25 – Estimation of exclusion zone for the MeRo scenario ( $P_{in} = 50$  W).

 Figure 4.26 – Estimation of exclusion zone for the MeRC scenario ( $P_{in} = 50$  W).

In order to understand how the exclusion radius modifies when a more accurate (*i.e.*, larger) geometrical model is used, a modified version of the MeRo scenario with extended walls was created and simulated. In this model, the height of walls has been increased from 0.5 m to 1 m



and the width was increased from 0.5 m to 1.5 m. It is observed that the number of simulation unknowns with such parameters increases about 4.4 times compared with the original model, and also that the simulation time increases about 12 times. Comparing the results for horizontal and vertical planes, Figure 4.27 and Figure 4.28 respectively, one may observe that the exclusion area obtained with the extended model maintains almost the same shape, although it becomes more restrictive for a factor of about 1.24. Thus, considering the huge increase of simulation time for the extended model, one has decided to use the original model, however, having in mind its limitations. The same increase on the number of unknowns and on the simulation time is expected for extended models for the other scenarios, so all have been kept with the original dimensions.

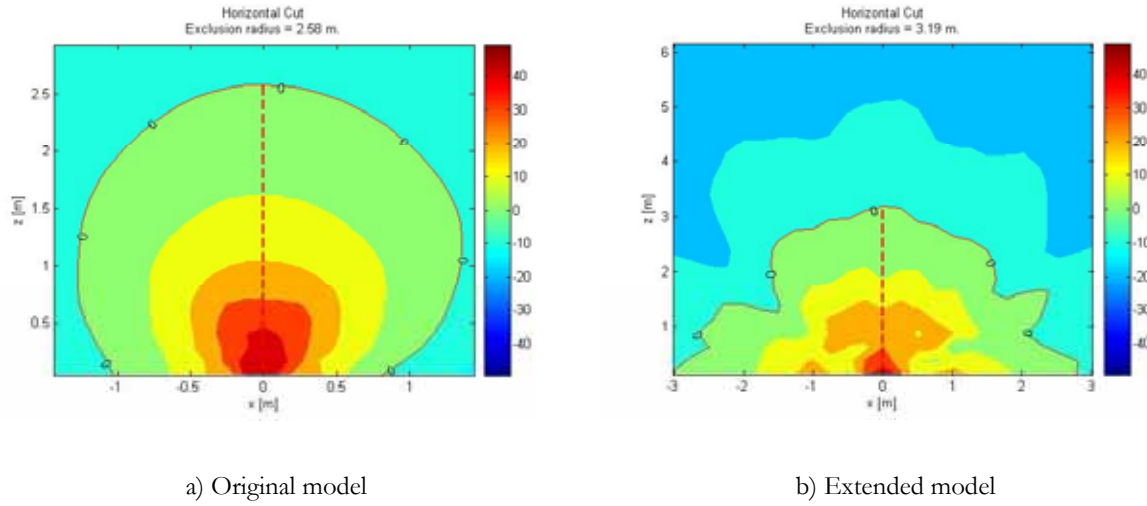


Figure 4.27 – Exclusion radius for original and extended models of the MeRo scenario (horizontal plane).

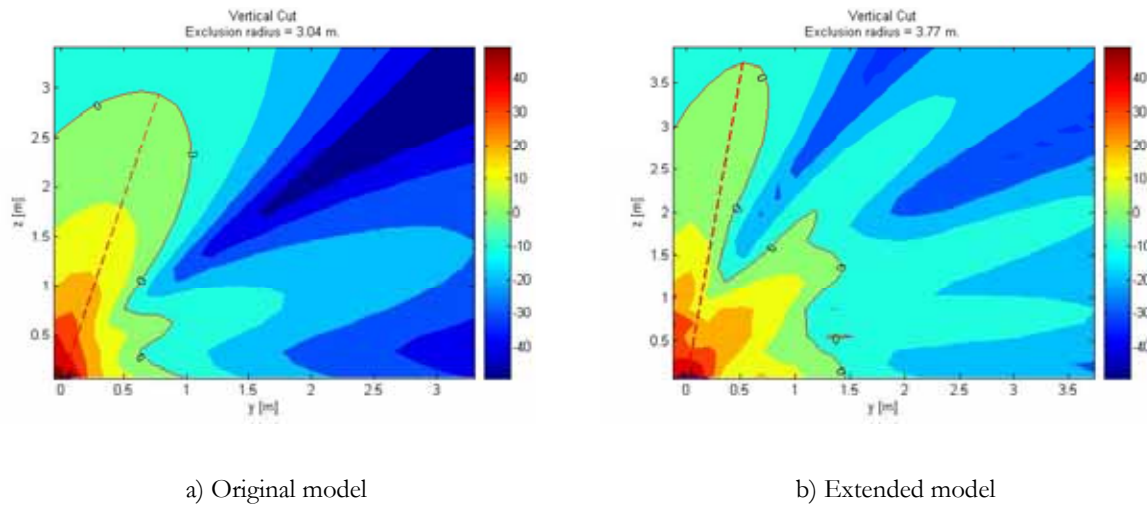


Figure 4.28 – Exclusion radius for original and extended models of the MeRo scenario (vertical plane).



Concerning the limitations of the used geometrical models, this work does not intend to obtain deterministic values for the extension and shape of exclusion zones for wireless antennas. Instead, it intends to provide qualitative tendency of the results and some guidelines to wireless operators when dimensioning and installing new antennas.

The final outcome of the work is presented in Figure 4.29 and Figure 4.30, where one can observe, for all scenarios, how the ratio  $r_{scno}/r_{ant}$  depends on different typical input powers,  $r_{ant}$  being the exclusion radius estimated for the antenna in free space conditions. The main conclusion from the results found on the shape and on the extension of exclusion zones stresses the importance of not uncritically applying free space conditions in wireless networks planning tools.

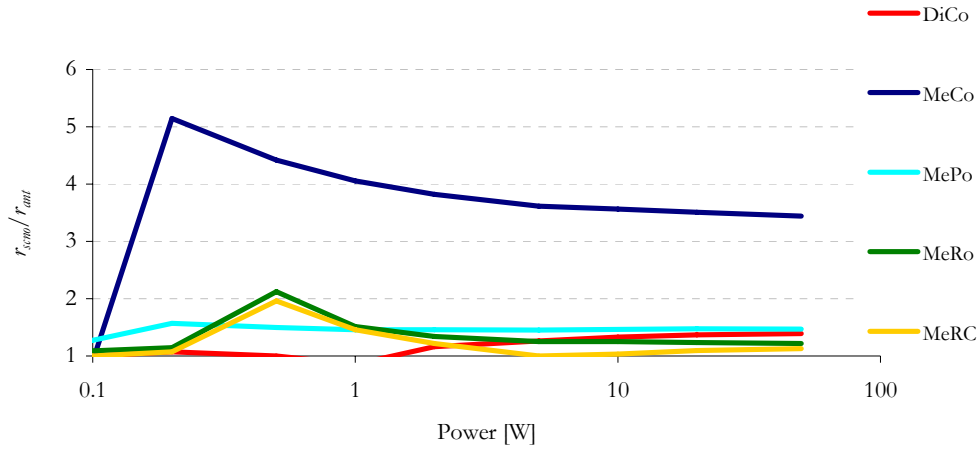


Figure 4.29 – Representation of  $r_{scno}/r_{ant}$  (vertical plane) for the various scenarios.

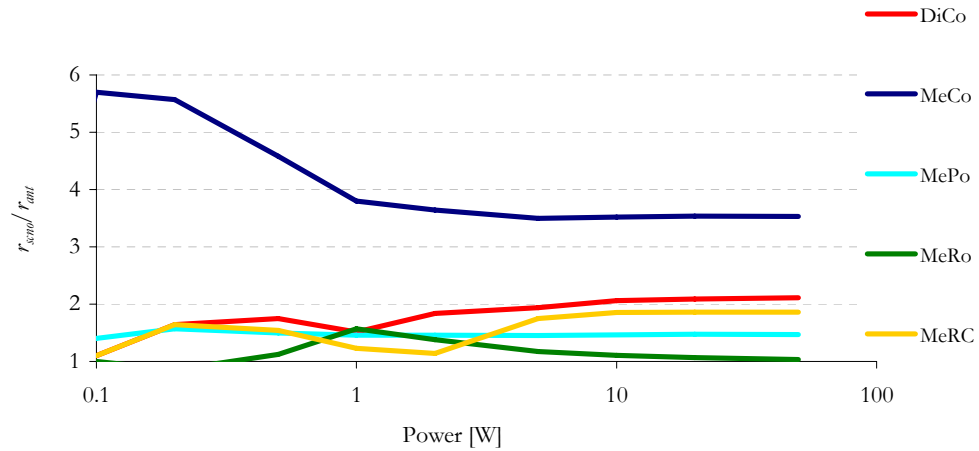


Figure 4.30 – Representation of  $r_{scno}/r_{ant}$  (horizontal plane) for the various scenarios.

A general conclusion is that for all scenarios and for both vertical and horizontal planes, it can be stated that, above a certain input power – generally, the power associated to the compliance boundary corresponding to the near-field limit – the ratio  $r_{sco}/r_{ant}$  remains almost constant. Regarding each particular scenario, some conclusions may be drawn:

- The DiCo scenario presents strictest results in the horizontal plane rather than in the vertical one. This is caused by the presence of the dielectric corner, which acts as a reflector, increasing antenna's directivity. In this case, the exclusion zone may extend up to 2 times the one calculated in free space conditions.
- The MeCo scenario presents the most restrictive results, with  $r_{sco}$  reaching up to 5.7 times the exclusion radius calculated in free space conditions. For  $P_{in} > 1$  W, results are quite similar for both horizontal and vertical planes.
- The MePo scenario shows similar results for the horizontal and vertical planes, with the exclusion zone being about 1.3 times the one calculated in free space conditions.
- The influence of a metallic roof above an antenna has no expression in the horizontal plane, impacting essentially on the vertical one. For the MeRo scenario, the exclusion radius in the horizontal plane is almost equal to the one obtained for the isolated antenna, while in the vertical plane it doubles the one obtained in free space.
- Results for the MeRC scenario show a joint influence from the dielectric corner and the metallic ceiling. The dielectric corner has a major impact, extending the horizontal exclusion up to 1.9 times the one obtained in free space.

Adopting a worst-case perspective, it is concluded that, for common BS installation scenarios, the exclusion radius might be estimated as being twice the one obtained under free space conditions. Exception is made for corner configurations with a metallic part on the back of the antenna, where the exclusion radius may increase by a factor of 5.

In future work, accurate approaches might be used, such as a combination of numerical simulation tools with ray-tracing techniques. This will lead to refined exclusion zones, but not to a practical approach, due to the complexity, the multiplicity and the dynamic of variables present in each environment. Furthermore, it is important to state that it is almost impossible to model reality.

Although all the work has been developed for a GSM900 antenna, the main conclusions are valid for the other wireless technologies mentioned in this thesis. In these frequency bands (900 MHz, 1800 MHz, 2 GHz, 2.5 GHz, 3.5 GHz, 5 GHz), no differences in the EMFs behaviour are expected to occur, as the results are scalable with respect to the involved wavelengths.



# **Chapter 5**

# **Conclusions**

This chapter finalises the thesis, summarising conclusions and pointing out aspects that may be developed in future works.

In order to protect the public from potential harmful levels of radiation, exclusion areas around antennas from wireless communication systems are defined. These areas, within which EMFs reference levels are exceeded, are generally defined by considering the antennas in free space conditions. This work aims at developing a method for the estimation of exclusion zones taking the actual surrounding environment into account. A possible approach to the evaluation of compliance boundaries for BS antennas, considering common indoor and outdoor installation scenarios is presented. Moreover, the work analyses the influence of both metallic and dielectric 3D structures surrounding BS antennas.

As a first step, basic aspects of EMFs propagation and antennas are studied, with the aim of identifying important parameters for the estimation of exclusion zones. Relevant characteristics of the radio interface of wireless technologies are then identified. A study on the current reference levels and on main guidelines established by international bodies for assessment of EMF levels is also carried out.

A discussion on different approaches to the assessment of EMF levels is presented: starting with the theory to estimate exclusion zones, then going through the calculation of fields in the near-field region, and ending with the estimation of field levels in the presence of scattering objects and others. No studies were found on the literature considering estimation of exclusion zones for BS installation in real scenarios.

In this thesis, the problem of evaluating EMFs in any point of interest around an antenna is solved through an Integral Equation and the MoM, by using the commercial numerical EM code WIPL-D. This code allows to model general 3D structures, like antennas and scatterers, characterising them with equivalent surface electric currents over metallic portions and over dielectric material surfaces.

Because of logistics availability, the 736 624 Kathrein indoor directional antenna, operating in the GSM900 band, was chosen as an example of a real antenna to be studied. A geometrical model for this antenna was developed in WIPL-D, based on detailed technical data provided by Kathrein. The performance of the developed model is assessed in terms of impedance and radiation pattern analysis, being concluded that it allows at least a qualitative evaluation of the impact of scenario objects on the estimation of exclusion zones.

Geometrical models for five common indoor and outdoor BS installation scenarios were then

created and the antenna model was placed on each one. These scenarios represent dielectric wall corners with and without metallic ceilings (MeRC and DiCo scenarios, respectively), a light pole (MePo), a dielectric wall installation with a metallic ceiling (MeRo) and also the case of a metallic box close to a dielectric wall (MeCo). Metallic structures are modelled as perfect electric conductors, while dielectric walls are assumed to be made of “Light Concrete” material. For each scenario, a study addressing the accuracy of the parameters of the analysis, the accuracy of the geometrical model, and use of symmetry properties of WIPL-D was done, so that a trade-off between the quality of the results and the number of problem unknowns (directly related to the simulations time) could be achieved. It is important to mention that simulation time directly depends on the number of problem unknowns, on the type of analysis requested (radiation pattern evaluation, near-field calculation), on the number of observation points, on the number of frequencies being analysed and so on. One may have simulation times from tens of second to up to tens of minutes per scenario.

Physical dimensions of the created models are restricted by the number of unknowns available in the used WIPL-D license, thus, being limited to a few wavelengths. Measurements were performed to assess the accuracy of these geometrical models, considering three of the simulated cases: isolated antenna, MeRo and MeRC scenarios. Regarding the isolated antenna, measurements were performed in an anechoic chamber, showing a good agreement with the simulated results for both the  $E$ - and  $H$ -planes, although some discrepancies are found on the antenna’s backside ( $|\text{angles}| > 90^\circ$ ), clearly due to interference on measurements caused by the structure that supports the antenna under test. Measurements of MeRo and MeRC scenarios were performed in a real classroom, showing a general good agreement with the predicted results, but presenting slight fluctuations due to reflections resulting from more complex details of the real environment, which could not be accounted in simulations. It is concluded that the adopted geometrical models are a good approach to reproduce real scenarios. The reduced geometrical dimensions of WIPL-D models still lead to accurate results, do not restricting the overall evaluation.

Regarding the analysis of antenna’s RL curves in the various scenarios, one observes that the surrounding scenario generally decreases mismatch efficiency (up to 4 dB decrease) with respect to the case of the isolated antenna. For DiCo and MeRC scenarios, analogous results are found: matched impedance is obtained for lower frequencies and RL values decrease down to 4 dB, thus, decreasing system’s performance. When an antenna is installed on a metallic surface, like in

the MeCo scenario, its impedance modifies considerably and the analysis of RL curve shows that this situation leads to a  $RL < -1.79$  dB ( $VSWR < 9.75$ ), while a RL value below  $-5.55$  dB ( $VSWR < 3.24$ ) is obtained for the isolated antenna. The installation of an antenna on a metallic pole (MePo scenario) decreases antenna's impedance, leading to an approximately constant RL curve and, thus, to poorer performance. Installing an antenna on a dielectric wall with a metallic ceiling above (MeRo scenario) has a minor effect on its input impedance and the RL curve for this situation shows a similar behaviour within the frequency band as isolated antenna.

From the analysis of antenna's radiation patterns in the various scenarios, one concludes that the geometry of BS installation and also the materials surrounding the antenna have a great influence on the way it radiates in space, almost always leading to the deformation of antenna's free space radiation pattern. Installations like those represented by DiCo and MeRC scenarios, where the antenna is located in a dielectric corner, tend to increase directivity properties. This is particularly true when the antenna is mounted on a metallic box, as it is shown by results for the MeCo scenario. For installation on metallic poles (MePo scenario), the most visible effect is the attenuation of backward radiation lobe, although a reduction of vertical and horizontal HPBW's is also observed, leading to an increased antenna's directivity. The situation of an antenna installed on a dielectric wall, with a metallic roof above it (MeRo scenario) approaches the radiation pattern of the isolated antenna, even though with slight distortions on the vertical plane.

For all scenarios, the near-field values are predicted on both horizontal and vertical planes passing through antenna's origin. Simulations were run for different input powers, ranging from 100 mW to 50 W, in order to understand how the exclusion zone will modify according to the power feeding the antenna. A small application was developed in Matlab, receiving WIPL-D output files with near-field values for the various scenarios, then, through comparison with EMF reference levels for the frequency of operation, it traces the 2D exclusion zone. The exclusion radius,  $r_{scm0}$  for the plane of interest is subsequently calculated.

In order to understand how the exclusion radius modifies when a larger geometrical model is used, a modified version of the MeRo scenario with extended walls was created and simulated. The exclusion area obtained with the extended model maintains almost the same shape, although it becomes more restrictive for a factor of about 1.24. Considering the huge increase of 12 times in simulation time, one has decided to use the original model, however, having its limitations in mind. The same results are expected for extended models for the other scenarios, so all have been kept with the original dimensions.



This work does not give deterministic values for the extension and shape of exclusion zones for wireless antennas, because of the limitations of the geometrical models used. Instead, it provides qualitative results of great value to wireless operators, when dimensioning and installing new antennas.

The effects found on the shape and on the extension of exclusion zones stress the importance of not uncritically applying free space conditions to wireless networks planning tools. Regarding each particular scenario, some conclusions may be drawn:

- The DiCo scenario presents strictest results in the horizontal plane rather than in the vertical one. The exclusion zone may extend up to 2 times the one calculated in free space conditions.
- The MeCo scenario presents the most restrictive results, with  $r_{scno}$  reaching up to 5.7 times the exclusion radius calculated in free space conditions.
- The MePo scenario shows similar results for the horizontal and vertical planes, with the exclusion zone being about 1.3 times the one calculated in free space conditions.
- The influence of a metallic roof above an antenna has no expression in the horizontal plane, impacting essentially on the vertical one. For the MeRo scenario, the exclusion radius in the horizontal plane is almost equal to the one obtained for the isolated antenna, while in the vertical plane it doubles the one obtained in free space.
- Results for the MeRC scenario show a joint influence from the dielectric corner and the metallic ceiling. The dielectric corner has a major impact, extending the horizontal exclusion up to 1.9 times the one obtained in free space.

Adopting a worst-case perspective, it is concluded that, for common BS installation scenarios, the exclusion radius may be estimated as being twice the one obtained under free space conditions. Exception is made for corner configurations with a metallic part on the back of the antenna, where the exclusion radius may increase by a factor of 5.

Although all the work has been developed for a GSM900 antenna, the main conclusions are valid for the other wireless technologies mentioned in this thesis. In these frequency bands (900 MHz, 1800 MHz, 2 GHz, 2.5 GHz, 3.5 GHz, 5 GHz), no differences in the EMFs behaviour are

expected to occur, as the results are scalable with respect to the involved wavelengths.

Due to the complexity of the subject underlying this thesis, a wide range of issues can be improved in a future work, leading to a more realistic and detailed approach:

- Confirmation of results for other types of antennas used in BSs.
- Confirmation of results for the other technologies referred in this work, namely GSM1800, UMTS, WiFi and WiMAX.
- Addition of more objects to the geometrical model, such as the metallic barriers commonly used in rooftop installations, mast structures, etc.
- Analysis of further BS installation scenarios, considering also co-location of antennas and the impact of other radio sources.
- Use of more accurate approaches, such as combining of numerical simulation tools with ray-tracing techniques.

Although all these issues may lead to refined exclusion zones, it is important to state that it is unfeasible to precisely model the reality due to the complexity, the multiplicity, and the dynamic of variables present in each environment.

# **Annex A**

## **Antennas used in Wireless Communication Systems**

This annex presents technical information about the typical antennas used in the various wireless communication systems considered in this work.

This annex gives detailed information on common antennas employed in GSM900, GSM1800, UMTS and WiFi BSs and APs. For WiMAX technology, the WiMAX Forum is conducting an equipment certification programme, after which the products will be introduced in the market. Thus, for WiMAX technology, only the technical information in Table A.1 is presented in this annex.

Table A.1 – Technical characteristics for a WiMAX antenna (based on [WiMA06]).

Frequency range	2.5 GHz
Gain	15 dBi
Polarisation	Cross
Horizontal HPBW	70°

Some examples of typical outdoor antennas are given in the following figures. Table A.2 summarises the examples presented.

Table A.2 – Summary of typical BS outdoor antennas.

Antenna	Picture	Technical description
Sector GSM900	Figure A.1	Table A.3
Sector GSM1800	Figure A. 2	Table A.4
Sector UMTS	Figure A 3	Table A.5
Sector WiFi	Figure A.4	Table A.6
Omnidirectional GSM900	Figure A.5	Table A.7
Omnidirectional GSM1800/UMTS	Figure A.6	Table A.8
Omnidirectional WiFi	Figure A.7	Table A.9



Figure A.1 – Sector GSM900 antenna (extracted from [KATH05a]).

Table A.3 – Technical characteristics of a typical sector GSM900 antenna (extracted from [KATH05a]).

Type	Kathrein 737 547
Frequency range	870 – 960 MHz
Gain	17 dBi
Polarisation	Vertical
Horizontal HPBW	65°
Vertical HPBW	8.5°
Electrical downtilt	9°
Dimensions (height/width/depth)	1934/258/103 mm



Figure A. 2 - Sector GSM1800 antenna (extracted from [KATH05a]).

Table A.4 – Technical characteristics of a sector GSM1800 antenna (extracted from [KATH05a]).

Type	Kathrein 734 330
Frequency range	1710 – 1900 MHz
Gain	17.5 dBi
Polarisation	Vertical
Horizontal HPBW	90°
Vertical HPBW	5°
Electrical downtilt	2°
Dimensions (height/width/depth)	1942/155/49 mm



Figure A 3 - Sector UMTS antenna (extracted from [KATH05a]).

Table A.5 – Technical characteristics of a sector UMTS antenna (extracted from [KATH05a]).

Type	Kathrein 742 215
Frequency range	1710 – 2200 MHz
Gain	2 x 18 dBi
Polarisation	+45°/-45°
Horizontal HPBW	65°
Vertical HPBW	6.2°
Electrical downtilt	0°-10°
Dimensions (height/width/depth)	1302/155/69 mm



Figure A.4 - Sector antenna used for WiFi systems (extracted from [CISC06b]).

Table A.6 – Technical characteristics of a sector WiFi antenna (extracted from [CISC06b]).

Type	Cisco AIR-AINT1949
Frequency range	2.4-2.83 GHz
Gain	13.5 dBi
Polarisation	Vertical
Horizontal HPBW	30°
Vertical HPBW	25°
Electrical downtilt	-
Dimensions (height/diameter)	457/76 mm





Figure A.5 – Omnidirectional GSM900 antenna (extracted from [KATH05a]).

Table A.7 – Technical characteristics of an omnidirectional GSM900 antenna (extracted from [KATH05a]).

Type	Kathrein 736 350
Frequency range	870-960 MHz
Gain	8 dBi
Polarisation	Vertical
Horizontal HPBW	360°
Vertical HPBW	13°
Electrical downtilt	-
Dimensions (height/diameter)	1543/51 mm

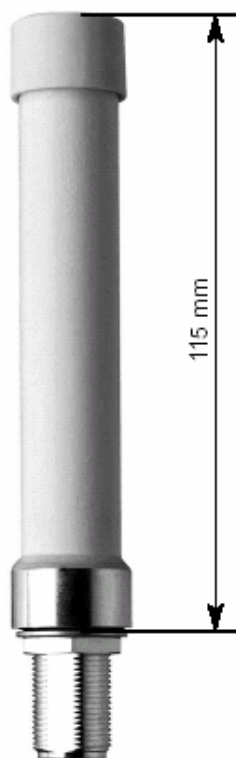


Figure A.6 – Omnidirectional GSM1800/UMTS antenna (extracted from [KATH05a]).

Table A.8 – Technical characteristics of an omnidirectional GSM1800/UMTS antenna (extracted from [KATH05a]).

Type	Kathrein 738 454
Frequency range	1710-2170 MHz
Gain	2 dBi
Polarisation	Vertical
Horizontal HPBW	360°
Vertical HPBW	78°
Electrical downtilt	-
Dimensions (height/diameter)	115/20 mm



Figure A.7 - Omnidirectional antenna used for WiFi systems (extracted from [CISC06b]).

Table A.9 – Technical characteristics of an omnidirectional WiFi antenna (extracted from [CISC06b]).

Type	Cisco AIR-ANT3213
Frequency range	2.4–2.83 GHz
Gain	5.2 dBi
Polarisation	Vertical
Horizontal HPBW	360°
Vertical HPBW	25°
Electrical downtilt	-
Dimensions (height/width/depth)	304/127/25 mm

Some examples of typical indoor antennas are given in the following figures. Table A.10 summarises the examples presented.

Table A.10 – Summary of typical indoor antennas.

Antenna	Picture	Technical description
GSM900	Figure A.8	Table A.11
WiFi	Figure A.9	Table A.12
Bidirectional multi band (GSM900/GSM1800/UMTS)	Figure A.10	Table A.13
Omnidirectional multi band (GSM900/GSM1800/UMTS/WiFi)	Figure A.11	Table A.14

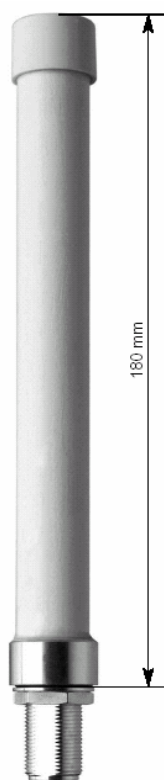


Figure A.8 – Omnidirectional GSM indoor antenna(extracted from [KATH05a]).

Table A.11 – Technical characteristics of an omnidirectional GSM indoor antenna (extracted from [KATH05a]).

Type	Kathrein 738 450
Frequency range	870-960 MHz
Gain	2 dBi
Polarisation	Vertical
Horizontal HPBW	360°
Vertical HPBW	78°
Electrical downtilt	-
Dimensions (height/diameter)	180/20 mm



Figure A.9 – WiFi indoor omnidirectional antenna (extracted from [CISC06b]).

Table A.12 – Characteristics of a WiFi indoor omnidirectional antenna.

Type	Cisco Aironet 1100
Frequency range	2.4-2.5 GHz
Gain	2 dBi
Polarisation	Linear
Horizontal HPBW	360°
Vertical HPBW	50°
Electrical downtilt	-
Dimensions (height/width/deep)	205/104/38 mm

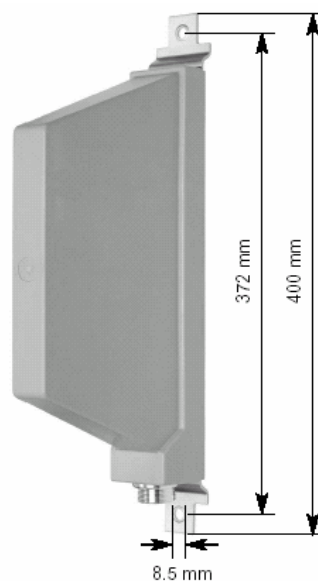


Figure A.10 – Indoor bi-directional multi band antenna(extracted from [KATH05a]).

Table A.13 – Technical characteristics of an indoor bi-directional multi band antenna (extracted from [KATH05a]).

Type	Kathrein 738 446
Frequency range	824-960 MHz 1710-1880 MHz 1880-2170 MHz
Gain	824-960 MHz: 5 dBi 1710-1880 MHz: 5.5 dBi 1880-2170 MHz: 6.5 dBi
Polarisation	Vertical
Horizontal HPBW	65°
Vertical HPBW	N/A
Electrical downtilt	-
Dimensions (height/width/depth)	310/55/190 mm



Figure A.11 – Indoor omnidirectional multi band antenna(extracted from [KATH05a]).

Table A.14 – Technical characteristics of an indoor omnidirectional multi band antenna (extracted from [KATH05a]).

Type	Kathrein 800 10249
Frequency range	806-960 MHz 1425-3600 MHz 5150-6000 MHz
Gain	2 dBi
Polarisation	Vertical
Horizontal HPBW	360°
Vertical HPBW	N/A
Electrical downtilt	-
Dimensions (height)	94 mm



# **Annex B**

## **Simulation of the 736 624 Kathrein Antenna**

This annex reports on the numerical simulation of the 736 624 Kathrein antenna, based on the detailed technical information provided by Kathrein. Three models of the antenna were simulated and compared. Based on the results obtained for the radiation pattern and the impedance, one of these models was chosen to be used in the different simulation scenarios of this thesis.

Given the 736 624 Kathrein antenna, chosen as an example of a real antenna to be studied, an analysis of numerical EM models of the antenna was required in order to obtain an adequate model for it. Detailed information on the technical characteristics and actual configuration of the antenna were kindly provided by Kathrein. This annex reports on the work developed to simulate the antenna and on the results obtained.

The 736 624 Kathrein antenna is an indoor directional one, operating in the GSM900 frequency band, with the technical characteristics presented in Table B.1. Figure B.1 represents the general aspect of the antenna, and Figure B.2 its internal components. The horizontal and vertical radiation patterns of this antenna provided by the manufacturer are presented in Figure B.3.

Table B.1 – Technical characteristics of the 736 624 Kathrein antenna (extracted from [KATH05b]).

Frequency range	870–960 MHz
VSWR	< 1.5
Gain	7 dBi
Impedance	50 $\Omega$
Horizontal HPBW	90°
Vertical HPBW	65°
Polarisation	Vertical
Max. Power	50 W (@ 50°C ambient temperature)
Weight	500 g
Dimensions (height/width/depth)	205/155/32 mm

Simulations were performed using the WIPL-D [WIPL05] software tool. Based on the sketches and on further information kindly provided by Kathrein, a preliminary basic geometric structure was created, composed by three metallic plates fed by a generator on the central one. From this preliminary structure, three simple geometrical models of the antenna were designed, Table B.2,

the degree of accuracy being increased from Model 1 to Model 3, implying a larger number of problem unknowns. The geometrical model may be improved by gathering further information on the antenna, however, the results obtained are satisfactory. A compromise solution between the quality of the results and the number of problem unknowns was obtained. The use of a low number of unknowns in the antenna model is essential, in order to have enough free variables to simulate objects in a real environment near the antenna in a next stage.



Figure B.1 – The 736 624 Kathrein antenna (extracted from [KATH05b]).

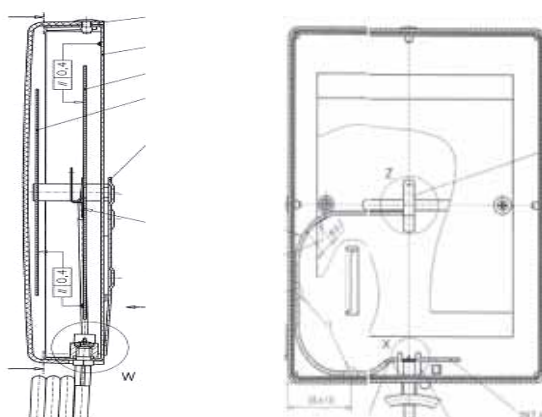


Figure B.2 – Internal components of the 736 624 Kathrein antenna (side and front views) [KATH05c].

The antenna has an input impedance of  $50 \Omega$ , therefore, from Table B.3, one can observe that Model 3 leads to the best results.

The 3D radiation patterns, and the horizontal and vertical cuts, are presented from Figure B.7 to Figure B.12. Table B.4 summarises the results obtained for the three simulation models. Note that HPBW's were calculated with a  $0.6^\circ$  resolution. By comparing the results obtained from simulations with the characteristics presented in Table B.1, one can observe a very good agreement and conclude that Models 1 and 3 are the most accurate ones.

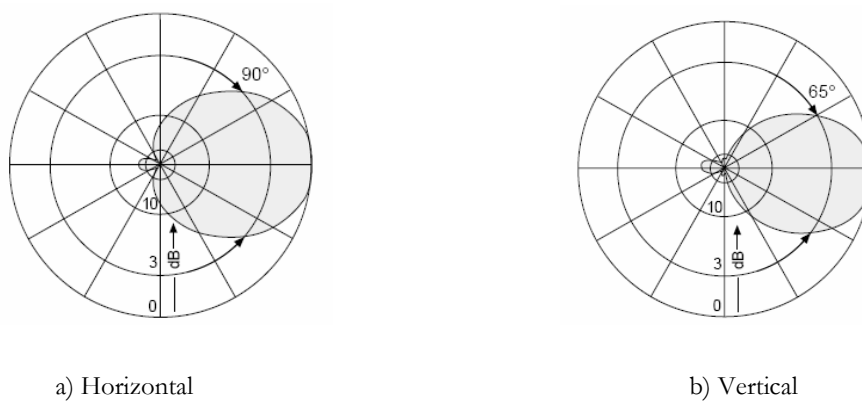


Figure B.3 – Radiation patterns.

Table B.2 – Description of the geometrical models.

Model	Description	Figure
1	Wires simulating the short circuit between plates.	Figure B.4
2	Metallic cylinders simulating the short circuit between plates.	Figure B.5
3	Metallic cylinders simulating the short circuit between plates. Higher detail on the feeding point.	Figure B.6



Figure B.4 – Simulation of the 736 624 Kathrein antenna (Model 1).



Figure B.5 – Simulation of the 736 624 Kathrein antenna (Model 2).

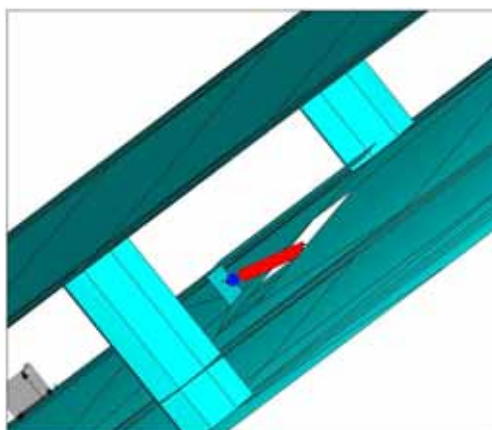


Figure B.6 – Simulation of the 736 624 Kathrein antenna (Model 3).

Table B.3 – Input impedance for the three models ( $f = 902.5$  MHz).

Model	Input impedance [ $\Omega$ ]
1	$20.70 + j3.37$
2	$25.88 - j7.76$
3	$32.98 - j1.13$

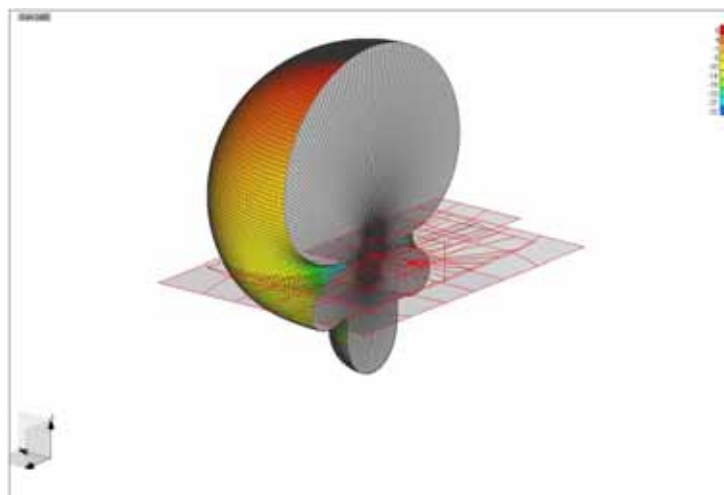
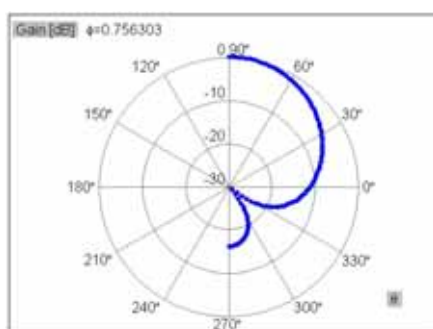
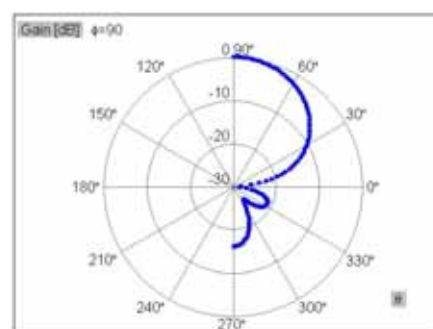


Figure B.7 - 3D radiation pattern (Model 1).



a) Horizontal



b) Vertical

Figure B.8 – Radiation patterns (Model 1).

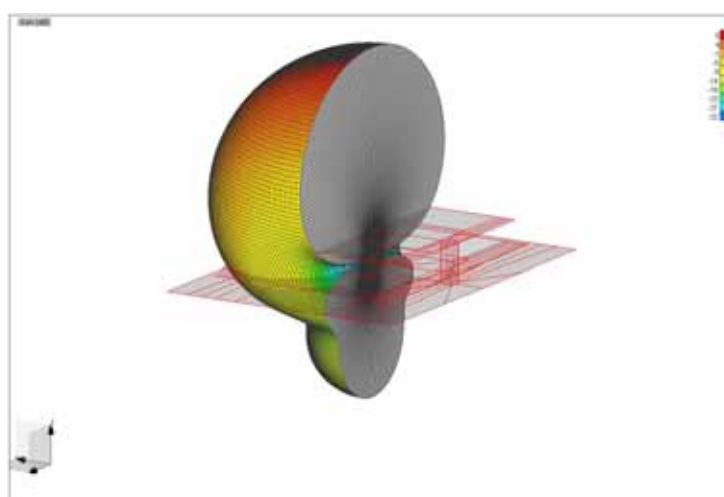
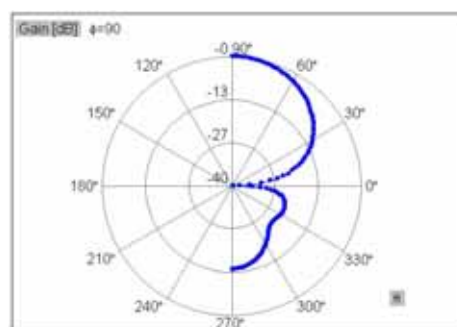


Figure B.9 – 3D radiation pattern (Model 2).



a) Horizontal



b) Vertical

Figure B.10 – Radiation patterns (Model 2).

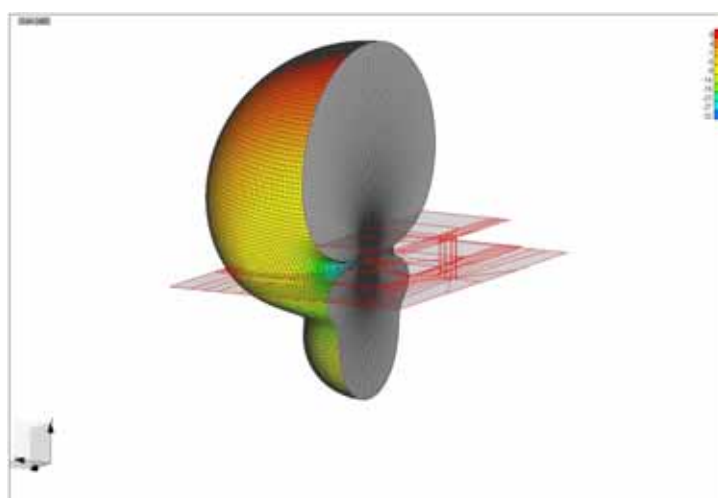
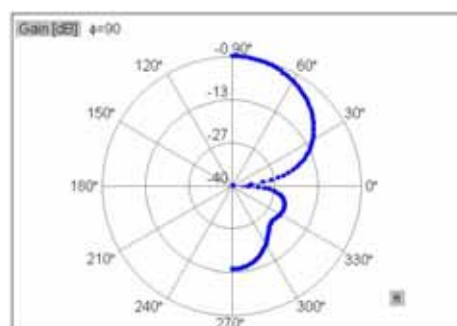


Figure B.11 – 3D radiation pattern (Model 3).



a) Horizontal



b) Vertical

Figure B.12 – Horizontal and vertical patterns (Model 3).

From the results obtained, Model 3 is the one chosen to simulate the 736 624 Kathrein antenna. While this model does not yield perfect results in terms of impedance, the results for radiation pattern are in good agreement with the reference ones. A difference of 1.38 dB is achieved in terms of gain and a minor difference of 5° in the horizontal pattern HPBW is attained.

Table B.4 – Radiation characteristics for the three models.

Model	Gain [dBi]	Horizontal HPBW [°]	Vertical HPBW [°]
1	8.13	88	65
2	8.38	85	64
3	8.38	85	65

An extended analysis on the GSM900 frequency band was performed for Model 3. From the RL curve presented in Figure B.13, one may observe matched impedance at 900 MHz, with  $RL < 5.55$  dB ( $VSWR < 3.24$ ) for the overall band of interest.

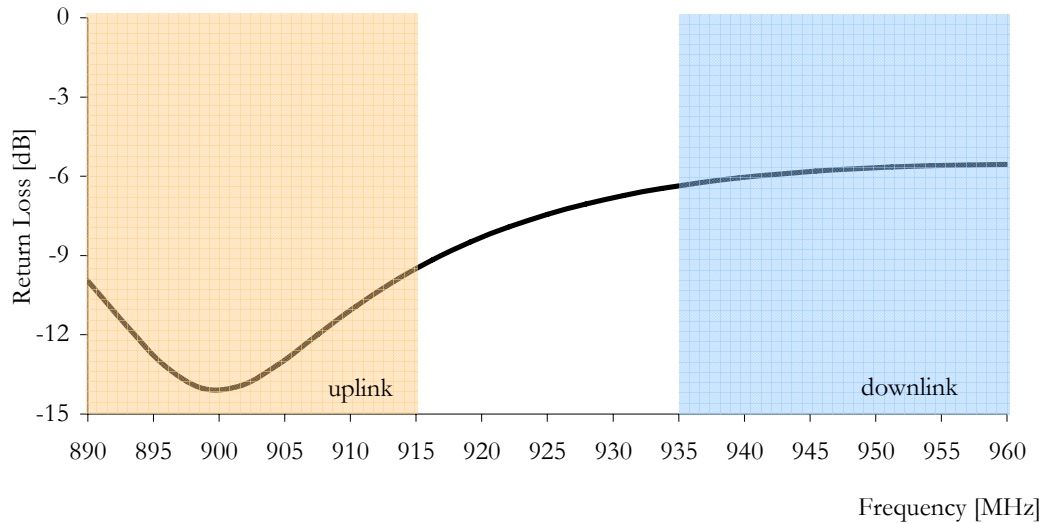


Figure B.13 – Return loss curve for Model 3.



# **Annex C**

## **Study on the Accuracy of Numerical Simulations**

A study on the accuracy of numerical simulations was performed, being reported in this annex. Section C.1 evaluates the impact of improving the accuracy of the integrals and the order of current approximation used in the computations, as well as of extending the frequency range of the analysis. Section C.2 reports on the influence of the geometrical model on the results, while Section C.3 addresses the use of symmetry in some scenarios. Important conclusions are obtained from the different analyses performed.

## C.1 Accuracy of the parameters of the analysis

In order to improve the accuracy of the solution, WIPL-D allows the user to change some of the parameters used in the computations. The accuracy of the integrals used, the order of current approximation and the frequency range of the analysis are examples of these parameters.

The order of numerical integration performed during computations may vary through successive grades, which improve the accuracy of the overall analysis, while consuming higher processing times. The WIPL-D user may choose these different grades of integral accuracy, which vary from *Normal* to *Enhanced 1-10* grades, where *Enhanced 10* is the most accurate, and time-consuming, one.

The user may also change the orders of current expansion along all plates and wires, which are of polynomial type. These orders also vary from *Normal* to *Enhanced 1-10*, where *Enhanced 10* is the higher order, and time-consuming, one.

The electrical size of the structure under analysis is determined with respect to the higher limit of the frequency range. Since the analysis is performed at the lower limit of the frequency range, increasing the higher limit increases the order of current expansion, thus, improving the solution and increasing the time for analysis.

For the five scenarios under analysis in this thesis, various simulation modes were set, by using different combinations of the parameters mentioned above, Table C.1. The horizontal and vertical radiation patterns obtained are presented from Figure C.1 to Figure C.5 for each one of the five simulation scenarios. The differences in the horizontal and vertical radiation patterns are quantified through the parameter  $\varepsilon_s$ , which measures the difference (in dB) between the radiation patterns of simulation modes 3 and  $s$ ,

$$\varepsilon_s = G(\theta, \phi)_3 - G(\theta, \phi)_s. \quad (C.1)$$

where:

- $G(\theta, \phi)_3$  - Antenna gain for simulation mode 3 [dB].

- $G(\theta, \phi)_s$  – Antenna gain for simulation mode  $s$  [dB].

It is important to define various statistical parameters for  $\varepsilon_s$  in a general way, as it is systematically used along this annex. So, given a particular  $\varepsilon$ , one defines its average value,  $\bar{\varepsilon}$ , by (C.2); its root mean square value,  $\sqrt{\varepsilon^2}$ , by (C.3) and a weighted average value,  $\bar{\varepsilon}_w$ , by (C.4).

$$\bar{\varepsilon} = \frac{\sum_{n=1}^{N_A} \varepsilon_n}{N_A}. \quad (C.2)$$

where:

- $\varepsilon_n$  –  $\varepsilon$  computed for each radiation angle.
- $N_A$  – Number of radiation angles.

$$\sqrt{\varepsilon^2} = \sqrt{\frac{\sum_{n=1}^{N_A} \varepsilon_n^2}{N_A}}. \quad (C.3)$$

$$\bar{\varepsilon}_w = \frac{\sum_{n=1}^{N_A} 10^{G_{n_{ref}}/10} \varepsilon_n}{\sum_{n=1}^{N_A} 10^{G_{n_{ref}}/10}}. \quad (C.4)$$

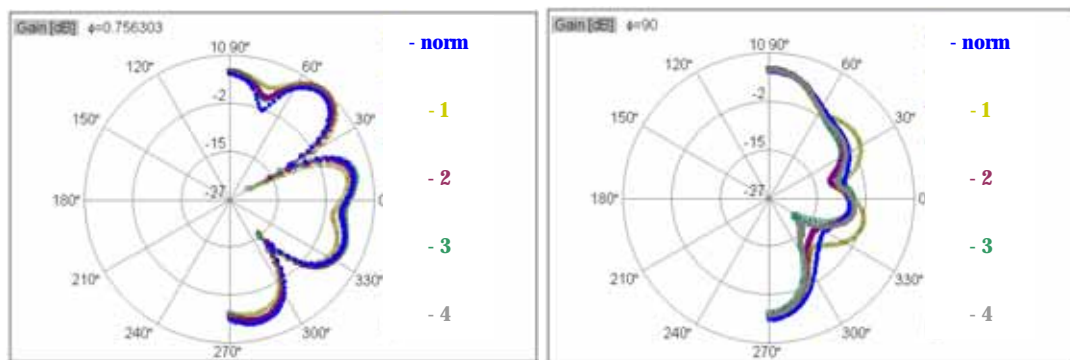
where:

- $G_{n_{ref}}$  – Gain of a reference antenna for a particular radiation direction [dB].

The statistical parameters for  $\varepsilon_s$ , the simulation time (using a Pentium 4 @ 2.2 GHz) and the number of used unknowns are presented in Table C.2 to Table C.6 for each one of the five simulation scenarios.

Table C.1 – Simulations performed with different accuracies of parameters.

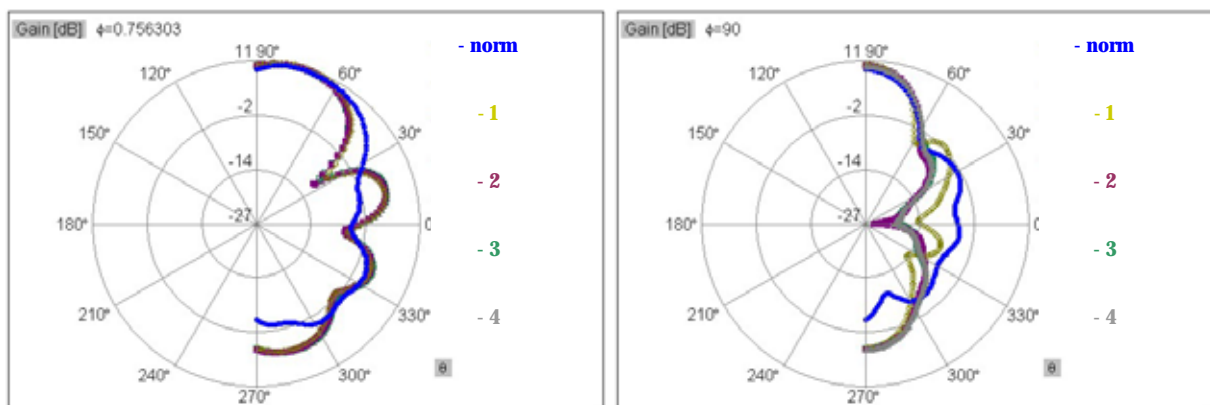
Simulation mode, $\varsigma$	Integral accuracy	Order of Currents	Frequency range, [MHz]
norm	Normal	Normal	902.5 - 960
1	Enhanced 1	Enhanced 1	902.5 - 960
2	Enhanced 2	Enhanced 2	902.5 - 960
3	Enhanced 3	Enhanced 3	902.5 - 960
4	Enhanced 1	Enhanced 1	902.5 - 1 050



a) Horizontal

b) Vertical

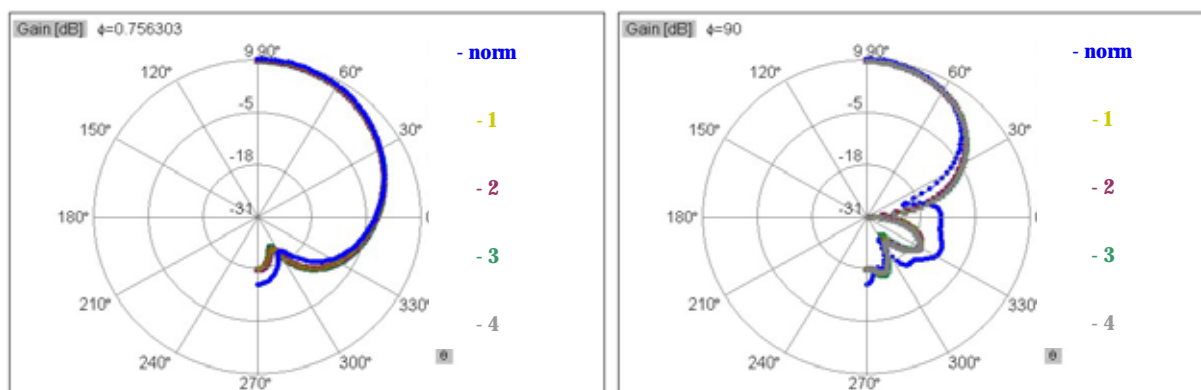
Figure C.1 – Radiation patterns for the DiCo scenario.



a) Horizontal

b) Vertical

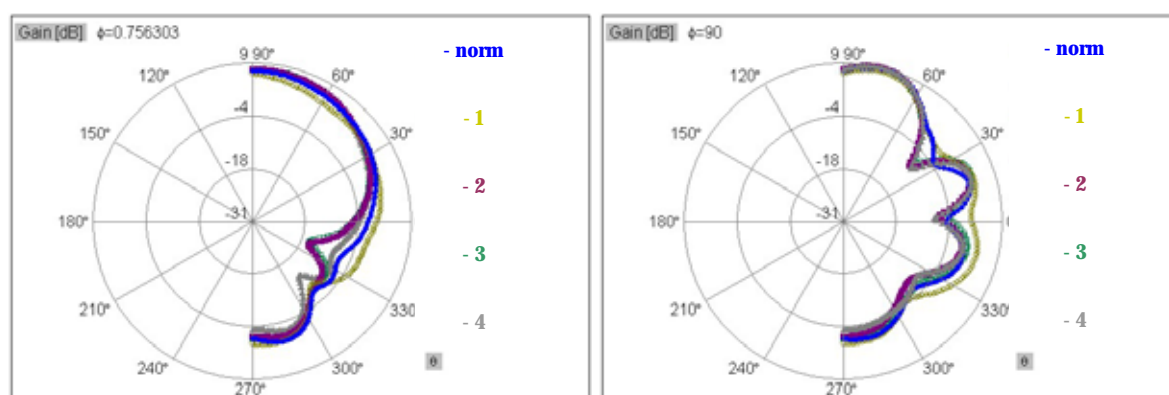
Figure C.2 – Radiation patterns for the MeCo scenario.



a) Horizontal

b) Vertical

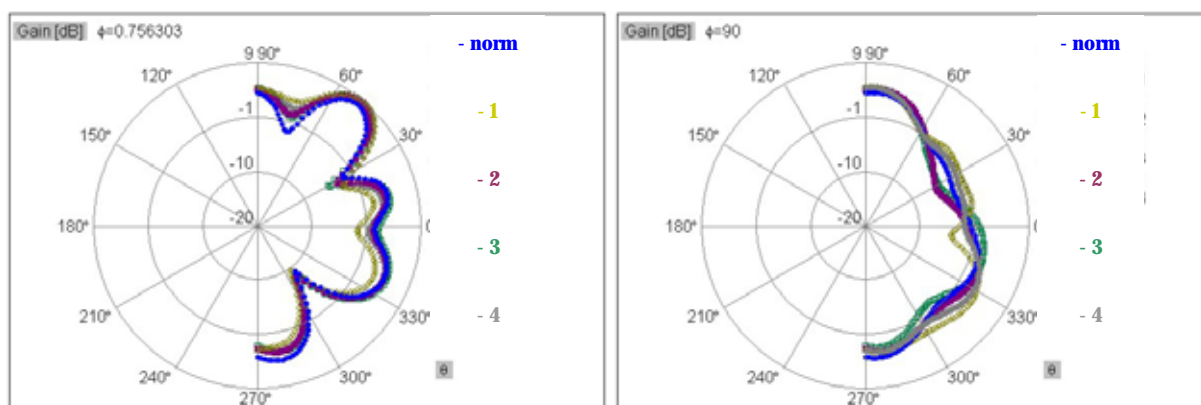
Figure C.3 – Radiation patterns for the MePo scenario.



a) Horizontal

b) Vertical

Figure C.4 – Radiation patterns for the MeRo scenario.



a) Horizontal

b) Vertical

Figure C.5 – Radiation patterns for the MeRC scenario.

Table C.2 – Simulation results for the DiCo scenario.

	Horizontal pattern			Vertical pattern			CPU time [s]	Number of unknowns
$s$	$\bar{\varepsilon}_s$ [dB]	$\sqrt{\varepsilon_s^2}$ [dB]	$\varepsilon_{w_s}$ [dB]	$\bar{\varepsilon}_s$ [dB]	$\sqrt{\varepsilon_s^2}$ [dB]	$\varepsilon_{w_s}$ [dB]		
norm	0.17	1.78	0.60	-2.13	3.38	-0.36	40	1 502
1	0.49	3.25	0.56	-3.11	4.79	-0.45	75	2 112
2	-0.03	0.95	0.11	-0.93	2.05	-0.18	121	2 579
4	0.21	0.99	0.14	-0.47	1.05	-0.16	205	3 118

Table C.3 – Simulation results for the MeCo scenario.

	Horizontal pattern			Vertical pattern			CPU time [s]	Number of unknowns
$s$	$\bar{\varepsilon}_s$ [dB]	$\sqrt{\varepsilon_s^2}$ [dB]	$\varepsilon_{w_s}$ [dB]	$\bar{\varepsilon}_s$ [dB]	$\sqrt{\varepsilon_s^2}$ [dB]	$\varepsilon_{w_s}$ [dB]		
norm	1.05	4.28	1.10	-2.80	7.66	2.02	30	1 068
1	0.10	0.86	-0.19	-1.73	4.45	0.13	52	1 520
2	0.26	0.47	0.03	0.35	1.30	-0.05	78	1 739
4	0.11	0.18	0.02	0.16	0.40	-0.04	111	2 548

Table C.4 – Simulation results for the MePo scenario.

	Horizontal pattern			Vertical pattern			CPU time [s]	Number of unknowns
$s$	$\bar{\varepsilon}_s$ [dB]	$\sqrt{\varepsilon_s^2}$ [dB]	$\varepsilon_{w_s}$ [dB]	$\bar{\varepsilon}_s$ [dB]	$\sqrt{\varepsilon_s^2}$ [dB]	$\varepsilon_{w_s}$ [dB]		
norm	-0.06	2.13	-0.15	-2.05	6.23	0.03	28	728
1	0.12	0.25	0.02	0.14	1.02	-0.06	44	1 004
2	0.09	0.24	-0.01	0.32	1.58	-0.03	87	1 711
4	0.11	0.27	-0.01	0.39	1.52	-0.05	111	2 548

Table C.5 – Simulation results for the MeRo scenario.

$s$	Horizontal pattern			Vertical pattern			CPU time [s]	Number of unknowns
	$\bar{\varepsilon}_s$ [dB]	$\sqrt{\varepsilon_s^2}$ [dB]	$\varepsilon_{w_s}$ [dB]	$\bar{\varepsilon}_s$ [dB]	$\sqrt{\varepsilon_s^2}$ [dB]	$\varepsilon_{w_s}$ [dB]		
norm	-1.54	2.93	0.25	-0.23	1.69	0.28	31	1 068
1	-1.86	4.45	1.05	-1.75	2.63	-0.09	52	1 520
2	0.06	0.61	0.03	0.92	1.20	0.24	79	1 739
4	0.16	2.22	0.25	1.12	1.55	0.29	111	2 548

Table C.6 – Simulation results for the MeRC scenario.

$s$	Horizontal pattern			Vertical pattern			CPU time [s]	Number of unknowns
	$\bar{\varepsilon}_s$ [dB]	$\sqrt{\varepsilon_s^2}$ [dB]	$\varepsilon_{w_s}$ [dB]	$\bar{\varepsilon}_s$ [dB]	$\sqrt{\varepsilon_s^2}$ [dB]	$\varepsilon_{w_s}$ [dB]		
norm	0.28	1.23	0.54	-0.45	1.31	-0.08	41	1 542
1	0.87	2.23	0.70	-1.22	2.85	-0.42	79	2 192
2	0.18	0.53	0.19	-0.16	1.11	-0.13	131	2 691
4	0.23	1.15	0.12	-0.84	1.81	-0.36	92	2 360

From the results obtained, it is concluded that the “best” simulation mode depends on each particular scenario. For each case, the average and RMS values have been analysed in conjunction with the weighted average. It is observed that high values of  $\bar{\varepsilon}_s$  do not necessary mean severe differences, instead, one has to look at the radiation patterns and to examine  $\varepsilon_{w_s}$ , which seems to be the most adequate statistical parameter. Inspection of the evolution of CPU times and of used unknowns (note that using few unknowns is essential to have enough free variables to simulate objects near to the BS antenna.) was also a decisive factor to choose on the simulation mode for each scenario. Thus, based on a trade-off between the quality of the results and the number of unknowns adopted, the following choices were taken:

- For the DiCo scenario, the simulation mode should be  $s = \text{norm}$ .

- For the MeCo scenario, the simulation mode should be  $s = 2$ .
- For the MePo scenario, the simulation mode should be  $s = 1$ .
- For the MeRo scenario, the simulation mode should be  $s = 2$ .
- For the MeRC scenario, the simulation mode should be  $s = \text{norm}$ .

## C.2 Accuracy of the geometrical model

As already referred, an adequate geometrical model of the structure of interest should be defined in order to obtain good results. Models that are more precise usually require a longer analysis time; hence, simple geometrical models should be created, still providing acceptable results.

For the MePo scenario, which is only composed of metallic elements, different geometrical models of the lamp pole were analysed, varying the height and the radius on both extremes, Figure C.6 and Table C.7. The radiation patterns obtained for each model are presented in Figure C.7. The differences (in dB) in the horizontal and vertical radiation patterns are quantified through the parameter  $\varepsilon_{\text{geom}_m}$ , defined by (C.5). The average,  $\bar{\varepsilon}_{\text{geom}_m}$ , the root mean square,  $\sqrt{\varepsilon_{\text{geom}_m}^2}$ , the weighted average,  $\varepsilon_{w_{\text{geom}_m}}$ , the simulation time and the number of used unknowns are presented in Table C.8 and Table C.9.

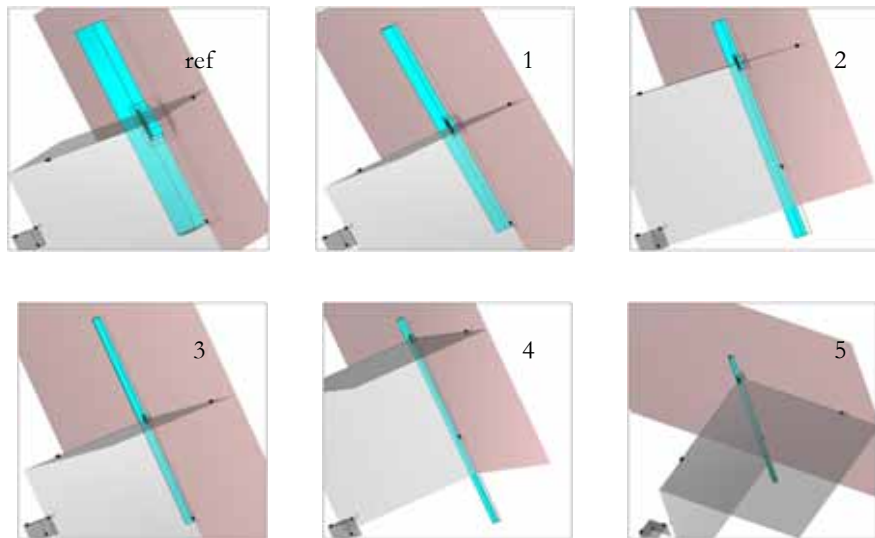


Figure C.6 – Geometrical models for the MePo scenario.



Table C.7 – Geometrical models for the MePo scenario.

$m$	Height, $b_{cyl}$ [m]	Radius (top of the cylinder) [m]	Radius (base of the cylinder) [m]	Position of the antenna
ref	1	0.1	0.1	$b_{cyl}/2$
1	2	0.1	0.1	$b_{cyl}/2$
2	2.5	0.1	0.1	$4b_{cyl}/5$
3	4	0.1	0.1	$b_{cyl}/2$
4	5	0.15	0.158	$9b_{cyl}/10$
5	3	0.15	0.158	$5b_{cyl}/6$

$$\varepsilon_{geom\_m} = G(\theta, \phi)_{ref} - G(\theta, \phi)_m. \quad (C.5)$$

where:

- $G(\theta, \phi)_{ref}$  - Antenna gain for a reference model [dB].
- $G(\theta, \phi)_m$  - Antenna gain for model  $m$  [dB].

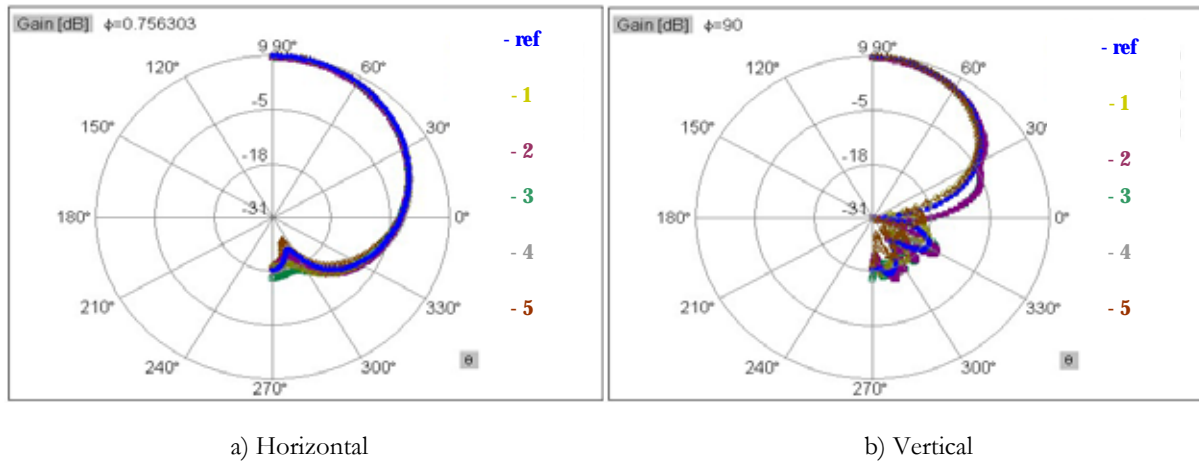


Figure C.7 – Radiation patterns for the different geometrical models (MePo scenario).

The DiCo scenario was chosen as an example of a scenario having not only metallic, but also dielectric elements. For this scenario, two models of the wall corner were simulated, varying the height of the wall, Figure C.8 and Table C.10. The radiation patterns obtained are presented in Figure C.9. Table C.11 presents the differences in the radiations patterns between these two models, and Table C.12 presents the simulation time and the number of used unknowns.

Table C.8 – Simulation results for the MePo scenario.

$m$	Horizontal pattern			Vertical pattern		
	$\bar{\varepsilon}_{geom\_m}$ [dB]	$\sqrt{\varepsilon^2_{geom\_m}}$ [dB]	$\varepsilon_{w_{geom\_m}}$ [dB]	$\bar{\varepsilon}_{geom\_m}$ [dB]	$\sqrt{\varepsilon^2_{geom\_m}}$ [dB]	$\varepsilon_{w_{geom\_m}}$ [dB]
1	-0.61	1.40	-0.07	-0.06	5.08	0.04
2	-0.28	0.85	0.23	-1.61	5.35	0.07
3	-	1.80	0.27	-1.46	5.89	0.07
4	-0.23	0.37	-0.03	0.74	4.29	0.07
5	0.85	1.32	-0.16	1.92	5.91	-0.04

Table C.9 – Comparison of CPU resources (MePo scenario).

$m$	CPU time [s]	Number of unknowns
ref	49	696
1	61	1 019
2	65	1 114
3	99	1 722
4	99	1 722
5	100	1 722

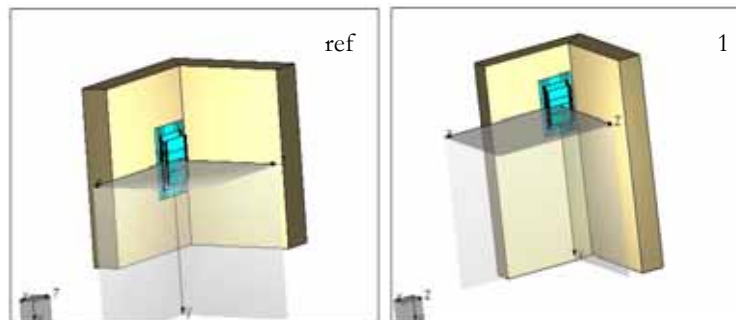


Figure C.8 – Geometrical models for the DiCo scenario.

For the MePo scenario, one may conclude that the increase of the pole's height originates minor differences on the horizontal pattern, while producing higher differences in the vertical one. This

result is expected, because the geometrical model was varied in the vertical plane. Comparing models 1 and 3, where the pole has increased 50 cm and 1 m for both sides of the antenna, respectively, on average, one may observe slight differences in the horizontal pattern, while observing a maximum of 1.46 dB in the vertical one. Similar results are obtained when the antenna is positioned asymmetrically in the pole (models 2 and 4), with different heights. Furthermore, the increase on the radius of the pole produces higher differences in the horizontal pattern. In terms of simulation time, the increase on the pole's height originates higher simulation times, as expected. In terms of unknowns, one may observe that there is no linear relation between the increase of the height and the number of unknowns. A small increase of 1 m in the height uses 323 more unknowns, while an increase of 3 m produces an increment of 1026 unknowns. For heights higher than 3 m, the number of unknowns seems to increase slowly.

Table C.10 – Geometrical models for the DiCo scenario.

$m$	Height, $h_{wall}$ [m]	Position of the antenna
ref	0.5	$h_{wall}/2$
1	0.75	$4h_{wall}/11$

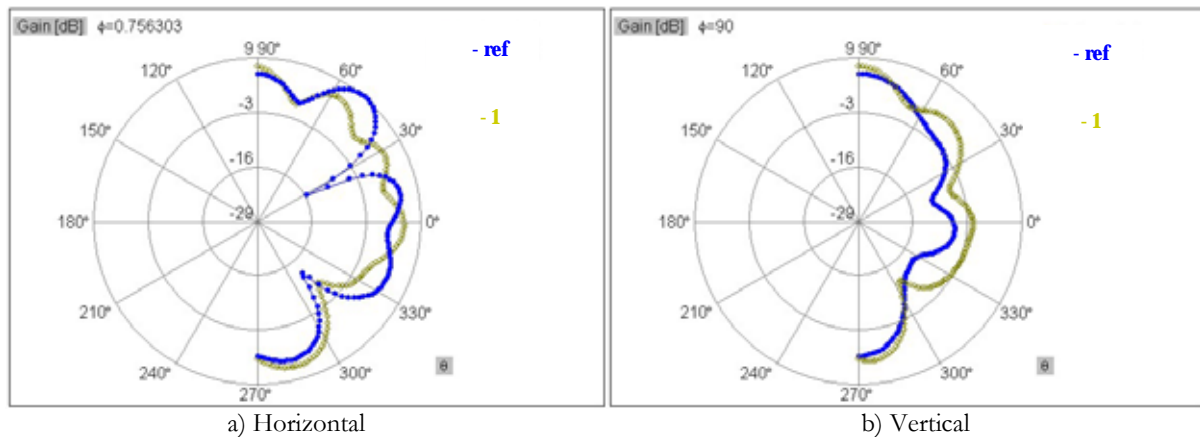


Figure C.9 – Radiation patterns for the different geometrical models (DiCo scenario).

From the results obtained for the DiCo scenario, with a dielectric wall, it is observed that changing the height of the wall from 50 to 75 cm is prohibitive in terms of the number of unknowns. Similarly to the metallic case, augmenting the height of the wall has a minor influence on the horizontal pattern and a higher influence and dispersion of values on the vertical one (average difference of 3.4 dB and 4.28 dB of dispersion).

Table C.11 – Simulation results for the DiCo scenario.

	Horizontal pattern			Vertical pattern		
$m$	$\bar{\varepsilon}_{geom\_m}$ [dB]	$\sqrt{\varepsilon^2_{geom\_m}}$ [dB]	$\varepsilon_{w_{geom\_m}}$ [dB]	$\bar{\varepsilon}_{geom\_m}$ [dB]	$\sqrt{\varepsilon^2_{geom\_m}}$ [dB]	$\varepsilon_{w_{geom\_m}}$ [dB]
1	-0.15	4.33	1.79	-3.40	4.28	-1.64

Table C.12 – Comparison of CPU resources (DiCO scenario).

$m$	CPU time [s]	Number of unknowns
ref	121	2 759
1	243	3 808

One may conclude that, in scenarios having metallic objects, increasing the size of the geometrical model is not prohibitive in terms of the results obtained for radiation pattern and also for the number of unknowns. Thus, a more realistic approach will be followed, choosing model  $m = 4$ . For the dielectric case, the geometrical model should be as small as possible, keeping in mind the differences in the vertical pattern, in order to have enough free unknowns to simulate a more realistic case. Therefore, model  $m = \text{ref}$  is chosen.

### C.3 Use of symmetry

For scenarios having both geometry and excitation symmetrical to a same basic coordinate plane, WIPL-D allows one to use symmetry properties to speed up the analysis. In these cases, only half of the structure is defined, thus, resulting in a reduced number of simulation unknowns and of CPU time used (approximately halved compared with the analysis of the original problem). This means that the maximum electrical size that WIPL-D can handle is doubled.

In MePo and MeRo scenarios, both the geometry and excitation are symmetrical to the yOz plane, so symmetry properties can be used. However, as the definition of the geometrical model is different from the original problem, some differences are expected. For both scenarios, the differences between radiation patterns of the problem using symmetry and the original one are

analysed through the parameter  $\varepsilon_{sym\_s}$ , which measures the difference (in dB) between the radiation patterns of the symmetry model and original one, in simulation mode  $s$ , defined by

$$\varepsilon_{sym\_s} = G(\theta, \phi)_{sym\_s} - G(\theta, \phi)_{original\_s}. \quad (C.6)$$

where:

- $G(\theta, \phi)_{sym\_s}$  – Antenna gain for the symmetry model, in simulation mode  $s$  [dB].
- $G(\theta, \phi)_{original\_s}$  – Antenna gain for the original model, in simulation mode  $s$  [dB].

The radiation patterns obtained for the MePo scenario are presented in Figure C.10, while Figure C.11 and Figure C.12 present the radiation patterns obtained for the MeRo scenario. The mean, the RMS and the weighted average values of  $\varepsilon_{sym\_s}$  are presented in Table C.13 and Table C.15, for MePo and MeRo scenarios, respectively.

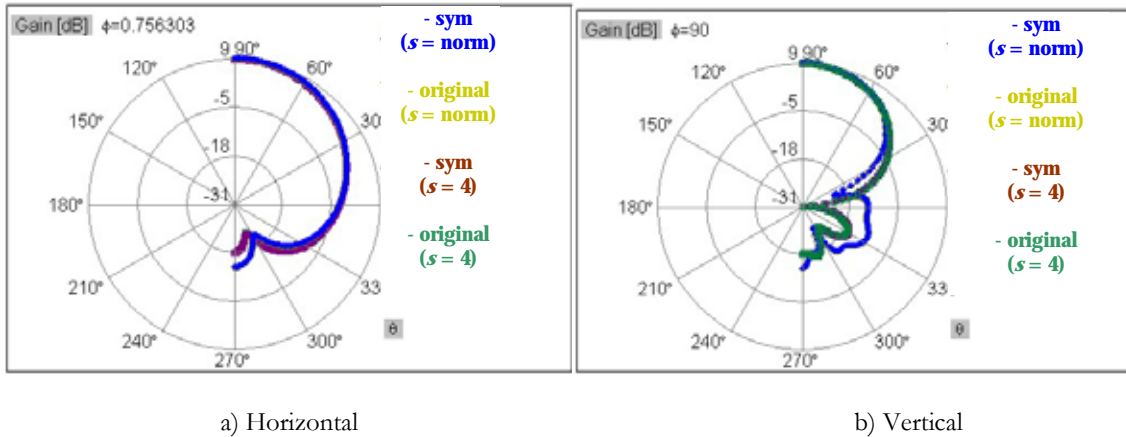


Figure C.10 – Radiation patterns obtained for the MePo scenario.

Table C.14 and Table C.16 present a comparison between the CPU time and the number of unknowns required for simulation of symmetry and original models for MePo and MeRo scenarios, respectively.

For the MePo one may observe minor differences when comparing the horizontal and vertical radiation patterns of the symmetry model with those of the original one, a maximum average difference of 0.06 dB being found. Moreover, one may observe minor differences in terms of simulation time, but a reasonable reduction in the number of unknowns required for simulation of the symmetry model. These observations are valid for the normal mode of simulation, as well as for mode 4. One concludes that symmetry properties should be used in simulations of the

MePo scenario, without any loss of accuracy of the results.

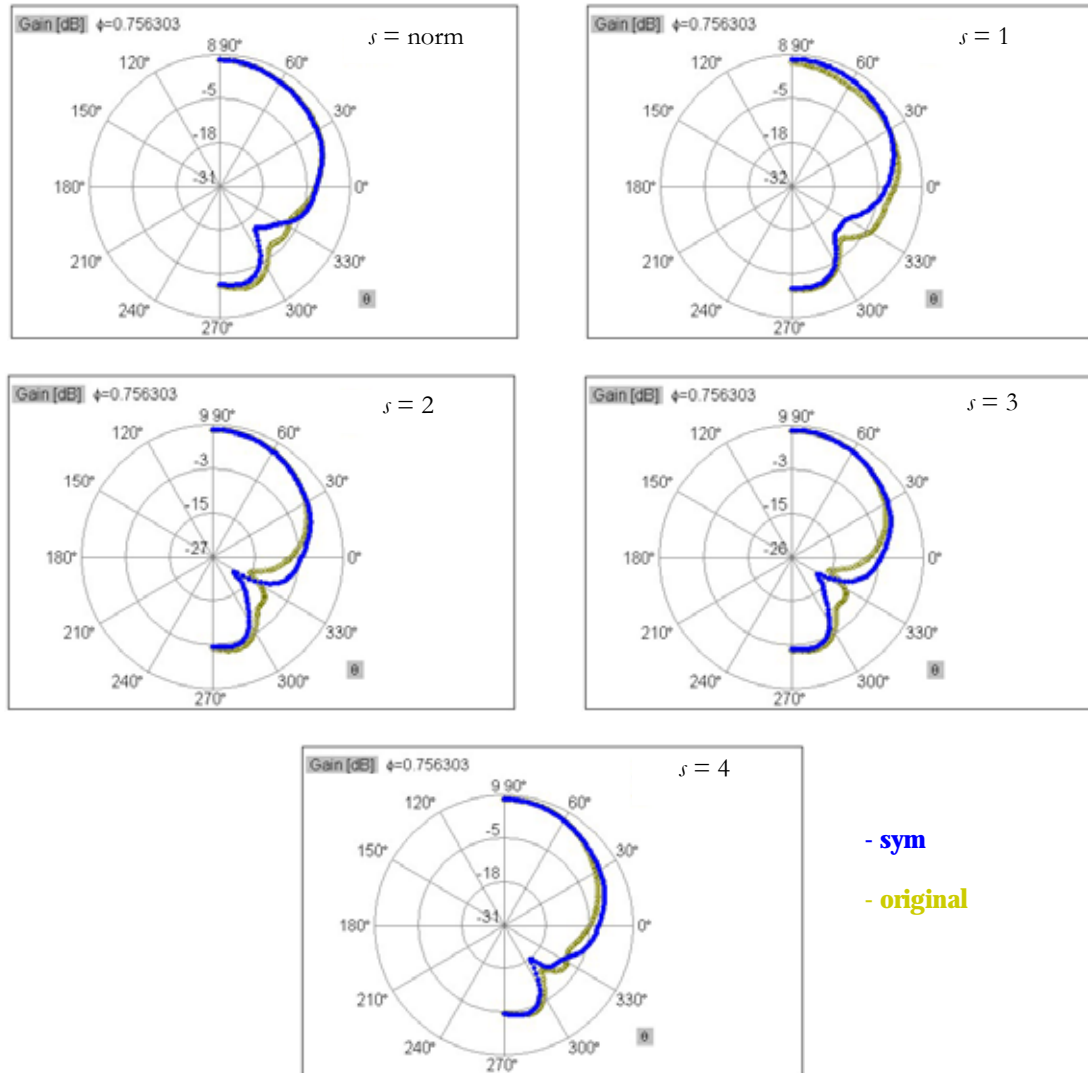


Figure C.11 – Horizontal radiation pattern obtained for the MeRo scenario.

When comparing the results for the MeRo scenario with and without symmetry, a better agreement between horizontal and vertical radiation patterns for accurate simulation modes is verified. In Table C.15, one may observe considerable RMS values and minor weighted average values. The reason for this is that the main differences in radiation patterns are reached in back directions, while a good agreement in main radiation direction is obtained. In general, for the different simulation modes, a slight reduction on simulation time and a considerable reduction in the number of unknowns are achieved. For this scenario, the use of symmetry with  $s = 4$  seems to be a good trade-off between accuracy of results and number of required unknowns.

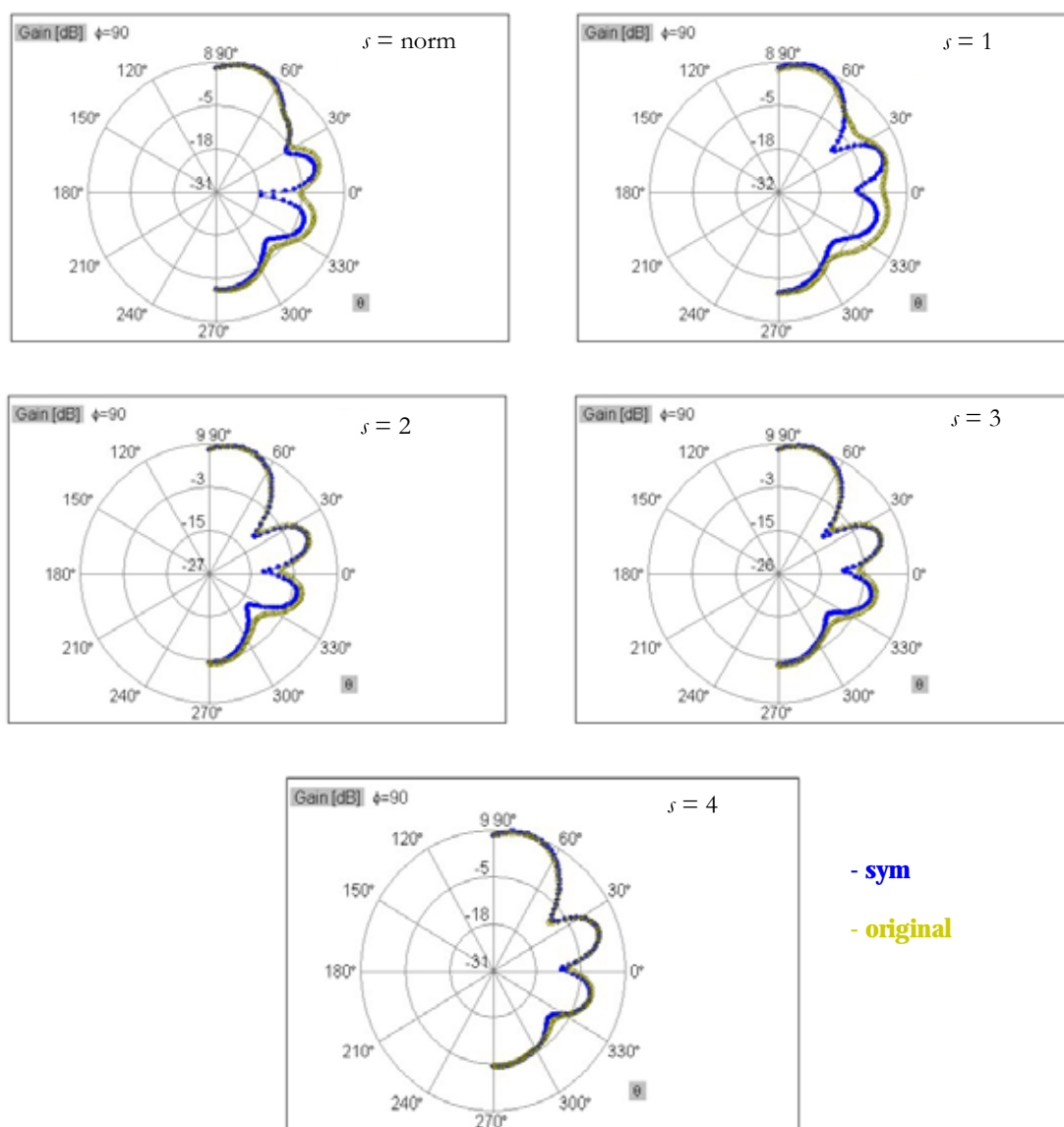


Figure C.12 – Vertical radiation pattern obtained for the MeRo scenario.

Table C.13 – Differences in radiation pattern using symmetry (MePo scenario).

$s$	Horizontal pattern			Vertical pattern		
	$\bar{\mathcal{E}}_{sym\_s}$ [dB]	$\sqrt{\mathcal{E}_{sym\_s}^2}$ [dB]	$\mathcal{E}_{w\_sym\_s}$ [dB]	$\bar{\mathcal{E}}_{sym\_s}$ [dB]	$\sqrt{\mathcal{E}_{sym\_s}^2}$ [dB]	$\mathcal{E}_{w\_sym\_s}$ [dB]
norm	-0.03	0.05	0.00	-0.03	0.09	0.00
4	-0.06	0.29	0.00	0.28	1.77	0.03

Table C.14 – Comparison of CPU resources (MePo scenario).

	$s = \text{norm}$		$s = 4$	
	original	symmetry	Original	symmetry
CPU time [s]	28	28	51	61
Number of unknowns	728	357	1 298	1 019

Table C.15 – Differences in radiation pattern using symmetry (MeRo scenario).

$s$	Horizontal pattern			Vertical pattern		
	$\overline{\mathcal{E}}_{\text{sym}_s}$ [dB]	$\sqrt{\mathcal{E}_{\text{sym}_s}^2}$ [dB]	$\mathcal{E}_{w_{\text{sym}_s}}$ [dB]	$\overline{\mathcal{E}}_{\text{sym}_s}$ [dB]	$\sqrt{\mathcal{E}_{\text{sym}_s}^2}$ [dB]	$\mathcal{E}_{w_{\text{sym}_s}}$ [dB]
norm	-1.11	2.36	-0.37	-1.73	2.89	-0.27
1	-1.36	2.92	0.62	-2.33	3.48	-0.13
2	-0.27	3.68	0.01	-1.22	1.82	-0.14
3	-0.17	3.57	0.16	-0.98	1.44	-0.12
4	0.14	2.14	0.25	-0.24	0.72	0.04

Table C.16 – Comparison of CPU resources (MeRo scenario).

	$s = \text{norm}$		$s = 1$		$s = 2$		$s = 3$		$s = 4$	
	original	sym	original	sym	original	sym	original	Sym	original	sym
CPU time [s]	31	30	52	45	79	80	136	110	111	59
Number of unknowns	1 068	581	1 520	871	1 739	1 288	2 274	1 644	2 548	1 255



# **Annex D**

## **Radiation Patterns**

This annex presents the complete set of radiation patterns obtained through WIPL-D, for the five considered scenarios of BS installation.

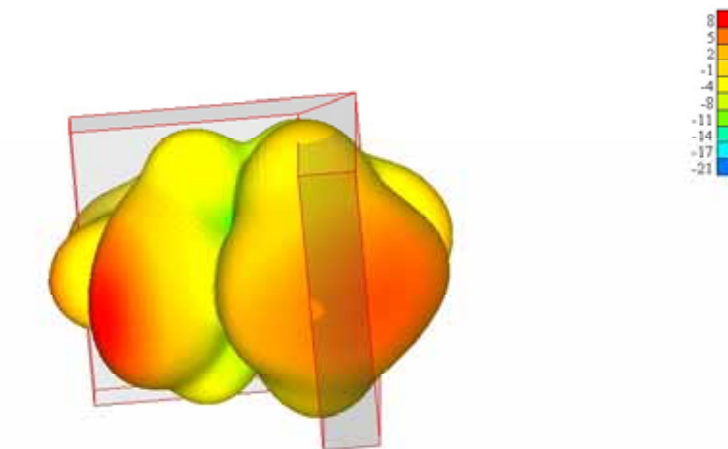


Figure D.1 – 3D radiation pattern obtained for the DiCo scenario.

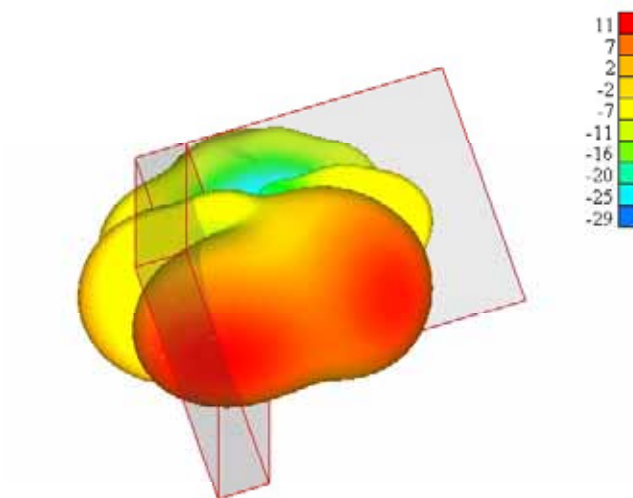


Figure D.2 – 3D radiation pattern obtained for the MeCo scenario.

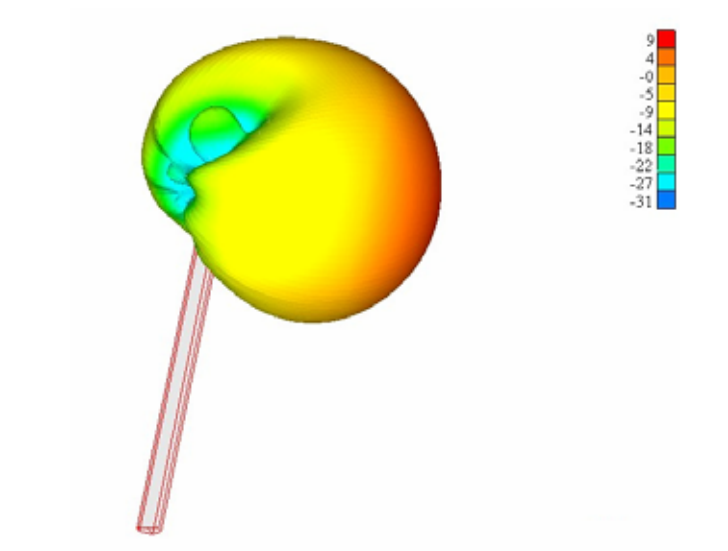


Figure D.3 – 3D radiation pattern obtained for the MePo scenario.

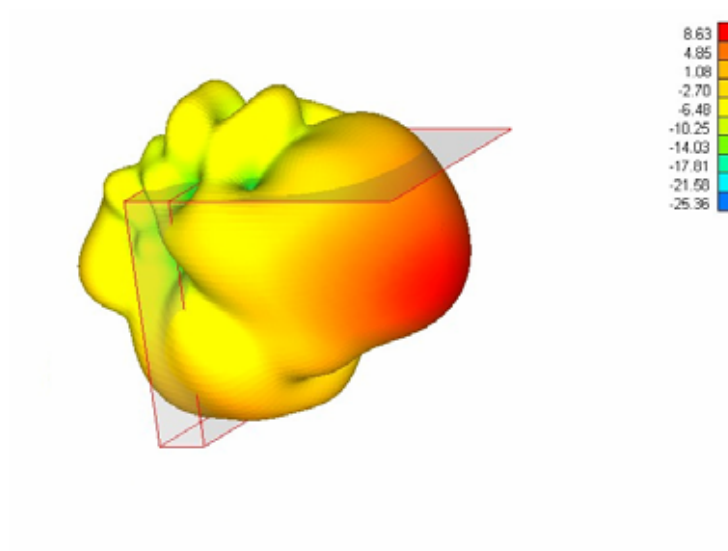


Figure D.4 – 3D radiation pattern obtained for the MeRo scenario.

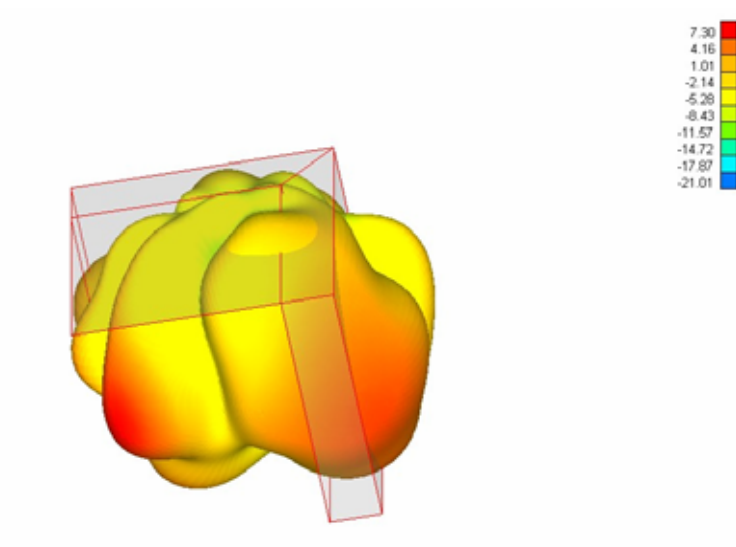


Figure D.5 – 3D radiation pattern obtained for the MeRC scenario.

# References

- [ABDK02] Altman,Z., Begasse,B., Dale,C., Karwowski,A., Wiart,J., Wong,M.-F. and Gattoufi,L., “Efficient Models for Base Station Antennas for Human Exposure Assessment”, *IEEE Transactions on Electromagnetic Compatibility*, Vol. 44, No. 4, Nov. 2002, pp. 588-592.
- [AnMP01] Andersen,J.B., Mogensen,P.E. and Pedersen,G.F., *Exposure Aspects of W-CDMA – Report to the GSM Association*, Aalborg University, Aalborg, Denmark, Dec. 2001.
- [ANAC03] ANACOM, *Procedures for monitoring and measurement of electromagnetic field strength levels originated by radiocommunication stations* (in Portuguese), ICP-ANACOM, Lisbon, Portugal, May 2003.
- [ANTE04] Antennessa, EMF Visual (<http://www.antennessa.com/mods/en/gen/contact>).
- [Bala89] Balanis,C.A., *Advanced Engineering Electromagnetics*, John Wiley & Sons, New York, NY, USA, 1989.
- [Bala97] Balanis,C.A., *Antenna Theory: Analysis and Design*, John Wiley & Sons, New York, NY, USA, 1997.
- [BCCP03] Bernardi,P., Cavagnaro,M., Cicchetti,R., Pisa,S., Piuizzi,E. and Testa,O., “A UTD/FDTD Model to Evaluate Human Exposure to Base-Station Antennas in Realistic Urban Environments”, in *Proc. of 2003 IEEE MTT-S International Microwave Symposium*, Philadelphia, PA, USA, June 2003.
- [BCPP00] Bernardi,P., Cavagnaro,M., Pisa,S. and Piuizzi,E., “Human Exposure to Radio Base-Station Antennas in Urban Environment”, *IEEE Transactions on Microwave Theory and Techniques*, Vol. 48, No. 11, Nov. 2000, pp.1996-2002.

- [BCFF99] Barbiroli,M., Carciofi,C., Falciassecca,G. and Frullone,M., “Analysis of field strength levels near base station antennas”, in *Proc. of VTC’99— IEEE International Vehicular Technology Conference*, Houston, TX, USA, May 1999.
- [Bena99] Benabdallah,N. (ed.), *RF System Scenarios*, 3GPP Technical Specification, No. 25.942, Ver. 2.1.1, Dec. 1999 (<http://www.3gppg.org>).
- [BFHM00] Bergqvist,U., Friedrich,G., Hamnerius,Y., Martens,L., Neubauer,G., Thuroczy,G., Vogel,E. and Wiart,J., *Mobile Telecommunication Base Stations – Exposure to Electromagnetic Fields – Report of a Short Term Mission within COST244bis*, COST 244bis, Brussels, Belgium, Nov. 2000.
- [BiGi99] Bizzi,M. and Gianola,P., “Electromagnetic fields radiated by GSM antennas, Electronic Letters”, *Electronic Letters*, Vol. 35, No. 11, May 1999, pp. 855-857.
- [Bing02] Bing,B., *Wireless Local Area Networks – The New Wireless Revolution*, John Wiley & Sons, New York, NY, USA, 2002.
- [BIRC02] Blanch,S., Romeu,J. and Cardama,A., “Near Field in the Vicinity of Wireless Base-Station Antennas: An Exposure Compliance Approach”, *IEEE Transactions on Antennas and Propagation*, Vol. 50, No. 5, May 2002, pp. 685-692.
- [CENE02] CENELEC, *Basic standard for the calculation and measurement of electromagnetic field strength and SAR related to human exposure from radio base stations and fixed terminal stations for wireless telecommunication systems (110 MHz – 40 GHz)*, Ref. No. EN 50383:2002 E, Central Secretariat, Brussels, Belgium, July 2002.
- [CENE04] CENELEC, *Basic standard to demonstrate the compliance of fixed equipment for radio transmission (110 MHz – 40 GHz) intended for use in wireless communication networks with the basic restrictions or the reference levels related to general public human exposure to radio frequency electromagnetic fields, when put into service*, Ref. No. prEN 50400:2002 E, Central Secretariat, Brussels, Belgium, June 2004.
- [CGLM99] Carli,E., Gianola,P., Lombardi,G., Mama,L. and Vescovo,R., “Antenna models for field level evaluation in proximity of GSM Base stations”, in *Proc. of EPMCC’99 – 3<sup>rd</sup> European Personal and Mobile Communications Conference*, Paris, France, Mar. 1999.

- [CISC06a] Cisco Systems (<http://www.cisco.com>).
- [CISC06b] Cisco Systems, *Cisco Aironet Antennas and Accessories Reference Guide*, 2006 ([http://www.cisco.com/en/US/products/hw/wireless/ps469/products\\_data\\_sheet09186a008008883b.html](http://www.cisco.com/en/US/products/hw/wireless/ps469/products_data_sheet09186a008008883b.html)).
- [CoEU04] Council of the European Union, “Corrigendum to Directive 2004/40/EC of the European Parliament and of the Council of 29 April 2004 on the minimum health and safety requirements regarding the exposure of workers to the risks arising from physical agents (electromagnetic fields) (18th individual Directive within the meaning of Article 16(1) of Directive 89/391/EEC)”, *Official Journal of the European Communities L 184/1*, Brussels, Belgium, May 2004.
- [CoEU99] Council of the European Union, “Council Recommendation of 12 July 1999 on the limitation of exposure of the general public to electromagnetic fields (0 Hz to 300 GHz)”, *Official Journal of the European Communities L 199/59*, Brussels, Belgium, July 1999.
- [DaCo99] Damosso,E. and Correia,L.M., *Digital mobile radio towards future generation systems*, COST 231, Final Report, European Commission, Brussels, Belgium, 1999.
- [Dane04] Danestig,J., *Analysis of RF Exposure from Radio Base Station Antennas in Operating Environments*, MSc. Thesis, Chalmers University of Technology, Göteborg, Sweden, 2004.
- [ECCC03] Electronic Communications Committee (ECC) European Conference of Postal and Telecommunications Administrations (CEPT), *Measuring Non-Ionizing Electromagnetic Radiation (9 kHz – 300 GHz)*, ECC Recommendation (02)04, Oct. 2003.
- [EMPI05] Empire (<http://www.empire.de>).
- [ETSI92] ETSI, *European digital cellular telecommunication system (phase 2) – Radio Network Planning Aspects*, ETSI/TC-GSM GSM 05.05, European Telecommunications Standard Institute, Sophia-Antipolis, France, Oct. 1992 (<http://www.etsi.org>).
- [ETSI05] ETSI, *Broadband Radio Access Networks (BRAN); HiperMAN Physical (PHY) Layer*, ETSI TS 102 177 V1.2.1, Sophia-Antipolis, France, Jan. 2005 ([http://webapp.etsi.org/workprogram/Report\\_WorkItem.asp?WKI\\_ID=21362](http://webapp.etsi.org/workprogram/Report_WorkItem.asp?WKI_ID=21362)).

- [FEKO05] FEKO (<http://www.feko.info>).
- [Frid03] Fridén, J., “RF exposure compliance boundary analysis of base station antennas using combined spherical-cylindrical near-field transformations”, *Electronics Letters*, Vol. 39, No. 25, Dec. 2003, pp. 1783-1784.
- [Hall38] Hallén, E., “Theoretical investigations into the transmitting and receiving qualities of antennae”, *Nova Acta Regiae Soc. Sci. Upsaliensis*, Ser. IV, No. 4, Jan. 1938, pp. 1-44.
- [Harr67] Harrington, R.F., “Matrix Methods for Field Problems”, in *Proceedings of the IEEE*, Vol. 55, No. 2, Feb. 1967, pp. 136-149.
- [Harr93] Harrington, R.F., *Field Computation by Moment Method*, Wiley-IEEE Press, Syracuse, NY, USA, 1993.
- [HoJo85] Horn, R.A. and Johnson, C.R., *Matrix Analysis*, Cambridge University Press, Cambridge, UK, 1985.
- [HoTo00] Holma, H. and Toskala, A., *WCDMA for UMTS-Radio Access For Third Generation Mobile Communications*, John Wiley & Sons, Chichester, UK, 2000.
- [ICNI98] ICNIRP, *Guidelines for Limiting Exposure to Time-Varying Electric, Magnetic, and Electromagnetic Fields (up to 300 GHz)*, ICNIRP, Report 0017-9078/98, Germany, 1998.
- [IEEE04] IEEE, *Standard for Local and Metropolitan Area Networks Part 16: Air Interface for Fixed Broadband Wireless Access Systems*, IEEE Std 802.16 – 2004, New York, NY, USA, June 2004.
- [KaAk64] Kantorovich, L. and Akilov, G., *Functional Analysis in Normed Spaces*, Pergamon Press, New York, NY, USA, 1964.
- [KATH06] KATHREIN (<http://www.kathrein.de>).
- [KATH05a] KATHREIN-Werke KG, *Basic Antenna Principles for Mobile Communications*, 2005 (<http://www.kathrein.de/de/mca/techn-infos/download/BasicAntenna.pdf>).



- [KATH05b] KATHREIN, “Kathrein 736 624 – Data Sheet”, Germany, 2005.
- [KATH05c] KATHREIN, Private communication.
- [Kolu99] Kolundzija,B.M., “Electromagnetic Modeling of Composite Metallic and Dielectric Structures”, *IEEE Transactions on Microwave Theory and Techniques*, Vol. 47, No. 7, July 1993, pp. 1021-1032.
- [KoPo93] Kolundzija,B.M. and Popovic,B.D., “Entire-domain Galerkin method for analysis of metallic antennas and scatterers”, in *IEE Proceedings-H. Microwaves, Antennas and Propagation*, Vol. 140, No. 1, Feb. 1993, pp. 1-10.
- [KTHS06] <http://www.s3.kth.se/antenn/index.shtml>
- [LoCa93] Lourenço,P.S. and Carvalho,M.A., *Automation of Antenna Measurement inside Anechoic Chamber II* (in Portuguese), Graduation Report, Instituto Superior Técnico, Lisbon, Portugal, Oct. 1993.
- [MATL06] MATLAB Release 14 (<http://www.mathworks.com/products/matlab/>).
- [MFRL02] Martínez-González,A.M., Fernández-Pascual,A., Reyes,E., Van Loock,W.V., Gabriel,C. and Sánchez-Hernández,D., “Practical procedure for verification of compliance of digital mobile radio base stations to limitations of exposure of the general public to electromagnetic fields”, in *IEE Proceedings Microwaves, Antennas and Propagation*, Vol. 149, No. 4, Aug. 2002, pp. 218-228.
- [MNMV02] Martínez-Burdalo,M., Nonidez,L., Martín,A. and Villar,R., “On the calculation of safety distances for human exposure to electromagnetic fields from base-station antennas”, *Microwave and Optical Technology Letters*, Vol. 43, No. 5, Sep. 2002, pp. 364-367.
- [MONI04] monIT Project, Private communication.
- [MoPa92] Mouly,M. and Pautet,M., *The GSM System for Mobile Communications*, Cell&Sys, Palaiseau, France, 1992.
- [NARD06] *Narda SRM3000 Data Sheet*, Narda-STS, Germany, 2006 (<http://www.narda-sts.de/pdf/hochfrequenz/ME-E0213G.pdf>).

- [NEC05] NEC (<http://www.nittany-scientific.com>).
- [NMMV01] Nonidez,L., Martínez-Burdalo,M., Martín,A. and Villar,R., “A Combination of Time-Domain Versions of PO and PTD with the FDTD Method to Evaluate Human Exposure to an Electromagnetic Field in an Urban Environment”, *Microwave and Optical Technology Letters*, Vol. 31, No. 5, Dec. 2001, pp. 371-374.
- [OFRC04] Oliveira,C., Fernandes,C., Reis,C., Carpinteiro,G., Ferreira,L., Correia,L.M. and Sebastião,D., *Definition of Exclusion Zones around Typical Installations of Base Station Antennas*, monIT Project, Report Ext\_Tec\_0102\_13, Instituto de Telecomunicações, Lisbon, Portugal, Dec. 2004.
- [OIFC06] Oliveira,C., Fernandes,C. and Correia,L.M., “Estimation of Exclusion Zones for Base Stations Antennas in Wireless Communication Systems”, in *Proc. of EHE'06 – International Conference on EMFs, Health and Environment*, Madeira, Portugal, Apr. 2006.
- [OlMa00] Olivier,C. and Martens,L., “A More Accurate Method to Define Exclusion Zones”, in *Proc. of RAWCON - IEEE Radio and Wireless Conference*, Denver, CO, USA, Sep. 2000.
- [OrFr04] Orange France, 2004 (<http://www.orange.fr>).
- [Pars92] Parsons,J.D., *The Mobile Radio Propagation Channel*, Pentech Pres, London, UK, 1992.
- [Pock97] Pocklington,H.C., “Electrical Oscillations in Wire”, in *Proc. of Cambridge Philos Soc.*, Cambridge, UK, Oct. 1897.
- [RaWG82] Rao,S.M., Wilton,D.R. and Glisson,A.W., “Electromagnetic Scattering by surfaces of Arbitrary Shape”, *IEEE Transactions on Antennas and Propagation*, Vol. 30, No. 3, May 1982, pp. 409-418.
- [Sadi00] Sadiku,M., *Numerical Techniques in Electromagnetics*, CRC Press, Prairie View, TX, USA, 2000.
- [Sche43] Schelkunoff,S.A., *Electromagnetic Waves*, D. van Nostrand, New York, NY, USA, 1943.

- [Vaug04] Vaughan-Nichols,S.J., “Achieving Wireless Broadband with WiMax”, *Computer*, Vol. 37, Issue 6, June 2004, pp. 10-13.
- [WiMA05] WiMAX Forum (<http://www.wimaxforum.org>).
- [WiMA06] WiMAX Forum, *Mobile WiMAX – Part I: A Technical Overview and Performance Evaluation*, Mar 2006.
- [WIPL05] WIPL (<http://www.wipl-d.com>).
- [Wojc02] Wójcik,D., “Evaluation of Near Field of the GSM Base Station Antennas in Urban Environment”, in *Proc. of MIKON 2002 - 14<sup>th</sup> International Conference on Microwaves, Radar and Wireless Communications*, Gdansk, Poland, May 2002.